12-2017

A Comprehensive Framework for White-Box Damage Detection in Structural Systems Based on Extended Constitutive Relation Error Method

Xiaoyu Hu
Clemson University

A COMPREHENSIVE FRAMEWORK FOR WHITE-BOX DAMAGE DETECTION IN STRUCTURAL SYSTEMS BASED ON EXTENDED CONSTITUTIVE RELATION ERROR METHOD

A Dissertation
Presented to
the Graduate School of
Clemson University

In Partial Fulfillment
of the Requirements for the Degree
Doctor of Philosophy
Civil Engineering

---

by
Xiaoyu Hu
December 2017

Accepted by:
Dr. Sez Atamturktur, Committee Chair
Dr. Hsein Juang
Dr. Weichiang Pang
Dr. Nadarajah Ravichandran
Dr. Akshay Gupte

ABSTRACT

Early detection of the deterioration and degradation in civil infrastructure is critical for structural engineers and infrastructure managers to develop rehabilitation and maintenance plans. In the field of structural health monitoring, numerous techniques have been developed to detect and localize damage by examining changes in measured vibration response. Among vibration-based damage detection techniques, model-based approach has been widely used as its damage detection process incorporates the geometric configuration, physical properties, and behavioral characteristics of the structural system.

However, the model-based approaches depend on a model calibration procedure that is based only on the outputs of numerical models without explicitly taking the knowledge regarding the mechanistic behavior of the system into account. Moreover, due to the limitation of measurement degrees of freedom (DOFs), the number of identified vibration modes are typically far fewer than the number of model variables to be calibrated. Consequently, these model-based damage detection methods frequently suffer from an ill-posed inverse-problem.

This dissertation contributes to the field of model-based damage detection by implementing the Extended Constitutive Relation Error (ECRE), a method developed for error localization in finite element models for detecting structural damage. Implementing ECRE for damage detection leads to the localization of elements with high residual energy through the identification of discrepancies between experimental measurements and model predictions due to damage. The ECRE-based damage detection technique incorporates the

underlying physics of the problem in a tangible and visible manner, and thus leading to more reliable solutions in the damage detection and localization process.

This dissertation applies the ECRE-based damage detection in the context of both linear and nonlinear dynamical systems. In particular, the dissertation integrates the Multi-harmonic balance method with ECRE to accurate identify the modeling errors of locally nonlinear dynamical systems. This approach has a potential to be applied for damage detection in the nonlinear structural system, as well as to be used as a damage prognosis tool for the estimation of structural system's remaining useful life.

DEDICATION

I dedicate this dissertation to my family for their constant love and support.

ACKNOWLEDGMENTS

I would foremost like to express my deepest gratitude to my advisor and committee chair, Dr. Sez Atamturktur, for excellent guidance, encouragement and remarkable patience on my research and study. I also would like to thank the rest of my dissertation committee, Dr. Hsein Juang, Dr. Weichiang Pang, Dr. Nadarajah Ravichandran, and Dr. Akshay Gupte, for their willingness to mentor and serve on my committee.

This dissertation would not have been completed without the support of my family and friends. I would like to take this opportunity to acknowledge my parents for their love and support throughout my life. I would like to thank my girlfriend Mengmeng Zhao for being so considerate and motivating me to keep working towards graduation. Additionally, I would like to thank Fanfu Fan, Wenping Gong, Zhe Chen, Yongzhi Shao, Zhengshou Lai, Jie Lu, Tao Ruan and all other friends for making my PhD life so enjoyable.

I must also thank my fellow research group colleagues: Dr. Saurabh Prabhu, Marcos Martínez, Evan Chodora, Aditya Kamath, Robert Locke and Andre Apostol for their support and comments for my dissertation.

Last, but not least, I would like to thank the faculty and staff of the Glenn Department of Civil Engineering at Clemson University for their teaching, help, advice and support during my PhD study.

TABLE OF CONTENTS

Page

LIST OF FIGURES

Figure Page

LIST OF TABLES

Figure Page

CHAPTER ONE

INTRODUCTION

1.1 Introductory remarks

The growing body of research in vibration-based damage identification over the last few decades (Mcgowan et al. 1990; Ding et al. 1994; Salawu 1997; Zou et al. 2000; Brownjohn et al. 2000; Chang et al. 2003; Jaishi and Ren 2006) exploits the dependency of vibration response features (notably modal properties such as frequencies, mode shapes, and modal damping) on the physical properties of the structure (mass, damping, and stiffness), operating on the premise that changes in these physical properties due to damage lead to measurable changes in vibration response. Vibration-based damage detection can be classified into two major categories: data-driven and model-based (Daigle and Goebel 2013; Teughels and Roeck 2004). Data-driven approaches involve developing empirical models based on measurements collected through either periodic or continuous vibration monitoring. Model-based approaches, on the other hand, entail calibrating damage indicating parameters of a physics-based computer model of a healthy (baseline) system using experimental data on the same system in its damaged condition. A key benefit of the model-based approach is its ability to incorporate any available knowledge regarding the geometric configuration, physical properties and behavioral characteristics of the structural system through the integration of a computer model into the damage detection framework.

As a result, model-based damage detection can not only detect, but also localize, classify and determine the severity of damage. These benefits have motivated numerous researchers, including the research campaign proposed herein, to focus on the advancement of model-based damage detection methods (Hearn and Testa 1991; Fritzen and Jennewein 1997).

Model-based damage detection is typically implemented using finite element (FE) model calibration, a process initially developed for improving the accuracy of a FE model so that the model predicted dynamic response matches the experimentally measured response (Young and Frank 1969; Berman 1979). Starting in 1990s, the concept of FE model calibration was implemented for damage detection by calibrating the FE model of a healthy structural system (baseline model) based on the measurements obtained from the same system in an unhealthy (i.e. damaged) condition (Fritzen and Jennewein 1997). In this implementation, damage was identified by comparing the changes in the physical parameters or stiffness related properties of the model between the calibrated and baseline FE models.

Model calibration methods can be further divided into two major categories: the *direct* method and *parametric* method (Jaishi and Ren 2006; Weng et al. 2009). The direct method calibrates the individual elements of the mass, stiffness, and damping matrices so that the error in calibrated model predictions with respect to the measured data is minimized (Berman 1979; Baruch 1982; Berman and Nagy 1983; Cha and Gu 2000).

However, a major drawback of direct method is that, even when the resulting matrices reproduce the measured modal properties, these calibrated matrices do not necessarily maintain structural connectivity (Kabe 1985) and are not always physically meaningful (Mottershead and Friswell 1993). For instance, Mcgowan et al. (1990) adopted a direct model calibration method for locating the damaged truss member in a large space structure and demonstrated the dependency of the structural stiffness matrix updated using the direct method on the mode selection and sensor placement. Thus, multiple configurations of the stiffness matrix can produce similar results, highlighting the issue of non-uniqueness of the inverse problem that typically arises when the number of measurement points are far fewer than the number of model variables to be calibrated.

Direct methods were followed by the emergence of parametric methods, which minimize the differences between the model predictions and experimental measurements by fine-tuning damage indicative physical parameters of the model. As these damage indicative parameters are allowed to vary with predefined distributions, parametric methods inherently preserve the physical meaning of imposed corrections (Piranda et al. 1991, Teughels et al. 2002). In parametric methods, one caveat is that the selected calibrating parameters must be sufficiently sensitive to the changes in the selected response features due to the onset of damage. This led to the development of sensitivity-based model calibration (Center et al. 1991; Beven and Binley 1992; Doebling et al. 1998), which has

been widely applied for model-based damage detection (see for instance Ricles and Kosmatka 1992; Farhat and Hemez 1995). However, the parameters with higher sensitivity are not necessarily the source of the discrepancy. Furthermore, this sensitivity-based approach results in calibrated models that reflect the optimum compensations of errors caused by different sources (Hemez and Farrar 2014). Thus, both the direct and parametric methods of model calibration suffer from drawbacks related to non-uniqueness of solutions, which can be partially assuaged by increasing the number of measurement points. However, such efforts are often impractical as additional experimentation is prohibitive, costly or time consuming. An alternative remedial measure is to exploit the model physics to calibrate the model in a physically meaningful manner, alleviating the problems related to non-uniqueness or improbability of solutions.

1.2 Motivation for research

Model-based damage detection methods mentioned in the previous section treat model calibration as a black-box problem, by minimizing the difference between computer model predictions, $y^{prediction}$, (e.g. the natural frequency, mode shape, modal force, mode shape curvature, etc.) and experimental measurements, y^{test}, while neglecting the physics governing the system behavior (Figure 1). Mottershead and Friswell (1993) noted that the inverse analysis necessary for black-box approaches is typically ill-posed, as the number of identified vibration modes are far fewer than the number of model variables to be

calibrated, owing to limited measurement degrees of freedom (DOFs). Ill-posed inverse problems allow compensations between parameters and typically lead to multiple plausible solutions (in our context, identification of multiple plausible damage scenarios), a concept widely referred to as non-uniqueness (Mottershead and Friswell 1993; Imregun et al. 1995; Janssen and Heuberger 1995; Kenigsbuch and Halevi 1998; Atamturktur et al. 2015, Prabhu et al. 2017).

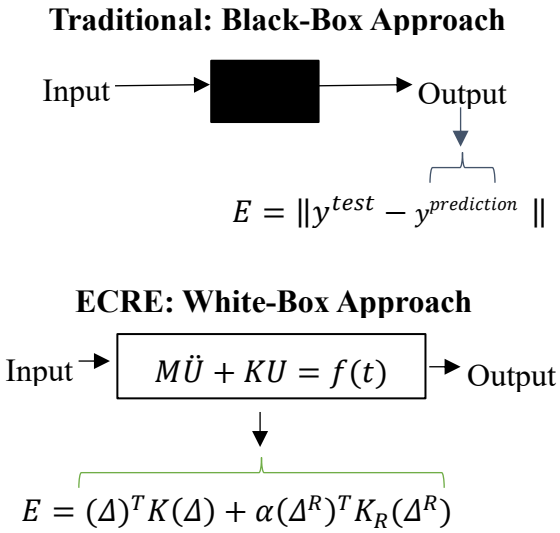

Figure 1.1. Comparison of black- and white-box approaches.

The goal of this dissertation is to establish a white-box damage detection technique along with its accompanying Structural Health Monitoring (SHM) framework through the implementation and expansion of the Extended Constitutive Relation Error (ECRE) concept (Ladeveze, 1983). What distinguishes the proposed white-box approach from the black-box damage detection techniques developed earlier is the incorporation of the underlying physics of the problem in a tangible and visible manner into the inverse analysis

process needed for identifying damage (as shown in Figure 1). Thus, the proposed white-box damage detection technique constrains the problem and leads to a unique solution in the damage detection and localization process (Faverjon and Sinou 2008).

1.3 Contributions of the dissertation

The contributions of this dissertation are three-fold as follows:

1. A two-step ECRE-based approach is developed for damage detection in *linear* structural systems with the consideration of error in the stiffness distribution.
2. The two-step ECRE-based damage detection is extended by simultaneously considering the effect of stiffness and mass error in the calculation of damage indicator.
3. An integrated MHB-ECRE calibration method is established to provide *a reliable numerical model* for the further application of the damage detection to *nonlinear* systems.

1.3.1 Damage detection in linear structural systems with consideration of stiffness error

A white-box ECRE-based approach for damage detection in *linear* structural systems is developed as the first pillar of the proposed SHM framework. The proposed damage detection method is capable of identifying the damage that alters the linear dynamic response and introduces nonlinear dynamic response. The response of an undamaged system is assumed to be linear and the introduction of damage can either

linearly or nonlinearly modify this response (Adams and Farrar 2002; Farrar et al. 2007). For instance, a crack, one of the most common types of damage, opens and closes under operational loading and may introduce nonlinearity to an originally linear system (Sundermeyer and Weaver 1995). The white-box approach proposed herein can straightforwardly identify such newly introduced nonlinearity or change in the linear response, and exploit the identified changes in the determination and localization of damage.

1.3.2 Damage detection in linear systems with consideration of stiffness and mass error

In the context of damage detection, the ECRE method calculates the residual energy between the experimental measurement and numerical model as the damage indicator. Yet, the residual energy only considers errors in the stiffness distribution given the inherent assumption that the connection damage would only lead to stiffness reduction. Structural damage, however, often modifies not only the stiffness, but also the mass distribution and damping. To account for such modifications, the ECRE-based damage detection method is extended in this study to account for errors in both stiffness and mass distribution. The uncertainties in the mass matrix are explicitly treated to ensure that the identification results are more robust to modeling error instead of assuming an accurately characterized mass matrix.

1.3.3 Model calibration in locally nonlinear structural systems

As all real-world structures are inherently nonlinear, the white-box ECRE-based approach is extended for model calibration in nonlinear dynamic systems. While the ECRE-based model calibration method has been utilized for identifying damage that causes the change of system's stiffness and mass, the proposed nonlinear model calibration approach has a potential to be further used as a damage prognosis tool that can estimate a structural system's remaining useful life (Farrar and Lieven 2007).

Nonlinear model calibration techniques calibrate all the parameters that describe both linear and nonlinear dynamic response in a collective manner (Lenaerts et al. 2001; Bellizzi and Defilippi 2003; Meyer and Link 2003; Kerschen et al. 2006). The drawback of such an approach is that the calibration of nonlinear parameters is significantly dependent on the model error associated with the linear component of dynamic response. This occurs because the calibration is based on the features extracted from the total structural response, despite the existence of two types of model error in both linear and nonlinear components of the response that need correction. In this study, we develop a method for the localization and classification of model error in nonlinear structural systems by distinguishing model error in both linear and nonlinear dynamic components. Thereby, the traditional one-step nonlinear model calibration is divided into a two-step calibration

process, which accounts for the influence of the model error in the associated linear component of dynamic response that has drawn less attention.

1.4 Dissertation organization

This dissertation proposal is organized into three chapters as described in the following paragraphs.

Chapter 2 introduces an application of the ECRE-based damage detection approach, which was originally developed for model error localization and model calibration in FE models. For a given structure in a healthy state, the ECRE approach can identify residual energy between experimental measurements and model predictions by considering both stiffness modeling errors and experimental noise. A two-step, ECRE-based damage detection is developed and its feasibility in identifying the presence, location and relative severity of damage is demonstrated on a scaled, two-story steel frame for damage scenarios of varying types and severity.

Chapter 3 discusses a modified ECRE-based damage detection strategy considering both the variation in mass and stiffness distribution. The calculation for residual energy is reformulated and amended to consider simultaneously the error in both stiffness and mass distribution, as well as experiemental noise for more reliable damage detection results. Moreover, the uncertainties in the mass matrix are explicitly treated to ensure that the identification results are more robust to modeling errors. Consequently, when the structural

system's masses are considered uncertain and are included in the damage indicator to be identified, the number of false negatives is reduced. The accuracy and efficiency of this modified approach is demonstrated through the same experimental measurements on the scaled, two-story steel frame as conducted in Chapter 2.

Chapter 4 discusses the MHB-ECRE based model calibration approach for locally nonlinear systems. The implemented strategy is based on the MHB-ECRE approach and relies on shaker tests conducted on the nonlinear structural system at low and high excitation force magnitudes. The first step is based on the low magnitude excitation test, under which the system behaves in a predominately linear manner, and thus the location of model error associated with the linear component can be identified through the utilization of the MHB-ECRE method. In the second step, a higher magnitude excitation is applied to insure the nonlinear dynamic response. The measurements from both low and high magnitude excitation tests are used to calibrate the model parameters associated with linear and nonlinear components. This strategy can be extended and applied for identifying the damage in a nonlinear structural system.

References

Adams, D. E., & Farrar, C. R. (2002). Classifying linear and nonlinear structural damage using frequency domain ARX models. *Structural Health Monitoring*, *1*(2), 185-201.

Atamturktur S., Liu Z., Cogan S. and Juang C. H. (2015), Calibration of imprecise and inaccurate numerical models considering fidelity and robustness: a multi-objective optimization based approach. *Structural and Multi-disciplinary Optimization (Springer), 51*(3), 659-671.

Baruch, M. (1982). Optimal correction of mass and stiffness matrices using measured modes. *AIAA Journal*, *20*(11), 1623-1626.

Berman, A. (1979). Mass matrix correction using an incomplete set of measured modes. *AIAA journal*, *17*(10), 1147-1148.

Berman, A., & Nagy, E. J. (1983). Improvement of a large analytical model using test data. *AIAA journal*, *21*(8), 1168-1173.

Beven, K., & Binley, A. (1992). The future of distributed models: model calibration and uncertainty prediction. *Hydrological processes*, *6*(3). 279-298.

Center, J. S., Ricles, J. M., & Hamilton, D. A. (1991). Nondestructive structural damage detection in flexible space structures using vibration characterization. *William A. Hyman and Stanley H. Goldstein, Editors*.

Cha, P. D., & Gu, W. (2000). Model updating using an incomplete set of experimental modes. *Journal of sound and vibration*, *233*(4), 583-596.

Chang, P. C., Flatau, A., & Liu, S. C. (2003). Review paper: health monitoring of civil infrastructure. *Structural health monitoring*, *2*(3), 257-267.

Daigle, M., and Goebel, K. (2013). Model-based prognostics with concurrent damage progression processes. *Systems, Man, and Cybernetics: Systems, IEEE Transactions*, *43*(3), 535-546.

Ding, J. L., Pazhouh, J., Lin, S. B., & Burton, T. D. (1994). Damage characterization by vibration test. *Scripta metallurgica et materialia*, *30*(7), 839-844.

Doebling, S. W., Farrar, C. R. and Prime, M. B. (1998). A summary review of vibration-based damage identification methods. *Shock and vibration digest 30*(2), 91-105.

Farhat, C. & Hemez, F. M. (1995). Structural Damage Detection via a Finite Element Model Updating Methodology. *Modal Analysis – The International Journal of Analytical and Experimental Modal Analysis*, *10*(3), 152-166.

Farrar, C. R., & Lieven, N. A. (2007). Damage prognosis: the future of structural health monitoring. *Philosophical Transactions of the Royal Society of London A: Mathematical, Physical and Engineering Sciences*, *365*(1851), 623-632.

Farrar, C. R., Worden, K., Todd, M. D., Park, G., Nichols, J., Adams, D. E., & Farinholt, K. (2007). Nonlinear system identification for damage detection (No. LA-14353-MS). *Los Alamos National Laboratory (LANL)*, Los Alamos, NM.

Imregun, M., Sanliturk, K. Y., & Ewins, D. J. (1995). Finite element model updating using frequency response function data: II. Case study on a medium-size finite element model. *Mechanical Systems and Signal Processing*, *9*(2), 203-213.

Jaishi, B, and Ren, W. (2006). Damage detection by finite element model updating using modal flexibility residual. *Journal of sound and vibration, 290*(1), 369-387.

Janssen, P. H. M., & Heuberger, P. S. C. (1995). Calibration of process-oriented models. *Ecological Modelling*, *83*(1), 55-66.

Kabe, A. M. (1985). Stiffness matrix adjustment using mode data. *AIAA journal*, *23*(9) 1431-1436.

Kenigsbuch, R., & Halevi, Y. (1998). Model updating in structural dynamics: a generalised reference basis approach. *Mechanical Systems and Signal Processing*, *12*(1) 75-90.

Kerschen, G., Worden, K., Vakakis, A. F., & Golinval, J. C. (2006). Past, present and future of nonlinear system identification in structural dynamics. *Mechanical systems and signal processing*, *20*(3) 505-592.

Ladeveze, P., & Leguillon, D. (1983). Error estimate procedure in the finite element method and applications. *SIAM Journal on Numerical Analysis*. *20*(3), 485-509.

Lenaerts, V., Kerschen, G., & Golinval, J. C. (2001). Proper orthogonal decomposition for model updating of non-linear mechanical systems. *Mechanical Systems and Signal Processing*, *15*(1), 31-43.

McGowan, P. E., Smith, S. W., & Javeed, M. (1990). Experiments for locating damage members in a truss structure. In *Proc. 2nd USAF/NASA Workshop on System Identification and Health Monitoring of Precision Space Structures* 571-615.

Meyer, S., & Link, M. (2003). Modelling and updating of local non-linearities using frequency response residuals. *Mechanical Systems and Signal Processing, 17*(1), 219-226.

Mottershead, J. E., & Friswell, M. I. (1993). Model updating in structural dynamics: a survey. *Journal of sound and vibration, 167*(2), 347-375.

Piranda, J., Lallement, G., & Cogan, S. (1991). Parametric correction of finite element models by minimization of an output residual: Improvement of the sensitivity method. *Proceedings of the 9th International Modal Analysis Conference*, 363-368.

Prabhu, S., Atamturktur, S., & Cogan, S. (2017). Model assessment in scientific computing: Considering robustness to uncertainty in input parameters. *Engineering Computations*, *34*(5), 1700-1723.

Ricles, J. M. and Kosmatka, J. B. (1992). Damage Detection in Elastic Structures Using Vibratory Residual Forces and Weighted Sensitivity. *AIAA Journal*, *30*(9), 2310–2316

Salawu, O. S. (1997). Detection of structural damage through changes in frequency: A Review. *Engineering Structures*, *19*(9) 718-723.

Sundermeyer, J. N., & Weaver, R. L. (1995). On crack identification and characterization in a beam by non-linear vibration analysis. *Journal of Sound and Vibration*, *183*(5), 857-871.

Teughels, A., & De Roeck, G. (2004). Structural damage identification of the highway bridge Z24 by FE model updating. *Journal of Sound and Vibration*, *278*(3), 589-610.

Teughels, A., Maeck, J. & Roeck, G. D. (2002). Damage assessment by FE model updating using damage functions. *Computers and Structures*, 80(25) 1869–1879.

Young, J. P. & Frank J. O. (1969). Mathematical modeling via direct use of vibration data. *SAE Technical Paper*, 690615.

Zou, Y., Tong, L. P. S. G., & Steven, G. P., (2000). Vibration-based model-dependent damage (delamination) identification and health monitoring for composite structures—a review. *Journal of Sound and vibration 230*(2), 357-378.

CHAPTER TWO*

MECHANISTICALLY-INFORMED DAMAGE DETECTION USING DYNAMIC MEASUREMENTS: EXTENDED CONSTITUTIVE RELATION ERROR

2.1 Introduction

Many forms of structural failures in steel frames can be attributed to damage in connections, such as shear failure of bolts, excessive bearing deformation at the bolt-hole and edge tearing or fracture of the connection plate (Carr and Chapetti 2011; Hegenderfer and Atamturktur 2013). One particular damage type is the self-loosening of bolts which leads to the loss of the clamping force in the bolted connection (Zadoks and Yu 1997; Jiang et al. 2003). The loss of structural redundancy from such damage in connections can considerably reduce the load-carrying capacity of a steel frame system, especially when the damaged connection is a critical component of the load path (Prabhu et al. 2014). Hence, early detection of connection damage is essential for structural engineers and infrastructure managers to ensure timely rehabilitation and repair of steel frame structures.

Model-based damage detection is now deemed an effective method for identifying, localizing and determining the severity of damage in structural systems (Wu and Li 2006; Jafarkhani and Masri 2011). In this approach, a numerical model, typically a finite element

* This chapter has been accepted for publication in the Journal of Mechanical Systems and Signal Processing as a technical paper.

(FE) representation, is developed based on the properties of the undamaged system and then updated with respect to the measurements obtained from the damaged system. Damage detection is based on the premise that the changes imposed on the model during the updating process reflect the damage in the system. Over the last three decades, a variety of FE model calibration schemes have been implemented for model-based damage detection. For instance, the earliest techniques entailed calibrating the individual terms within stiffness and mass matrices. Although this approach made it possible to obtain global matrices that reproduced the measured modal parameters identically (Baruch 1982; Berman and Nagy 1983), the resulting matrices were not guaranteed to maintain structural connectivity and the suggested changes in the model were not always related to actual damage (in worst cases the changes were not even physically meaningful)[†] (Farrar et al. 2004). These direct methods were followed by the emergence of indirect (also known as parametric) methods, which focused on updating the parameters of the model and thus, preserved the physical meaning of imposed corrections (Piranda et al. 1991; Link and Floressantiago 1991; Mottershead and Friswell1993; Friswell and Mottershead 1995; Atamturktur et al. 2012). The parametric method, when implemented for damage detection, typically involved solving an optimization problem where a cost function that represents the discrepancy between the FE model of the undamaged system and the experimental

[†] In these applications, the objective was to improve the feedback control loop and hence accurate representation of the structural connectivity was not implemented.

measurements from its damaged counterpart was minimized by manipulating the damage-indicative parameters. This cost function was defined through a user-selected metric, often based on mathematical norms, such as Euclidean distance (Teughels et al. 2004; De Smith 2006; Bi et al. 2014) or p-norms (Lin and Gea 2013), without explicitly taking the knowledge regarding the mechanistic behavior of the system into account. This parametric approach was most commonly applied using non-destructively measured vibration modes (Kammer 1991; Worden and Burrows 2001). In most applications, however, the practical constraints on the number of measurement degrees of freedom (DOFs) limited the number of identified vibration modes resulting in an ill-posed inverse-problem (Friswell 2007). In the context of damage detection, ill-posed inverse-problems lead to multiple plausible solutions (i.e. more than one possible damage scenario), a concept widely referred to as non-uniqueness (Berman and Flannelly 1971).

These approaches for model calibration as applied for damage detection mentioned are based only on the outputs of computer models (natural frequencies, mode shapes, modal forces, etc.). In contrast, the Extended Constitutive Relation Error (ECRE) based damage detection integrates the mechanistic principles (e.g. load-displacement relationships) underlying the behavior of the system during the comparison of model predictions against experiments (Ladevèze 1999; Decouvreur et al. 2008; Isasa et al. 2011; Charbonnel et al. 2013). In the traditional ECRE approach, the model error localization

procedure involves pinpointing the contributions of each element to the global error considering both model and experimental errors (Ladevèze and Leguillon 1983). The proposed ECRE-based damage detection involves calculating the residual energy in each element of the FE model of the undamaged structure using experimental measurements collected from the damaged structure. A damage indicator is then obtained by normalizing the residual energy to the total energy in each element of the FE model. Thus, the damage indicator reveals the damaged elements by pinpointing the greatest disagreement between the model and the experiments represented by the relative residual energy.

Recognizing that computer models are imperfect representations of reality and assuming that experimental measurements are more realistic than the computer models, this paper presents a two-step damage detection approach, which involves determining: i) the residual error due to model imperfections (i.e. traditional ECRE for error localization) and ii) the damage in the structural system while correcting for model imperfection. The corrected elemental residual energy values obtained in the second step therefore reflect the damage state of the structure.

This paper is organized as follows. In Section 2, the authors present the theoretical background for ECRE error localization, discuss the two-step ECRE-based damage detection procedure and demonstrate the capabilities of the proposed approach on a controlled, academic example. In Section 3, the practical applicability of the proposed

approach is demonstrated on a 1/4th scale steel frame with bolted connections considering multiple damage levels. Section 4 presents the two-step damage identification procedure applied to the steel frame system. Finally, Section 5 discusses the potential limitations of the described damage detection method in practical applications. The paper concludes with a discussion on benefits of the proposed approach and directions for future research in Section 6.

2.2 Methodology

2.2.1 Overview of ECRE method for model error localization

Mathematical formulation of ECRE approach

In this study, we implement ECRE in the context of structural dynamics of linear elastic undamped systems, for which the equation of motion can be expressed as:

$$\boldsymbol{M}\ddot{\boldsymbol{x}}(t) + \boldsymbol{K}\boldsymbol{x}(t) = \boldsymbol{f}(t) \tag{1}$$

where $\boldsymbol{M}$, $\boldsymbol{K}$, $\in \Re^{N,N}$ are the discrete mass and stiffness matrices, respectively, of order N that are assumed to be time-invariant, symmetric and non-negative; $\ddot{\boldsymbol{x}}$, $\boldsymbol{x} \in \Re^{N,1}$ are respectively the acceleration and displacement vectors in the time domain; and $\boldsymbol{f} \in \Re^{N,1}$ is the time-dependent excitation vector representing external forces.

The homogeneous equation of motion for the linear elastodynamic structure is written as:

$$(\boldsymbol{K} - \lambda_z \boldsymbol{M})\boldsymbol{y}_z = 0 \tag{2}$$

where $\lambda_z, \boldsymbol{y_z}$ are the z^{th} eigensolutions of Equation (1) with the eigenvalues λ_z and associated eigenvectors $\boldsymbol{y_z} \in \Re^{N,1}$; $\boldsymbol{y_z}$ is assumed to be normalized such that $\boldsymbol{y_z^T K y_z} = \lambda_z$.

Conservative linear elastodynamic systems with stiffness errors

In this study, the ECRE method is extended to not only quantify model error, but also detect the connection damage in steel frame structures, referred to herein as ECRE-based damage detection. Connection damage is often considered to degrade the stiffness of the system without altering its mass distribution (Salawu 1997). Thus, the residual energy (i.e., the model error indicator) is calculated only considering errors in the stiffness distribution[‡]. The ECRE based on the z^{th} experimentally identified eigensolution is defined as:

$$E_z^2 = (\boldsymbol{u_z} - \boldsymbol{v_z})^T \boldsymbol{K} (\boldsymbol{u_z} - \boldsymbol{v_z}) + \frac{\alpha}{1-\alpha} (\boldsymbol{H u_z} - \boldsymbol{u_z^e})^T \boldsymbol{K_R} (\boldsymbol{H u_z} - \boldsymbol{u_z^e}) \tag{3}$$

where E_z^2 is a scalar quantity expressing the extended constitutive relation error as a function of the two unknown admissible vectors $\boldsymbol{u_z}$ and $\boldsymbol{v_z}$; $\boldsymbol{u_z^e} \in \Re^{n,1}$ is the z^{th} identified eigenvector on the *n* experimentally measured DOFs; $\boldsymbol{u_z}$ can be interpreted as an expansion of the experimental eigenvector $\boldsymbol{u_z^e}$ to the *N* model DOFs; $\boldsymbol{v_z}$ is the static displacement field evaluated by the FE model due to the inertial loading $\lambda_z^e \boldsymbol{M u_z}$, which

[‡] Incorporating the mass matrix and damping matrices, the model error can be configured to account for the mass error and damping error (Faverjon & Sinou 2008).

can be solved using the equilibrium of the system as shown in Equation (4); and $H \in \Re^{n,N}$ is a transformation matrix with 0 and 1 entries, which projects the analytical vector, u_z, onto the set of *n* measured DOFs, thus allowing the comparison of mode shapes between the experimental measurement and the FE model. K_R is the reduced stiffness matrix of the FE model with n measured DOFs obtained by Guyan reduction (Guyan 1965). α is a weighting factor, $0 \leq \alpha \leq 1$, with which the decision maker may incorporate the confidence placed on the experimental measurements. Here, a larger α value indicates higher confidence in the measurements. The default value of α is typically taken as 0.5 (Deraemaeker et al. 2002).

Note that there are two error terms on the right-hand side of Equation (3) defined over the measured DOFs: the modeling error (first term) and the mode shape expansion error (second term) that is introduced when the measured mode shapes are extrapolated to the *N* model DOFs (Zimmerman and Kaouk 1994). Both terms are expressed in an energy-based error measure, with respect to the stiffness matrix of the FE model in either its global form, $\boldsymbol{K}$, or reduced form, $\boldsymbol{K_R}$.

The equilibrium equation of the system is given by:

$$\boldsymbol{K v_z} = \lambda_z^e \boldsymbol{M u_z} \tag{4}$$

where λ_z^e is the z^{th} identified eigenvalue. The above equation can also be written as the force residual equation in terms of $(\boldsymbol{u_z} - \boldsymbol{v_z})$:

$$\boldsymbol{K}(\boldsymbol{u_z} - \boldsymbol{v_z}) = (\boldsymbol{K} - \lambda_z^e \boldsymbol{M})\boldsymbol{u_z} \tag{5}$$

where $(\boldsymbol{u_z} - \boldsymbol{v_z})$ is the static relative displacement field resulting from the unbalanced forces, $(\boldsymbol{K} - \lambda_z^e \boldsymbol{M})\boldsymbol{u_z}$, because λ_z^e and $\boldsymbol{u_z}$ are not the eigensolutions of the FE model. If λ_z^e and $\boldsymbol{u_z}$ were eigensolutions of Equation (2), then $(\boldsymbol{u_z} - \boldsymbol{v_z}) \approx 0$ and the value of E_z^2 would be close to zero, depending on the amount of experimental uncertainty. Otherwise, E_z^2 would increase with increasing model error on the calculated DOFs, mode shape expansion error or experimental uncetainty (i.e. measurement noise).

In the ECRE method, the equations of interest (constitutive behavior relations, equations of motion, equilibrium equations, etc.) are divided into the reliable equations and less reliable equations. A minimization problem is then formulated to minimize the error in the less reliable equations under the constraint of the reliable equations. In this study, the measure of the error in Equation (3) is considered as the less reliable equation while the equilibrium equation (Equation (4) or (5)) is considered as the reliable equation. Hereby, the unknown displacement field, $\boldsymbol{u_z}$, and the relative displacement field, $(\boldsymbol{u_z} - \boldsymbol{v_z})$, are obtained by solving the following minimization problem:

$$\begin{cases} \text{Minimize } E_z^2 = \left(\boldsymbol{u_z} - \boldsymbol{v_z}\right)^T \boldsymbol{K}\left(\boldsymbol{u_z} - \boldsymbol{v_z}\right) + \dfrac{\alpha}{1-\alpha}\left(\boldsymbol{H}\boldsymbol{u_z} - \boldsymbol{u_z^e}\right)^T \boldsymbol{K_R}(\boldsymbol{H}\boldsymbol{u_z} - \boldsymbol{u_z^e}) \\ \text{Under the constraint } \boldsymbol{K}\left(\boldsymbol{u_z} - \boldsymbol{v_z}\right) - \boldsymbol{Z}\left(\lambda_z^e\right)\boldsymbol{u_z} = 0 \end{cases} \tag{6}$$

where $\boldsymbol{Z}(\lambda_z^e) \equiv \boldsymbol{K} - \lambda_z^e \boldsymbol{M}$. A saddle-point problem can then be formulated with the introduction of Lagrange multipliers. Assuming $\boldsymbol{K}$ is not rank deficient, the above equations yield the following system of linear equations:

$$\begin{bmatrix} \boldsymbol{Z}\left(\lambda_z^e\right) & \dfrac{\alpha}{1-\alpha}\boldsymbol{H}^T\boldsymbol{K}_R\boldsymbol{H} \\ \boldsymbol{K} & -\boldsymbol{Z}\left(\lambda_z^e\right) \end{bmatrix} \begin{Bmatrix} \boldsymbol{u}_z - \boldsymbol{v}_z \\ \boldsymbol{u}_z \end{Bmatrix} = \begin{Bmatrix} \dfrac{\alpha}{1-\alpha}\boldsymbol{H}^T\boldsymbol{K}_R\boldsymbol{u}_z^e \\ 0 \end{Bmatrix} \tag{7}$$

The solution vectors $\boldsymbol{u_z}$ and $(\boldsymbol{u_z} - \boldsymbol{v_z})$ are evaluated by subsitituting the results from experimental measurements (λ_z^e and $\boldsymbol{u_z^e}$) and the numerical model ($\boldsymbol{K}$, $\boldsymbol{M}$ and $\boldsymbol{K_R}$) into Equation (7). Constitutive error is then calculated using the relative displacement field between $\boldsymbol{u_z}$ and $\boldsymbol{v_z}$ and normalized with respect to a quantity proportional to the total energy. Evaluation of the global model error, $\hat{E}_z^2$ over a set of experimental eigensolutions can be expressed as:

$$\hat{E}_z^2 = \frac{(\boldsymbol{u}_z - \boldsymbol{v}_z)^T \boldsymbol{K}(\boldsymbol{u}_z - \boldsymbol{v}_z) + \dfrac{\alpha}{1-\alpha}(\boldsymbol{H}\boldsymbol{u}_z - \boldsymbol{u}_z^e)^T \boldsymbol{K}_R(\boldsymbol{H}\boldsymbol{u}_z - \boldsymbol{u}_z^e)}{\boldsymbol{u}_z^T \boldsymbol{K}\boldsymbol{u}_z + \lambda_z^e \boldsymbol{u}_z^T \boldsymbol{M}\boldsymbol{u}_z} \tag{8}$$

The elemental residual energy, $E_{z,i}^2$ is then formulated based on the solution to Equation (7). Let $\boldsymbol{K_i} \in \Re^{N,N}$ be the stiffness matrix of the i^{th} subdomain defined by:

$$\boldsymbol{K}_i = \sum\nolimits_{j \in \boldsymbol{S}_i} \boldsymbol{K}_j^{\boldsymbol{ele}} \tag{9}$$

where $\boldsymbol{K_j^{ele}} \in \Re^{N,N}$ are sparse $N \times N$ matrices containing the assembled stiffness matrices of the j^{th} finite element and $\boldsymbol{S_i}$ is the set of element matrices belonging to the

subdomain i. In the formulations, the residual energy that represents the stiffness-based model error for the i^{th} subdomain and the z^{th} experimental eigensolution is then given by:

$$E_{z,i}^{2} = \left(\boldsymbol{u}_z - \boldsymbol{v}_z\right)^T \boldsymbol{K}_i (\boldsymbol{u}_z - \boldsymbol{v}_z) \tag{10}$$

2.2.2 Two-step ECRE-based approach for damage detection

The first step of the proposed two-step damage detection method involves the development of a FE model that represents the undamaged structure. Using this FE model in combination with the experimental measurements collected from the undamaged structure, we obtain the relative displacement vector $\boldsymbol{R_h} = (\boldsymbol{u_z} - \boldsymbol{v_z})$ through Equation (7). This vector $\boldsymbol{R_h}$ also represents the model error in the FE model of undamaged structure that accounts for the discrepancy between the experimentally measured mode shape vectors and those predicted by the FE model.

In the second step, the relative displacement $\boldsymbol{R} = (\boldsymbol{u_z} - \boldsymbol{v_z})$ is calculated to determine the deviation between mode shape vectors experimentally obtained from the damaged structure and those numerically obtained from the FE model of the undamaged structure. The relative displacement field, $\boldsymbol{R_h}$ obtained in the first step, is then used to correct the relative displacement field in the second step, $(\boldsymbol{R} - \boldsymbol{R_h})$ to take into account the imperfections of the FE model (representing the undamaged structure). This correction process significantly reduces the effect of model error on the calculated damage indicators. As a result, the damage index is calculated as:

$$ECRE_i = (\boldsymbol{R} - \boldsymbol{R_h})^T \boldsymbol{K_i} (\boldsymbol{R} - \boldsymbol{R_h}) \tag{11}$$

$$I_{D,i} = \sum_{z=1}^{m} \frac{ECRE_{i,z}}{\boldsymbol{u_z^T K u_z} + \lambda_z^e \boldsymbol{u_z^T M u_z}} \tag{12}$$

where $ECRE_i$ is the residual energy and $\boldsymbol{K_i}$ is the stiffness matrix for the i^{th} subdomain in the FE model of the undamaged structure. For the z^{th} identified mode, the residual energy ($ECRE_{i,z}$) is obtained using Equation (11). The damage indicator $I_{D,i}$ for the i^{th} subdomain is then calculated as the sum of normalized residual energy for all *m* modes. The flowchart for this two-step ECRE-based damage detection procedure is shown in Figure 1 and 2.

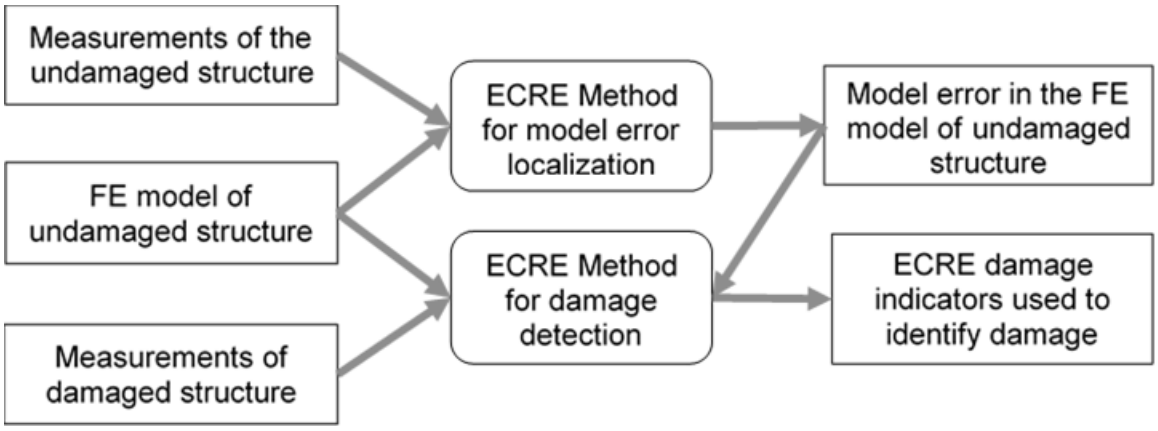

Figure 2.1. Framework of the ECRE-based damage detection method.

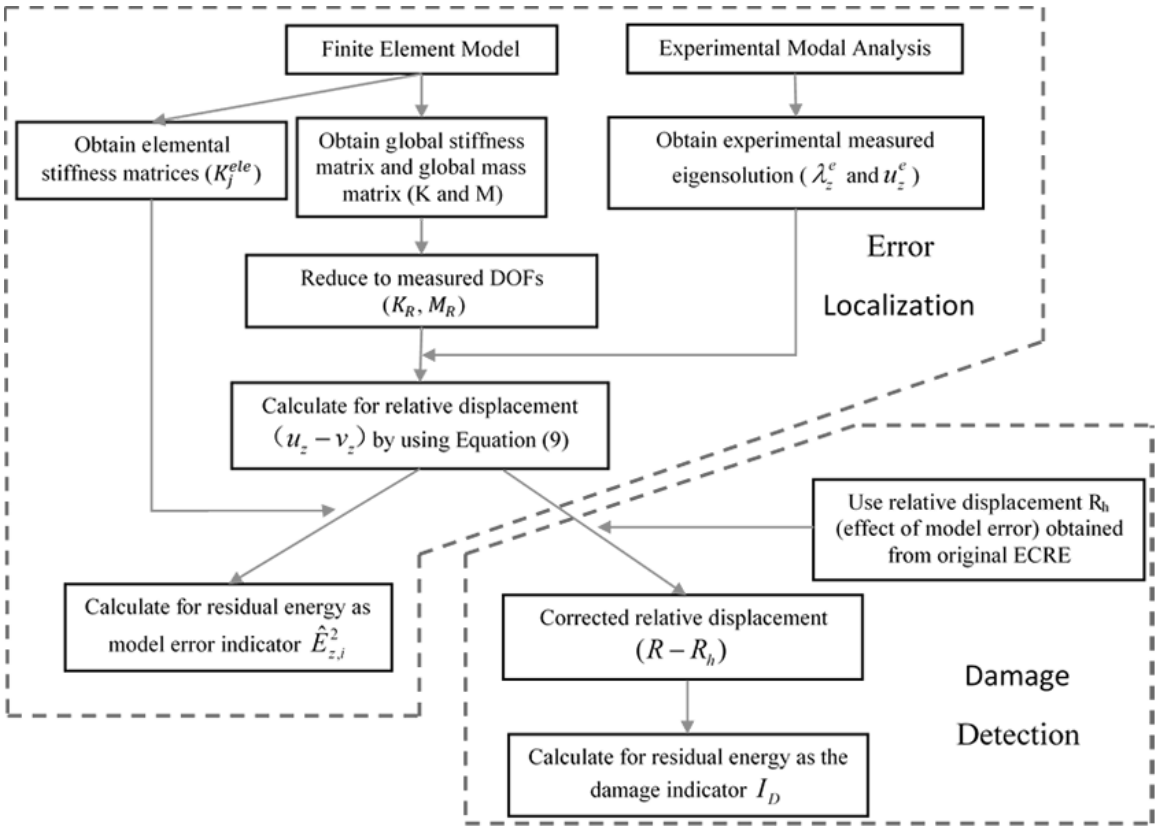

Figure 2.2. ECRE error localization and damage detection flowchart.

2.2.3 Notional proof-of-concept example

In this section, the two-step ECRE-based damage detection procedure is demonstrated on a controlled academic example using a FE model of a simply supported beam developed in ANSYS 14.0 with BEAM188 elements. The beam is discretized into 50 elements, which are grouped into five separate segments as shown in Figure 3 (c) and (d). The properties of these segments are summarized in Table 1.

Table 1. Reference configuration of beam model

Symbol	Parameter	Value
L	Total length	10 m
b	Width of cross section	0.2 m
h	Height of cross section	0.1 m
ρ	Density	7830 kg/m^3
E	Young's modulus	210 GPa
E_e	Introduced model error	105 GPa
E_d	Introduced damage	105 GPa
ν	Poisson's ratio	0.33
N_{node}	Node number	51
N_{dof}	DOF number	300
N_e	Beam element number	50
N_m	Measured DOFs	49

Synthetic (i.e. simulated) experimental data, which represents the undamaged structure, is generated using the beam FE model with what we refer to as the *original* Young's modulus value. Next, an imperfect model is developed by assigning an incorrect (i.e. underestimated) Young's modulus value, E_e, for the fifth segment (40^{th}-50^{th} elements) as shown in Figure 3 (c). Introducing a controlled model imperfectness was necessary for us to evaluate the ability of the two-step ECRE method to correctly identify damage even with an imperfect FE model. Finally, another FE model is developed to represent the (hypothetical) damaged beam. The damage is simulated by reducing the Young's modulus, E_d, in the first segment (1^{th}-10^{th} elements) of the initial FE beam model (Figure 3 (d)). This model is then used to generate synthetic experimental data representing the damaged structure without the consideration of experimental noise.

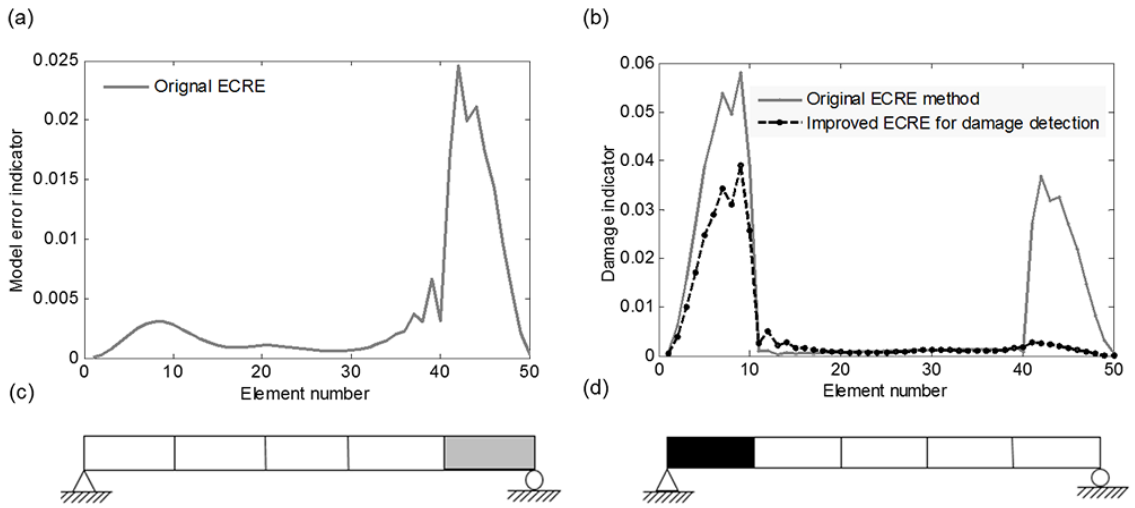

Figure 2.3. Results from simply supported beam simulation: (a) ECRE for localization purpose; (b) ECRE damage detection method for the gray line is the result from direct application of ECRE; dashed line is the result from the proposed improved ECRE method; (c) simply supported beam with model error between 40th - 50th elements; (d) simply supported beam with damage between 1st - 10th elements, the gray block represents the segment with model error while the black block represents the damaged segment.

Model error localization

Modal analysis is first carried out to obtain the synthetic experimental natural frequencies and mode shapes from the undamaged beam (this is in lieu of experimentally measured quantities as this is an academic example). The first 10 bending modes are obtained at 10 points evenly spaced across the length of the beam. The relative displacement field between the imperfect FE model and synthetic experimental measurements from the undamaged beam are then calculated using Equation (7). Figure 3 (a) shows the model error localization (obtained through Equation (8)), which is the total model error normalized with respect to the total system energy (i.e. $\boldsymbol{u}_z^T \boldsymbol{K}\boldsymbol{u}_z + \lambda_z^e \boldsymbol{u}_z^T \boldsymbol{M}\boldsymbol{u}_z$). This result illustrates the first step of the ECRE-based damage detection that is quantifying

the model error indicator. It can be seen in Figure 3 (a) that a higher model error is identified in beam elements of the fifth segment (the segment with the erroneous parameter value) than that in the rest of beam elements.

Damage detection

Using Equation (7), the relative displacement field between the FE model of the undamaged beam and the synthesized experimental measurements from the damaged beam is calculated. The solid gray line in Figure 3 (b) represents the damage detected using the original ECRE method without the consideration of the intrinsic model error. As shown in this figure, the identified residuals represent the combined effect of model errors and structural damage making it difficult to distinguish between the two, thus leading to false diagnosis of model error as damage.

On the other hand, our proposed two-step approach accounts for the model error in the FE model of undamaged structure by calculating the damage indicator with the corrected relative displacement using Equations (11) and (12). The resulting ECRE-based damage detection is plotted as the dashed line in Figure 3 (b). Evident in this figure, the simulated damage is identified successfully on the first segment of the beam with a negligible elemental residual error on other elements. This indicates that the proposed ECRE-based damage detection can accurately detect damage even if the reference FE model is imperfect.

2.3 Application: Two-story steel frame with connection damage

2.3.1 Steel frame laboratory specimen

In this section, we apply the proposed ECRE-based damage detection technique to identify the damage of a two-story single bay steel frame made of mild steel. The test frame is built using 5.08 cm × 0.32 cm angles for the four columns that are each 63.50 cm in length. The eight beams are each 64.45 cm in length made of 5.08 cm × 0.25 cm flat stock. All beams and columns are connected at 60.96 cm on center using two vertically aligned 2.54 cm spaced, grade 5, and 0.64 cm common threaded bolts. The base of each column is connected to a 15.24 cm × 15.24 cm × 1.27 cm steel plate using two 5.08 cm × 5.08 cm × 0.32 cm steel angles and four 0.64 cm bolts for each column and the corresponding plate is secured to a 20.32 cm × 10.16 cm × 1.27 cm steel plate anchored to a concrete slab serving as a rigid base. All bolts are given an initial torque of 15.82 Nm. Two 60.96 cm × 60.96 cm × 2.54 cm wood plates are mounted to mimic diaphragm action with the edge of the plates bolted into the four beams. The fully assembled frame is shown in Figure 4 (a). The details of the base connection and beam-column connection (before the wood plates are mounted) are shown in Figure 5.

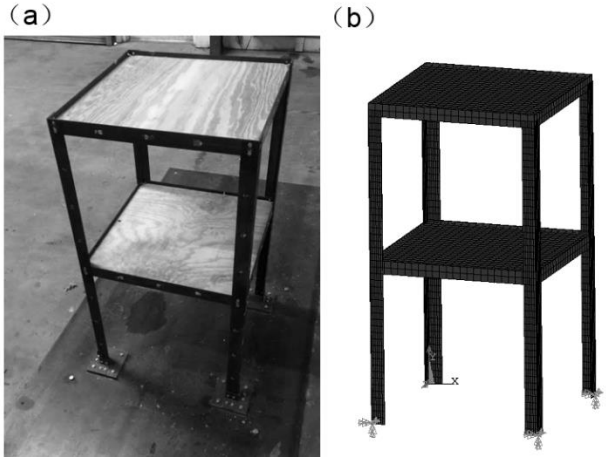

Figure 2.4. (a) Assembled steel frame model with wood floor mounted to both floors; (b) extruded view of FE model.

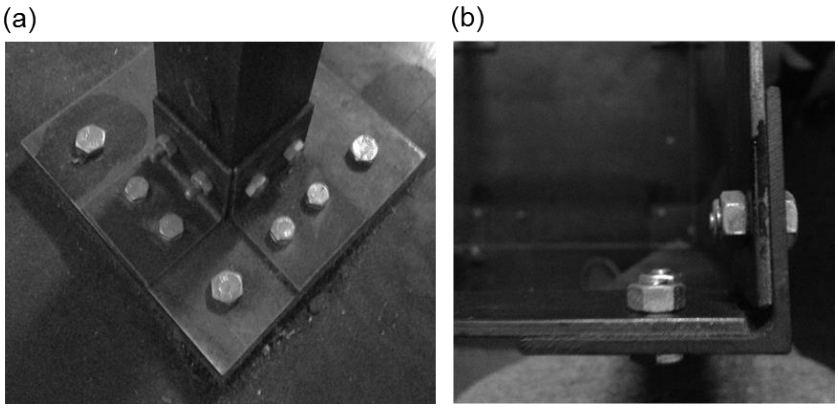

Figure 2.5. The details of (a) base connection; (b) the details of beam-column connection before the wood plates are mounted.

2.3.2 Development of the reference FE model of undamaged frame

The numerical model of the undamaged steel frame is developed in the FE analysis program ANSYS 14.0 using BEAM188 elements for all beams and columns and SHELL63 elements for all wood plate diaphragms as shown in Figure 4 (b). Base connections of the steel frame are idealized as fixed connections by restraining all the translational and rotational DOFs in x, y and z-axes. All beam-column connections are assumed to be rigid;

the wood plate and steel beams are assumed to be in full contact (see Table 2 for the reference configuration of the steel frame model).

Table 2. Reference configuration of steel frame model

Symbol	Parameter	Value
D_s	Steel density	7830 kg/m^3
D_w	Wood density	608 kg/m^3
E_s	Young's modulus of steel	210 GPa
E_w	Young's modulus of wood	11 GPa
ν_s	Poisson's ratio of steel	0.33
ν_w	Poisson's ratio of wood	0.35
N_{node}	Number of nodes	1630
N_{dof}	Number of DOF	8604
N_e	Number of Beam element	452
N_m	Measured DOFs	64

To ensure the numerical solutions' accuracy, a mesh-convergence study is completed to determine the appropriate mesh size (Roache 1994). Natural frequencies of the first twelve mode shapes are calculated for three mesh grids (coarse, medium and fine). With a correction applied to the fine grid solution, an extrapolated exact solution can then be obtained by using Richardson extrapolation approach. With 17 elements per beam/column, all modes of interest reached a relative error level below 1%, which is calculated between natural frequencies prediction and extrapolated exact solution. However, a finer mesh grids of 24 elements per beam are selected to match the measurement points on the FE model with the measurement points on the laboratory specimen. The first four identified mode shapes, shown in Figure 6, are used for the damage detection procedure.

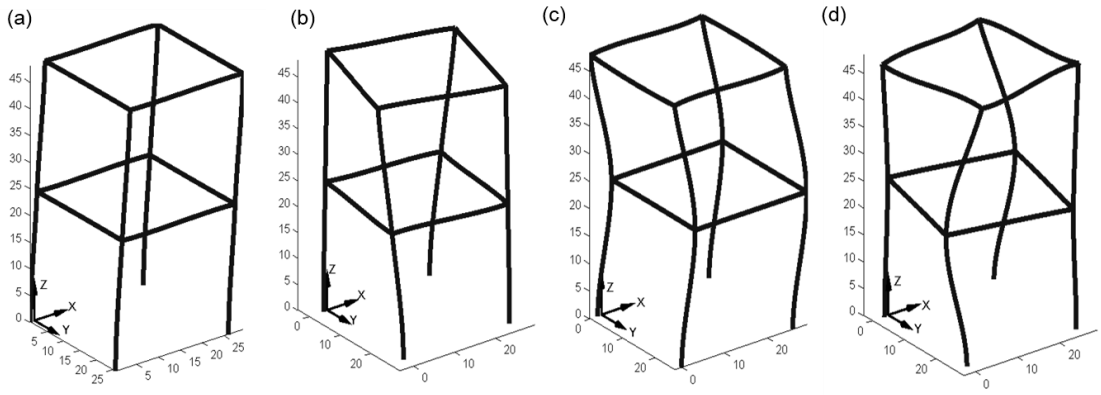

Figure 2.6. The first four mode shapes obtained by the FE model: (a) the first mode shape; (b) the second mode shape; (c) the third mode shape; (d) the fourth mode shape (the natural frequencies are listed in Table 3).

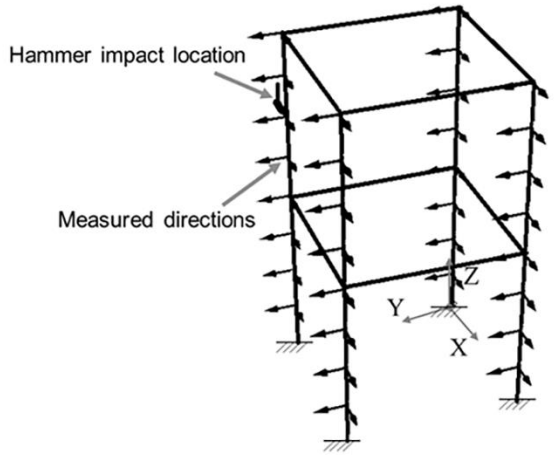

Figure 2.7. Measurement grid and hammer impact location.

Table 3. A comparison of the natural frequencies between the experimental measurement and numerical model of healthy structure.

Mode number	Numerical model prediction (Hz)	Experimental measurement (Hz)	% Difference
Mode1	19.7	21.3	7.5%
Mode2	35.1	30.3	-15.8%
Mode3	69.1	88.1	21.6%
Mode4	124.1	134.4	7.7%

2.3.3 Experimental campaign

Based upon the initial frequencies and modes shapes extracted from the FE model, an impact hammer test is developed with 64 uniaxial measurement points uniformly distributed along the four columns (at 32 locations with one measuring in the x direction and one measuring the y direction) (Figure 7). The data acquisition system is set to record in the frequency range 0-500 Hz with a measurement duration of 3.2 seconds. The experiment is completed in four setups by roving the accelerometer location and/or direction of each setup. Both the measurement grid and the locations of the hammer impact configuration are shown in Figure 7.

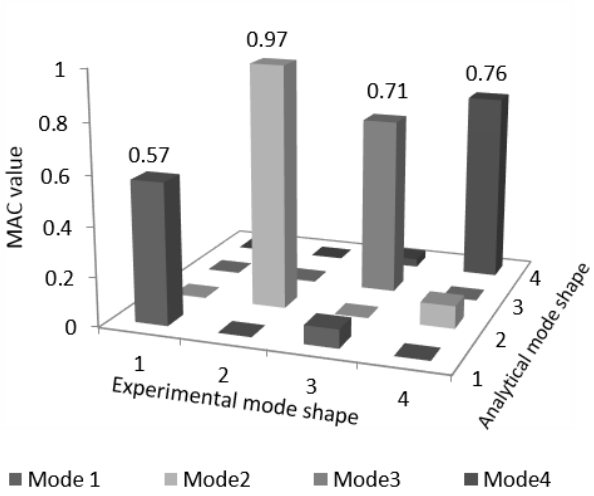

Figure 2.8. MAC correlation for the first four modes.

The measured natural frequencies for the first four modes are compared with calculated natural frequencies as listed in Table 3. To ensure that each mode is properly paired, the Modal Assurance Criterion (MAC) (Allemang and Brown 1982; Allemang 2003) between numerically generated mode shapes and experimentally measured mode shapes is calculated as shown in Figure 8. From the MAC plot, the first diagonal value (0.57) indicates a relatively low correlation between the experimental and analytical first mode shape, possibly due to the imprecise modeling of the contact between the steel beam and wood plate.

Controlled damage was introduced to the steel frame by removing select bolts and angles and then the experimental campaign is repeated (Zadoks and Yu 1997; Jiang et al. 2003). Three distinct damage states are considered as shown in Figure 9. The first damage state is the full damage applied at one base connection by removing all the bolts and angles. The second damage state has the same damage location as the first, but less severe damage as the two angles attached to the base plate are retained but the bolts attached to the column are removed. In this damage state, with the angles remaining, the translational DOFs in horizontal directions are partially restrained due to friction. In the third damage state, damage is introduced to a connection at the top level of the steel frame where four bolts that connect the beams to column are removed.

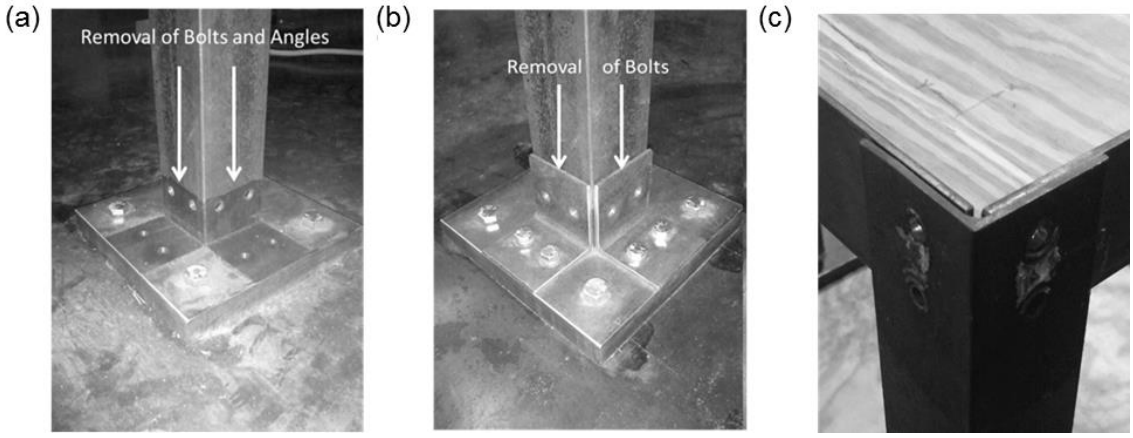

Figure 2.9. Three damage states with controlled damage introduced: (a) the removal of all bolts and angles at one base connection; (b) the removal of all bolts at one base connection; (c) the removal of all bolts at one top connection.

The first four natural frequencies of the steel frame, before and after the damage is introduced, are listed in Table 4. While the natural frequencies for damage state #1 and #2 show a significant reduction from those of the steel frame in the healthy state, the natural frequencies for damage state #3 (especially those that correspond to modes 2-4) show a negligible change as considerably less severe damage is introduced in this state.

Table 4. A comparison of the experimental measured natural frequencies for healthy and damage states (ω_n is the measured natural frequency).

Mode number	Healthy state	Damage state1		Damage state 2		Damage state 3	
	ω_n (Hz)	ω_n (Hz)	Difference	ω_n (Hz)	Difference	ω_n (Hz)	Difference
Mode1	21.3	17.8	-16.2%	18.8	-11.8%	20.3	-4.4%
Mode2	30.3	28.1	-7.2%	29.4	-3.1%	30.6	1.0%
Mode3	88.1	82.8	-6.0%	85.0	-3.5%	88.1	0.0%
Mode4	134.4	122.5	-8.8%	130.3	-3.0%	134.7	0.2%

2.3.4 Damage detection using ECRE

Upon obtaining natural frequencies and mode shape vectors from both the FE model and the experiments in the laboratory, we employed the ECRE-based damage detection algorithm to localize the damage for the three aforementioned damage states. The global stiffness and mass matrices of the undamaged frame, extracted from the FE model, are reduced to the measured DOFs through Guyan reduction. Next, the relative displacement vector is calculated from the ECRE optimization (recall Equation (6)). The elemental stiffness matrices (for all finite elements) are also extracted from the FE model. These elemental matrices are used to calculate residual energy in elements, and in turn, the damage indicators.

In addition, for comparison, synthetic measurements are generated from the FE model for each of the damage scenarios. The synthetically measured mode shape vectors of the FE model are obtained at nodes identical to those of the sensor locations on the test structure. The length of the mode shape vector is therefore kept identical between experimental and synthetic measurements. The synthetic data are used to obtain a reference damage indicator for evaluating the effect of (i) the model error, (ii) the unavoidable limitations on the number of measurement points, and (iii) the experimental noise on the success of the proposed damage detection method.

2.4 Results: Two-story steel frame with connection damage

2.4.1 Damage State #1: Removal of all bolts and angles at one base connection

The first damage state involves the removal of all bolts and angles at one of the column base connections, thus turning the column base into a free support. The constitutive error distribution calculated using measurements collected from the scaled steel frame in the laboratory are shown in Figure 10 (a). In this figure, the darker region with a maximum damage indicator of 0.25 corresponds to the damaged base connection.

To evaluate the degrading effects of experimental uncertainties on the damage indicators, constitutive errors calculated using experimental measurements are compared against those obtained using synthetic experiments. Here, the damage is simulated in the FE model by removing all constraints at the damaged base and representing the connection as a free support. Synthetic experimental measurements are generated based on 32 nodes corresponding to horizontal translational DOFs without the consideration of experimental noise. The constitutive errors obtained by using synthetic data are plotted in Figure 10 (b). Similarly, the darker region indicates the correct location of the introduced damage. However, this time, the maximum value for the damage indicator is 0.7, significantly higher than 0.25, the value obtained when laboratory experiments were used. This reduction in the damage indicator values can be explained in part by the measurement noise and in part by the fact that the FE model of the steel frame is an idealized representation of

reality. Although the model error correction process is applied through the two-step ECRE procedure to reduce the effect of model error, the differences between the synthetically generated and experimentally measured mode shapes (due for instance to idealized beam-column connections; omitted energy dissipation; and simplified representation of pre-stress forces at the angle brackets (Doebling et al. 1998; Aktan et al. 1994; Bezerra et al. 2008; Atamturktur et al. 2012; Hegenderfer and Atamturktur 2013)) may not be fully addressed. This comparison demonstrates the degrading effect of experimental noise as well as the model inaccuracy on the damage localization. The influence of experimental uncertainty will be further investigated in Section 5.

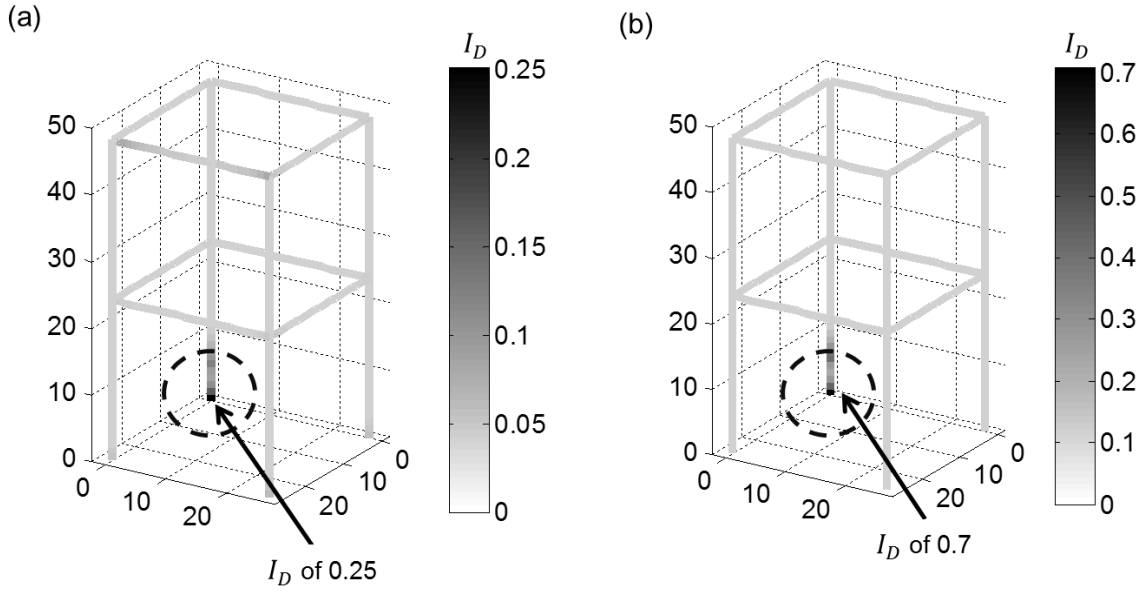

Figure 2.10. ECRE result of damage state 1 using both (a) experimental data and (b) synthetic data; - - dashed line indicates the actual damage location

2.4.2 Damage State #2: Removal of all bolts at one base connection

The damage is introduced by removing all bolts except for the two angles attached to the base plate at the same location as the damage state #1. The second damage state allows us to test the ability of ECRE-based damage detection to indicate the relative severity of damage. In this damage state, the maximum damage indicator of 0.07 is successfully located at the damaged base connection, however, false positive indications (i.e. damage indicators with high values at locations where there is no damage) also appear around the connections of the top floor as seen in Figure 11 (a). As expected, the maximum damage indicator value calculated for this damage state (which has less severe damage compared to damage state #1) is lower (0.07) than that obtained for damage state #1 (0.25).

This reduction is promising for the potential of the ECRE to quantitatively indicate the relative severity of damage.

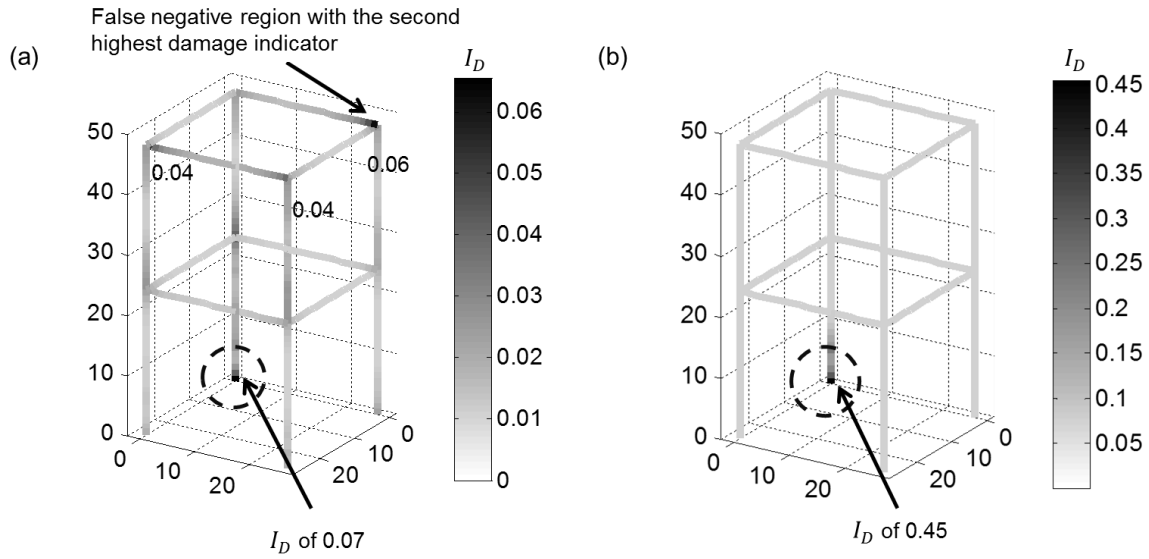

Figure 2.11. ECRE result of damage state 2 using both (a) experimental data and (b) synthetic data; - - dashed line indicates the actual damage location.

The damage indicator is recalculated using synthetic measurements to evaluate the combined effect of experimental uncertainties and inaccuracies in FE model predictions. While generating the synthetic measurements (which have no experimental uncertainty), the base connection (with angles but without any bolts) is treated as a connection with only translational constraints in the x and y direction by removing the rotational constraints.

As seen in Figure 11 (b), the constitutive errors localized by the ECRE method using synthetic measurements successfully identifies the actual damage location. It is observed that false negative indications at the upper-corner connections (recall Figure 11 (a)) disappear. This is mainly due to the fact that synthetic, noise-free measurements that

generated from the FE model are used so that the effect of both model inaccuracy and experimental uncertainty is eliminated. Once again, compared to the results obtained for damage state #1, there is an evident reduction in the damage indicator values for damage state #2. Specifically, when synthetic data are used for both state #1 and state #2, the maximum value of the damage indicators is reduced from 0.7 to 0.45.

2.4.3 Damage State #3: Removal of all bolts at one top floor connection

The aim of this damage state is to test the performance of the ECRE-based damage detection method on identifying damage in the superstructure of the frame. Constitutive errors identified using experimental measurements are shown in Figure 12, where the true damaged location is correctly identified. There are, however, two false negatives with lower constitutive errors located at the connections of the top floor. In this damage state, synthetic measurements are not applied as the reference to compare with the experimental results because the idealized top connections of the FE model cannot be used to fully describe the behavior of damaged connections in the actual steel frame.

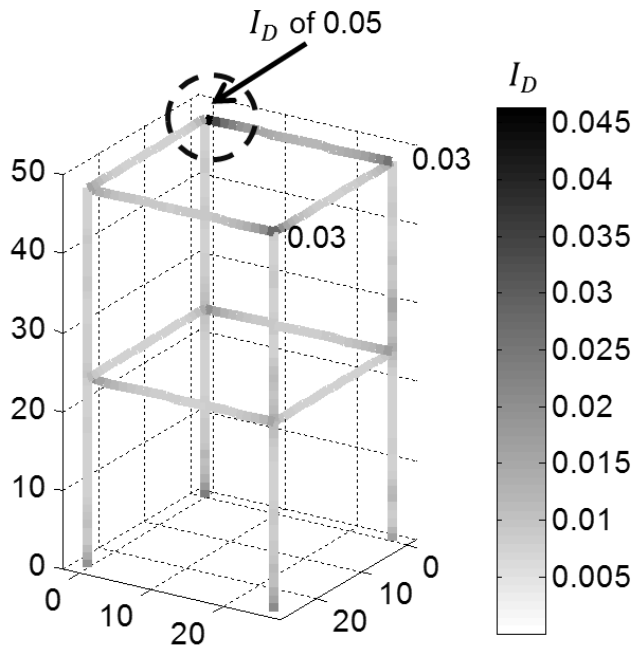

Figure 2.12. ECRE result of damage state 3 using experimental data; - - dashed line indicates the actual damage location.

2.5 Further discussions on ECRE-based damage detection

The success of the ECRE-based damage detection depends strongly on the quantity (number and placement of the sensors) as well as the quality (uncertainty of the measurements). This section details our evaluation of the effect of both quantity and quality of damage detection experiments.

2.5.1 Quantity of experiments: Effect of the numbers of measurement points

In this section, the influence of number of measurement points on the effectiveness of damage detection is evaluated, focusing on damage state #1 using synthetic measurements. Here, we use synthetic measurements so that the experimental uncertainty and model inaccuracy are not factors, and the comparison is focused on the number and

spatial coverage of measurement DOFs. The initial number of measurement points n is reduced first from 64 to 32 and then further reduced to 16. The proposed ECRE-based damage detection method is able to successfully identify the damage location with as few as 32 measurement points (1.4% of the total number of FE model DOFs).

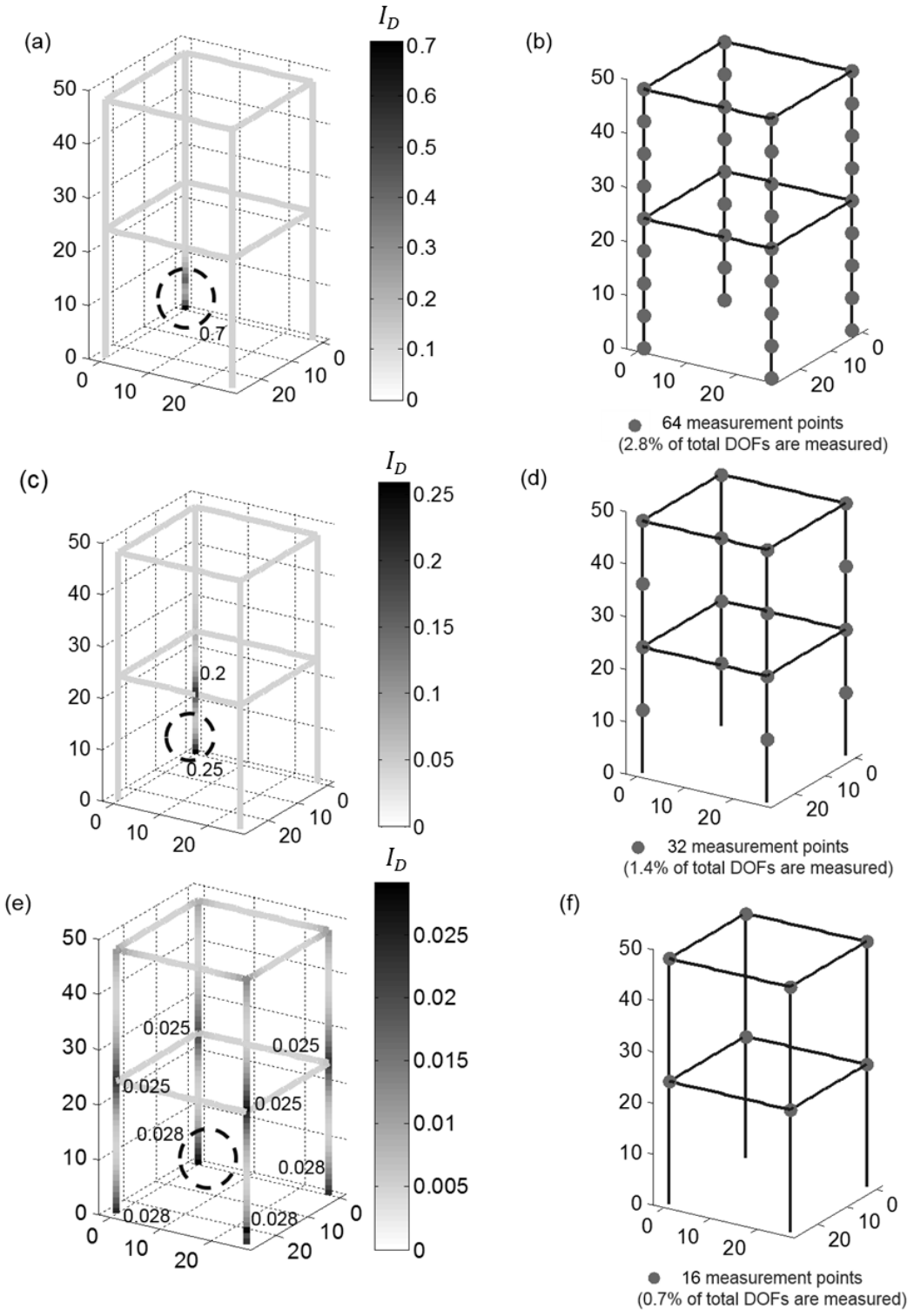
(a)
I_D
0.7
0.6
0.5
0.4
0.3
0.2
0.1
0
(b)
64 measurement points
(2.8% of total DOFs are measured)
(c)
I_D
0.25
0.2
0.15
0.1
0.05
0
0.2
0.25
(d)
32 measurement points
(1.4% of total DOFs are measured)
(e)
I_D
0.025
0.02
0.015
0.01
0.005
0
0.025
0.028
(f)
16 measurement points
(0.7% of total DOFs are measured)

Figure 2.13. The effect of the number of measured DOFs on the ECRE result plot of damage state 1: (a) ECRE result using synthetic data of 64 measurement points; (b) locations of 64 measurement points; (c) ECRE result using synthetic data of 32 measurement points; (d) locations of 32 measurement points; (e) ECRE result using synthetic data of 16 measurement points; (f) locations of 16 measurement points; - - dashed line indicates the actual damage location.

2.5.2 Quality of experiments: Effect of experimental uncertainty

In this section, the influence of experimental uncertainty on the effectiveness of damage detection is detailed with a particular emphasis on damage state #1. The experimental uncertainty is represented by adding $\pm$ 5% Gaussian noise to the experimentally measured mode shapes as suggested in Meng et al. (2004) and Ge et al. (2010). A total of 100 *contaminated* mode shape realizations each with randomly generated noise are obtained. For each set of the contaminated modes shape vectors, an array of damage indicators is calculated, which are then averaged for all 100 realizations as shown in Figure 14 (a). As evidenced by Figure 14 (a), the distribution of averaged damage indicators on the frame is capable of localizing the damage at the base of the damaged column.

However, compared to the constitutive errors calculated by using noise-free synthetic measurements (shown earlier in Figure 10 (b)), the maximum damage indicator is observed to decrease from 0.25 to 0.15.

The procedure is repeated for the increased Gaussian noise of 15%, 25% and 35%, as shown in Figures 14 (b), (c) and (d), respectively. Here, an increase in the number of

false positive indications is evident for increasing levels of experimental uncertainty and in the case with the highest experimental noise of 35% as shown in Figure 14 (d), the proposed method can no longer identify the actual location of damage. In Figure 15, the inverse proportional relationship between the value of maximum damage indicators and the experimental uncertainty is demonstrated with more cases with experimental noise from 5% to 35%. The error bars in Figure 15 represent the uncertainty of the calculated maximum damage indicators for the different percentage of experimental noise being introduced. As the experimental noise increases beyond 20%, it is observed in Figure 15 that the maximum damage indicators converge because the experimental uncertainty becomes the main source of residual energy. Hence, the damage indicators begin to scatter throughout the model making the damage location indistinguishable. This inverse proportional relationship and convergence effect may lead future research on creating a confidence factor of the proposed approach.

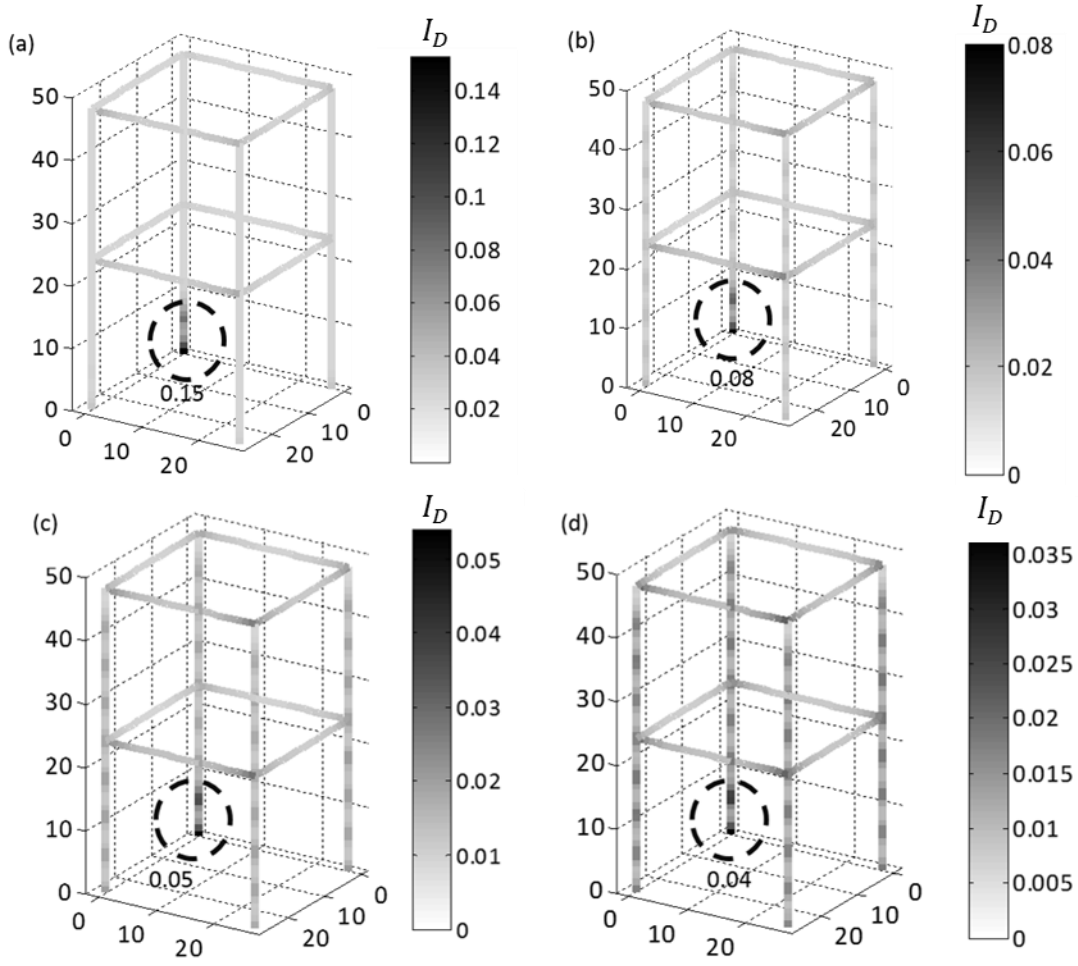
(a)
I_D
0.14
0.12
0.1
0.08
0.06
0.04
0.02
0.15
(b)
I_D
0.08
0.06
0.04
0.02
0
0.08
(c)
I_D
0.05
0.04
0.03
0.02
0.01
0
0.05
(d)
I_D
0.035
0.03
0.025
0.02
0.015
0.01
0.005
0
0.04

Figure 2.14. ECRE result plots of damage state 3 using four different levels of contaminated experimental data: (a) 5% noise added; (b) 15% noise added; (c) 25% noise added; (c) 35% noise added; - - dashed line indicates the actual damage location.

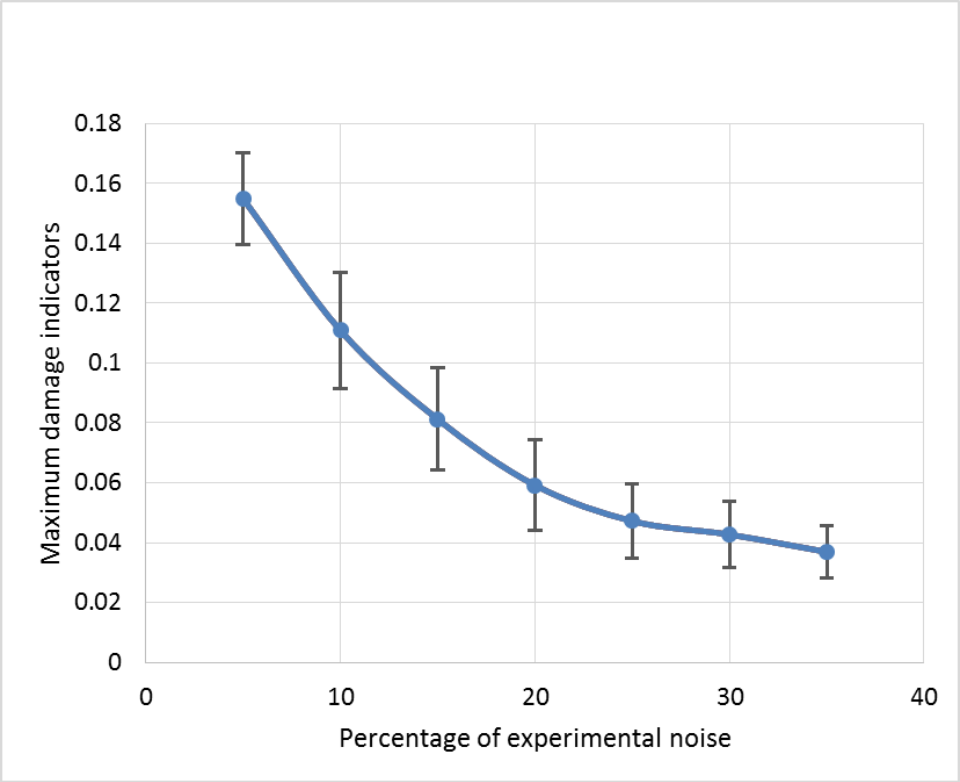

Figure 2.15. The relationship between experimental uncertainty and maximum damage indicators.

2.6 Conclusions

A novel, approach for damage detection is proposed by integrating the mechanistic concept of ECRE into the model-based damage detection paradigm by explicitly considering the underlying dynamic behavior of linear elastodynamic systems. The concept of ECRE, when applied in FE model calibration, localizes the residual errors that reflect the discrepancies between experimental measurements and model predictions corresponding to the same structure. For the purpose of damage detection, however, a two-

step approach is needed: the first step determines the constitutive error in the FE model of the undamaged system; and the second step employs these residual errors to account for the model's imperfection and finally obtains the residual energy (damage indicator) between the FE model of the undamaged system and the experimental data of the damaged system. In this paper, the ECRE-based damage detection method is demonstrated on a steel frame with connection damage. However, the applicability of the proposed approach is not limited to steel structures. The presented approach can be applied to many different types of structure for which the experimental modal data is available.

Another advantage of the ECRE-based damage detection method over traditional damage detection methods is its inherent ability to identify the damage location—unlike many model updating-based approaches which require an additional step after the damage is detected. Furthermore, as expected, the damage indicator values exhibit a proportional relationship with the severity of the damage given the availability of a sufficient number of measurement points with low enough experimental uncertainty. Hence, given the suitable conditions, the proposed method can also determine the relative severity of the damage.

Although the two-step ECRE-based damage detection method is most promising, it is also strongly dependent on the sensor placement (both number and distribution) as well as the level of experimental uncertainty. However, with recent trends towards full-

field surface vibration measurement techniques that utilize for instance laser Doppler vibrometers (Castellini et al. 2006) or high-frequency cameras (Chen et al. 2015), the future of vibration testing has the potential to provide the needed quality and quantity of data for ECRE to be successful in identifying, locating and determining the severity of damage.

References

Aktan, A. E., Lee, K. L., Chuntavan, C., & Aksel, T. (1994). Modal testing for structural identification and condition assessment of constructed facilities. *Proceedings-spie the International Society for Optical Engineering*, 462-462.

Allemang, R. J. (2003). The modal assurance criterion–twenty years of use and abuse. *Sound and vibration, 37*(8), 14-23.

Allemang, R. J., & Brown, D. L. (1982). A correlation coefficient for modal vector analysis. In *Proceedings of the 1st international modal analysis conference*, 110-116.

Atamturktur, S., Hemez, F. M., & Laman, J. A. (2012). Uncertainty quantification in model verification and validation as applied to large scale historic masonry monuments. *Engineering Structures, 43*, 221-234.

Baruch, M. (1982). Optimal correction of mass and stiffness matrices using measured modes. *AIAA journal, 20*(11), 1623-1626.

Berman, A. & Flannelly, W. G. (1971). Theory of incomplete models of dynamic structures. *AIAA journal, 9*(8), 1481-1487.

Berman, A., & Nagy, E. J. (1983). Improvement of a large analytical model using test data. *AIAA journal, 21*(8), 1168-1173.

Bezerra, A. C., Vieira, L. C., Rade, D. A., & Scotti, A. (2008). On the influence of welding residual stresses on the dynamic behavior of structures. *Shock and Vibration, 15(3-4),* 447-458.

Bi, S., Atamturktur, S., & Deng, Z. (2014), Stochastic model updating using distance discrimination analysis. *Chinese Journal of Aeronautics (Elsevier), 27*(5), 1188-1198.

Carr, G. E., & Chapetti, M. D. (2011). On the detection threshold for fatigue cracks in welded steel beams using vibration analysis. *International Journal of Fatigue, 33*(4), 642-648.

Castellini, P., Martarelli, M., & Tomasini, E. P. (2006). Laser Doppler Vibrometry: Development of advanced solutions answering to technology's needs. *Mechanical Systems and Signal Processing, 20*(6), 1265-1285.

Charbonnel, P. É., Ladevèze, P., Louf, F., & Le Noac'h, C. (2013). A robust CRE-based approach for model updating using in *situ* measurements. *Computers & Structures, 129,* 63-73.

Chen, J. G., Wadhwa, N., Cha, Y. J., Durand, F., Freeman, W. T., & Buyukozturk, O. (2015). Modal identification of simple structures with high-speed video using motion magnification. *Journal of Sound and Vibration*, *345*, 58-71.

De Smith, M. J. (2006). Determination of gradient and curvature constrained optimal paths. *Computer-Aided Civil and Infrastructure Engineering*, *21*(1), 24-38.

Decouvreur, V., Ladevèze, P., & Bouillard, P. (2008). Updating acoustic models: a constitutive relation error approach (Doctoral dissertation, PhD thesis, Université Libre de Bruxelles).

Deraemaeker, A., Ladevèze, P., & Leconte, P. (2002). Reduced bases for model updating in structural dynamics based on constitutive relation error. *Computer Methods in Applied Mechanics and Engineering*, *191*(21), 2427-2444.

Doebling, S. W., Farrar, C. R., & Prime, M. B. (1998). A summary review of vibration-based damage identification methods. *Shock and vibration digest*, *30(2)*, 91-105.

Farrar, C. R., Hemez, F. M., Shunk, D. D., Stinemates, D. W., Nadler, B. R., & Czarnecki, J. J. (2004). A review of structural health monitoring literature: 1996-2001 (p. 303). Los Alamos, NM: Los Alamos National Laboratory.

Faverjon, B., & Sinou, J. J. (2008). Robust damage assessment of multiple cracks based on the frequency response function and the Constitutive Relation Error updating method. *Journal of Sound and Vibration*, *312*(4), 821-837.

Friswell, M. I. (2007). Damage identification using inverse methods. *Philosophical Transactions of the Royal Society A: Mathematical, Physical and Engineering Sciences, 365*(1851), 393-410.

Friswell, M., & Mottershead, J. E. (1995). Finite element model updating in structural dynamics. *Springer Science & Business Media*. *38.*

Ge, M., Lui, E. M., & Khanse, A. C. (2010). Non-proportional damage identification in steel frames. *Engineering Structures, 32*(2), 523-533.

Guyan, R. J. (1965). Reduction of stiffness and mass matrices. *AIAA journal, 3(2),* 380-380.

Hegenderfer, J., & Atamturktur, S. (2013). Prioritization of code development efforts in partitioned analysis. *Computer‐Aided Civil and Infrastructure Engineering, 28*(4), 289-306.

Isasa, I., Hot, A., Cogan, S., & Sadoulet-Reboul, E. (2011). Model updating of locally non-linear systems based on multi-harmonic extended constitutive relation error. *Mechanical Systems and Signal Processing, 25*(7), 2413-2425.

Jafarkhani, R., & Masri, S. F. (2011). Finite element model updating using evolutionary strategy for damage detection. *Computer‐Aided Civil and Infrastructure Engineering, 26*(3), 207-224.

Jiang, Y., Zhang, M., & Lee, C. H. (2003). A study of early stage self-loosening of bolted joints. *Journal of Mechanical Design, 125(3),* 518-526.

Kammer, D. C. (1991). Sensor placement for on-orbit modal identification and correlation of large space structures. *Journal of Guidance, Control, and Dynamics*, *14*(2), 251-259.

Ladevèze, P., & Leguillon, D. (1983). Error estimate procedure in the finite element method and applications. *SIAM Journal on Numerical Analysis*, *20*(3), 485-509.

Ladevèze, P., Moës, N., & Douchin, B. (1999). Constitutive relation error estimators for (visco) plastic finite element analysis with softening. *Computer Methods in Applied Mechanics and Engineering, 176*(1), 247-264.

Lin, P. T., & Gea, H. C. (2013). A gradient-based transformation method in multidisciplinary design optimization. *Structural and Multidisciplinary Optimization, 47*(5), 715-733.

Link, M., & Floressantiago, O. (1991). Updating and localizing structural errors based on minimization of equation errors. *In ESA, Spacecraft Structures and Mechanical Testing, 1,* 503-510.

Mottershead, J. E., & Friswell, M. I. (1993). Model updating in structural dynamics: a survey. *Journal of sound and vibration, 167(2),* 347-375.

Piranda, J., Lallement, G., & Cogan, S. (1991). Parametric correction of finite element models by minimization of an output residual: Improvement of the sensitivity method. In *Proc. of the 9th International Modal Analysis Conference*, 363-368.

Prabhu, S., Atamturktur, S., Brosnan, D., Messier, P., & Dorrance, R. (2014). Foundation settlement analysis of Fort Sumter National Monument: Model development and predictive assessment. *Engineering Structures, 65*, 1-12.

Roache, P. J. (1994). Perspective: a method for uniform reporting of grid refinement studies. *Journal of Fluids Engineering*, *116*(3), 405-413.

Salawu, O. S. (1997). Detection of structural damage through changes in frequency: a review. *Engineering Structures, 19*(9), 718-723.

Teughels, A., & De Roeck, G. (2004). Structural damage identification of the highway bridge Z24 by FE model updating. *Journal of Sound and Vibration, 278*(3), 589-610.

Worden, K., & Burrows, A. P. (2001). Optimal sensor placement for fault detection. *Engineering Structures*, *23*(8), 885-901.

Wu, J. R., & Li, Q. S. (2006). Structural parameter identification and damage detection for a steel structure using a two-stage finite element model updating method. *Journal of Constructional Steel Research, 62(*3), 231-239.

Zadoks, R. I., & Yu, X. (1997). An investigation of the self-loosening behavior of bolts under transverse vibration. *Journal of sound and vibration, 208(2),* 189-209.

Zimmerman, D. C., & Kaouk, M. (1994). Structural damage detection using a minimum rank update theory. *Journal of Vibration and Acoustics, 116(2),* 222-231.

CHAPTER THREE

Extended Constitutive Relation Error Based Approach: The Role of Mass in Damage Detection

3.1 Introduction

As structural systems accumulate damage throughout their service life, their physical properties, such as stiffness, mass, and damping change, which in turn alters their vibration characteristics (Vandiver 1975; Kim and Bartkowicz 1993; Hemez and Farhat 1995; Worden et al. 2009; Atamturktur et al. 2013). The last three decades have seen a vast number of studies focused on measurements of vibration characteristics, such as natural frequencies, mode shapes, and damping ratios, to detect the onset and propagation of damage in a variety of structural systems (Doebling et al. 1998; Zou et al. 2000; Fugate et al. 2001). A popular class of damage detection techniques developed in these earlier studies, known as model-based techniques, implement a physics-based model of the engineering system, which is parameterized to represent potential damage to the system. These predefined parameters are selected to be indicative of the presence, location and severity of damage (Teughels and Roeck 2004; Kopsaftopoulos and Fassois 2010; Prabhu and Atamturktur 2013). Model-based techniques aim to achieve this through an inverse analysis that is conceived to reduce the discrepancies between the experiments and model

predictions (Doebling et al. 1998; Teughels and Roeck 2004; Lee et al. 2005; Prabhu and Atamturktur 2015; Hu et al. 2017).

As structural damage often affects the system's stiffness properties to a much greater extent than it affects the mass properties (Cawley and Adams 1979; Hearn and Testa 1991), these model-based techniques have traditionally hypothesized that the mass distribution of the system either remains unchanged or changes by a known quantity (Hassiotis and Jeong 1995; He and Zhu 2013). Consequently, many model-based damage detection approaches have focused solely on changes in the system behavior due to changes in the structural stiffness to detect damage (Zimmerman and Kaouk. 1994; Hassiotis and Jeong 1995; Lee et al. 2005).

One such model-based technique, the Extended Constitutive Relation Error (ECRE)-based damage detection, identifies damage using residual energy between the measurements obtained from the damaged physical system and the predictions of the numerical model of the undamaged system. The ECRE-based damage detection involves calculating the elemental residual energy of the undamaged structure using experimental measurements from the damaged structure. Then, damaged regions are localized by pinpointing the greatest disagreement between the model and the experiments represented by the calculated residual energy. While the ECRE approach has previously been applied to detect structural damage (Faverjon and Sinou 2009; Hu et al. 2017), it has been

implemented in a way where the residual energy was calculated solely considering the residual elastic forces without taking the residual inertial forces into account. However, there are two specific cases where considering the inertial forces becomes particularly beneficial in model-based damage detection. The first is when the damage alters the mass distribution of the system (Kosmatka and Ricles 1999), as in the case of a loss of structural components (Ma and Pines 2003), corrosion damage in metal structures (Maaddawy et al. 2005), and loss of non-structural material (Joukoski et al. 2009). The second case is when the mass distribution of the system is poorly known and hence, erroneously represented in the model as a result of, for instance, inappropriate simplifying assumptions (Berman 1979; Martin and Doyle 1996; Whalen et al. 2004) and hard-to-control variations in manufacturing or construction (Oberkampf et al. 2002). Considering the effect of mass stands to improve damage detection: in the former case, by accounting for the change in system's mass due to damage; and in the latter case, by accounting for modeling errors even when there is no change in the system's mass due to damage.

In this paper, an ECRE-based damage detection method is formulated to account for the residual unbalanced elastic and inertia forces that result from discrepancies between the measured and numerically generated displacement fields. These discrepancies in the displacement fields can then be combined with the system's stiffness and mass matrices to calculate the residual energy, which in turn allows us to pin-point the damage in the system.

Potential contributions to this calculated residual energy from modeling error may lead to false-positives in damage detection. If experimental measurements are available from the structure in both damaged and undamaged states, a correction step can be carried out to account for the potential contributions of modeling error to the calculated residual energy (Hu et al. 2017).

This paper is organized as follows. Section 2 overviews the theoretical background of the ECRE method considering both unbalanced elastic and inertial forces and describes the step-by-step procedure for the stiffness-and-mass ECRE-based damage detection method. In Section 3, a two-story steel frame case study structure and the development of its numerical model are discussed. In Section 4, the performance of the proposed approach is evaluated through a numerical example of a two-story steel frame with modeling error intentionally introduced in the mass distribution. Section 5 demonstrates the performance of this approach using the experimental measurements from the steel frame. The results obtained for damage scenarios of varying severity and location are discussed and compared against the stiffness-only ECRE-based damage detection. Finally, Section 6 draws the conclusion of this study and makes recommendations for future work.

3.2 Methodology

In the constitutive relation error method, the equations of interest (constitutive behavior relations, equations of motion, equilibrium equations, etc.) are grouped as reliable

and less reliable equations. Accordingly, an optimization problem is formulated to minimize the error in the less reliable equations under the constraint of the reliable equations using unknown admissible fields (Ladeveze 1999). Similarly, available experimental measurements are also grouped into reliable and less reliable observations. For instance, if experimental modal analysis is conducted, the mode shape vectors may be considered less reliable quantities compared to natural frequencies especially if only a limited number of measurement points are available on the structure. Common groups of reliable and less reliable equations and quantities from the pertinent literature are listed in Table 1 (Deraemaeker et al. 2002; Charbonnel et al. 2013).

Table 1. Common reliable and less reliable equations

	Numerical Model	Experimental Campaign
Reliable Equations and Quantities	Geometric Information Kinematic Equations Equilibrium Equations	Measured Natural Frequencies Sensor Locations and Directions Excitation Force Locations and Directions
Less Reliable Equations and Quantities	Constitutive Equations	Measured Mode Shapes

3.2.1 A generalized example for the constitutive relation error method

Let us consider a reference linear, elastic, and undamped structure within a domain Ω as shown in Figure 1. On the boundary $\partial\Omega$ of the domain, an excitation force F_d is applied on $\partial\Omega_1$ and the displacement U_d is measured on $\partial\Omega_2$. f_d is the body force in the domain Ω. Here, the reliable equations can be taken as the kinematic and the equilibrium equations; and the less reliable equation as the constitutive relations.

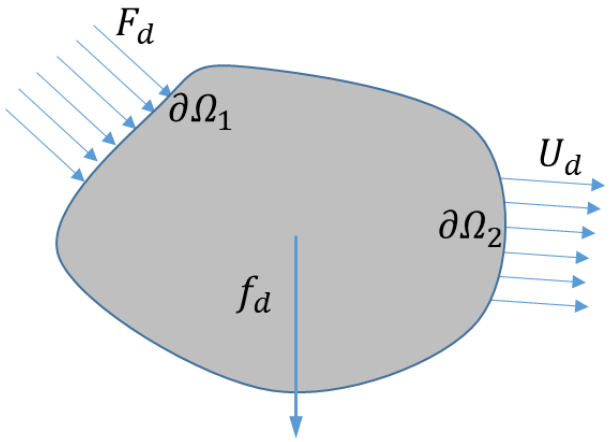

Figure 3.1. The reference structure.

The reliable kinematic equation can be expressed as:

$$U_d = U \tag{1}$$

where U is the admissible field representing the measured displacement. If experimental uncertainty is not considered, the admissible field U would be equal to U_d ,

The reliable equilibrium equation can be expressed as:

$$-\int_{\Omega} \mathrm{tr}[\sigma\varepsilon(U)]\mathrm{d}\Omega + \int_{\Omega} f_d \cdot U\mathrm{d}\Omega + \int_{\Omega_1} F_d \cdot U\mathrm{d}\Omega_1 = \int_{\Omega} \rho\ddot{U} \cdot U\mathrm{d}\Omega \tag{2}$$

where $\mathrm{tr}[...]$ is the sum of the diagonal entries of matrix $[\sigma\varepsilon(U)]$; σ and ε are the stress and strain tensors, respectively; ρ is the density; and $\ddot{U}$ is the acceleration response of the structure.

For linear materials, the stress-strain constitutive relation can be defined using Hooke's law as expressed below:

$$\sigma = \mathbf{H}\varepsilon(V) \tag{3}$$

where **H** is the Hooke's operator; V is the admissible field representing the model predicted response due to unbalanced elastic force. If there is a difference in the stiffness distribution between the numerical model and the physical system, the model predicted response V would be different than the admissible field representing the measured displacement U, leading to a residual error $(U-V)$.

A solution can be sought that exactly satisfies the reliable kinematic equation (Equation (1)) and equilibrium equation (Equation (2)), while minimizing the error in the constitutive relation (Equation (3)). The constitutive relation error due to unbalanced elastic forces can then be formulated based on the distance between the two admissible fields that represent the measured (U) and the model predicted (V) response as expressed below (Ladeveze 1999):

$$\xi^2(U,V) = \int_\Omega \mathrm{tr}[(\mathbf{H})(\varepsilon(V)-\varepsilon(U))^*(\varepsilon(V)-\varepsilon(U))]\mathrm{d}\Omega \tag{4}$$

where "*" is the complex conjugate.

To account for the mass in the reference problem, one must also consider the constitutive relation error due to unbalanced inertial forces:

$$\Gamma = -\rho\omega^2 W \tag{5}$$

where ω is the angular frequency of the reference structure; and W is introduced as the admissible field to represent the model predicted response due to unbalanced inertial forces. Equation (5) enables the consideration of acceleration, $\omega^2 W$, as an independent

variable in addition to U. If there is a difference in the mass distribution between the numerical model and physical system, W would be different than measured displacement U leading to a residual error $(U-W)$. The constitutive relation error in Equation (1) and (5) can be combined and the constitutive relation error can be expressed based on the distance between admissible fields as below:

$$\xi^2(U,V,W) = \int_\Omega \frac{\gamma}{2} \mathrm{tr}[(\mathbf{H})(\varepsilon(V)-\varepsilon(U))^*(\varepsilon(V)-\varepsilon(U))] + \frac{1-\gamma}{2}\rho\omega^2(U-W)^*(U-W)\mathrm{d}\Omega \tag{6}$$

where γ is a real positive scalar between zero and one, weighting the relative confidence one places on the modeling of the mass and stiffness distribution of the system. The value of γ is set to 0.5 to provide equal weighting to each error term (Deraemaeker et al. 2002).

3.2.2 ECRE approach solely considering the unbalanced elastic forces

In this section, the reference structure of Section 2.1 is discretized using the finite element (FE) method only considering the effect of the unbalanced elastic forces. For the z^{th} mode, the reliable quantity corresponding to the equilibrium equation of the system is expressed by:

$$\boldsymbol{K}\boldsymbol{v}_z = \lambda_z^e \boldsymbol{M}\boldsymbol{u}_z \tag{7}$$

where $\boldsymbol{K} \in \Re^{N,N}$ is the stiffness matrix of the structure and N is the total number of degrees of freedom (DOFs) in the FE model. $\boldsymbol{u}_z \in \Re^{N,1}$ is the unknown admissible field representing the expanded, experimentally measured mode shape vector; $\boldsymbol{v}_z \in \Re^{N,1}$ is the unknown

admissible field representing the mode shape vector predicted by the numerical model under the inertial forces $\lambda_z^e \boldsymbol{M}\boldsymbol{u}_z$; $\boldsymbol{M} \in \Re^{N,N}$ is the mass matrix of the structure; λ_z^e is the identified eigenvalue.

For the discretization of less reliable equation, one may rewrite the constitutive relation error in Equation (4) using system's stiffness matrix along with numerically predicted and experimentally measured mode shape vectors. For the z^{th} mode shape, the constitutive relation error can then be expressed as:

$$\xi_z^2 = (\boldsymbol{u}_z - \boldsymbol{v}_z)^T \boldsymbol{K} (\boldsymbol{u}_z - \boldsymbol{v}_z) \tag{8}$$

Equation (8) can be interpreted as the implicit residual energy that results from unbalanced elastic forces causing residual displacement within the system.

Regarding the experimental data, the measured mode shapes, $\boldsymbol{u}_z^e$ are often treated as less reliable because the number of measurement locations, *n*, tends to be less than the total DOFs, *N* (Kammer 1991; Chang et al. 2003). $H \in \Re^{n,N}$ is a transformation matrix with zero and one entries, which pairs the expanded mode shape vector $\boldsymbol{u}_z \in \Re^{N,1}$ and the z^{th} measured mode shape $\boldsymbol{u}_z^e \in \Re^{n,1}$. An error term resulting from the expansion process can be expressed as below:

$$e_z^2 = \frac{\alpha}{1-\alpha} (\boldsymbol{H}\boldsymbol{u}_z - \boldsymbol{u}_z^e)^T \boldsymbol{K}_R (\boldsymbol{H}\boldsymbol{u}_z - \boldsymbol{u}_z^e) \tag{9}$$

where $\boldsymbol{K}_R$ is the stiffness matrix condensed to the *n* measured DOFs. Typically, the Guyan reduction method is implemented to condense the stiffness matrix (Guyan 1965). α is a

real positive scalar between zero and one, weighting the relative confidence one places in the experimentally measured mode shapes. If α is chosen to be close to one, the experimental error would be the major contributor to the total residual energy compared to the unbalanced elastic forces. Alternatively, if α is close to zero, the effect of experimental uncertainty is considered to be negligible in the calculation of the total residual energy. The value of α is typically set to 0.5 to assign equal weight to both residual energy caused by unbalanced elastic forces as well as experimental uncertainty in Equation (8) and (9) (Hu et al. 2017).

When calculating the residual energy, the constitutive relation error (Equation (8)) and the expansion error (Equation (9)) must both be considered as they are treated as the less reliable equations. Hence, the residual energy for the z^{th} mode is given by:

$$E_z^2 = (\boldsymbol{u_z} - \boldsymbol{v_z})^T \boldsymbol{K} (\boldsymbol{u_z} - \boldsymbol{v_z}) + \frac{\alpha}{1-\alpha} (\boldsymbol{H u_z} - \boldsymbol{u_z^e})^T \boldsymbol{K_R} (\boldsymbol{H u_z} - \boldsymbol{u_z^e}) \quad (10)$$

The residual energy due to the unbalanced elastic forces, given Equation (10), can be calculated for each structural element. The highest residual energy value indicates the greatest disagreement between the model and the experiments, and thus allowing one to identify the regions that exhibit modeling error.

3.2.3 ECRE approach considering unbalanced elastic and inertial forces

If the effect of the unbalanced inertial forces are also considered, the equilibrium equation of the system (Equation (7)) is no longer satisfied. Instead, for the z^{th} mode, the reliable quantity corresponding to the equilibrium equation of the system is expressed by:

$$\boldsymbol{K}\boldsymbol{v}_z = \lambda_z^e \boldsymbol{M}\boldsymbol{w}_z \tag{11}$$

where $\boldsymbol{w}_z \in \Re^{N,1}$ is the unknown admissible field representing the numerically predicted mode shape vector due to unbalanced inertial forces. Equation (11) can be rewritten in terms of $\boldsymbol{u}_z$, $(\boldsymbol{u}_z - \boldsymbol{v}_z)$ and $(\boldsymbol{u}_z - \boldsymbol{w}_z)$:

$$\boldsymbol{K}(\boldsymbol{u}_z - \boldsymbol{v}_z) = (\boldsymbol{K} - \lambda_z^e \boldsymbol{M})\boldsymbol{u}_z + \lambda_z^e \boldsymbol{M}(\boldsymbol{u}_z - \boldsymbol{w}_z) \tag{12}$$

Integrated with expansion error term in Equation (9), the residual energy for the Equation (6) can be rewritten for the z^{th} experimentally measured mode shape and natural frequency as follows:

$$\begin{aligned} E_z^2 &= \gamma(\boldsymbol{u}_z - \boldsymbol{v}_z)^T \boldsymbol{K}(\boldsymbol{u}_z - \boldsymbol{v}_z) + (1-\gamma)\lambda_z^e(\boldsymbol{u}_z - \boldsymbol{w}_z)^T \boldsymbol{M}(\boldsymbol{u}_z - \boldsymbol{w}_z) \\ &+ \frac{\alpha}{1-\alpha}(\boldsymbol{H}\boldsymbol{u}_z - \boldsymbol{u}_z^e)^T \boldsymbol{K}_R(\boldsymbol{H}\boldsymbol{u}_z - \boldsymbol{u}_z^e) \end{aligned} \tag{13}$$

where $(1-\gamma)\lambda_z^e(\boldsymbol{u}_z - \boldsymbol{w}_z)^T \boldsymbol{M}(\boldsymbol{u}_z - \boldsymbol{w}_z)$ is the residual energy resulting from the unbalanced inertial forces.

The minimization problem thus becomes the minimization of E_z^2 in Equation (13) under the constrain of Equation (11). To solve this problem a Lagrange multiplier, ψ , is introduced. The minimization problem is formulated as shown below:

$$\min g = \gamma \boldsymbol{r_z}^T \boldsymbol{K} \boldsymbol{r_z} + (1-\gamma)\lambda_z^e \boldsymbol{q_z}^T \boldsymbol{M} \boldsymbol{q_z} + \frac{\alpha}{1-\alpha}(\boldsymbol{H}\boldsymbol{u_z} - \boldsymbol{u_z^e})^T \boldsymbol{K_R}(\boldsymbol{H}\boldsymbol{u_z} - \boldsymbol{u_z^e}) + \psi^T(\boldsymbol{K}\boldsymbol{r_z} - \boldsymbol{Z}\left(\lambda_z^e\right)\boldsymbol{u_z} - \lambda_z^e \boldsymbol{M}\boldsymbol{q_z}) \tag{14}$$

where $\boldsymbol{r_z} \equiv (\boldsymbol{u_z} - \boldsymbol{v_z})$ and $\boldsymbol{q_z} \equiv (\boldsymbol{u_z} - \boldsymbol{w_z})$. The minimization in Equation (14) becomes a saddle-point problem, whose solution is defined by the stationary conditions of the function g with respect to the unknown vectors $\boldsymbol{u_z}$, $\boldsymbol{v_z}$, $\boldsymbol{w_z}$ and ψ (Deraemaeker et al. 2002). Through simplification of the stationary conditions, the minimization problem can be rewritten in the matrix form depicted below:

$$\begin{bmatrix} \gamma \boldsymbol{K} & (1-\gamma)\lambda_z^e \boldsymbol{M} & \frac{\alpha}{1-\alpha}\boldsymbol{H}^T \boldsymbol{K_R} \boldsymbol{H} \\ \gamma \boldsymbol{M} & (1-\gamma)\boldsymbol{M} & 0 \\ \boldsymbol{K} & -\lambda_z^e \boldsymbol{M} & -\boldsymbol{Z}(\lambda_z^e) \end{bmatrix} \begin{Bmatrix} \boldsymbol{u_z} - \boldsymbol{v_z} \\ \boldsymbol{u_z} - \boldsymbol{w_z} \\ \boldsymbol{u_z} \end{Bmatrix} = \begin{Bmatrix} \frac{\alpha}{1-\alpha}\boldsymbol{H}^T \boldsymbol{K_R} \boldsymbol{u_z^e} \\ 0 \\ 0 \end{Bmatrix} \tag{15}$$

The second row of the matrix equations corresponds to the relation between the two residual displacement fields, namely $(\boldsymbol{u_z} - \boldsymbol{w_z}) = -\frac{\gamma}{1-\gamma}(\boldsymbol{u_z} - \boldsymbol{v_z})$. Eliminating the vector $(\boldsymbol{u_z} - \boldsymbol{w_z})$ and regrouping yields the following system of equations:

$$\begin{bmatrix} \gamma \boldsymbol{Z}(\lambda_z^e) & \frac{\alpha}{1-\alpha}\boldsymbol{H}^T \boldsymbol{K_R} \boldsymbol{H} \\ \boldsymbol{K} + \frac{\gamma}{1-\gamma}\lambda_z^e \boldsymbol{M} & -\boldsymbol{Z}(\lambda_z^e) \end{bmatrix} \begin{Bmatrix} \boldsymbol{u_z} - \boldsymbol{v_z} \\ \boldsymbol{u_z} \end{Bmatrix} = \begin{Bmatrix} \frac{\alpha}{1-\alpha}\boldsymbol{H}^T \boldsymbol{K_R} \boldsymbol{u_z^e} \\ 0 \end{Bmatrix} \tag{16}$$

After Equation (16) is solved, the elemental residual energy is formulated based on the solution vectors $\boldsymbol{u_z}$, $(\boldsymbol{u_z} - \boldsymbol{v_z})$ and $(\boldsymbol{u_z} - \boldsymbol{w_z})$ from Equation (16). Let $\boldsymbol{K_i}$ and $\boldsymbol{M_i}$ be the sparse $N \times N$ matrices containing the assembled stiffness and mass matrices of the i^{th} element. Then, considering both unbalanced elastic and inertial forces, we obtain the elemental residual energy $E_{z,i}^2$ for the i^{th} element as depicted below:

$$E_{z,i}^2 = (\boldsymbol{u}_z - \boldsymbol{v}_z)^T \boldsymbol{K}_i (\boldsymbol{u}_z - \boldsymbol{v}_z) + \lambda_z^e (\boldsymbol{u}_z - \boldsymbol{v}_z)^T \boldsymbol{M}_i (\boldsymbol{u}_z - \boldsymbol{v}_z) \quad (17)$$

3.2.4 Formulation of elemental residual energy as damage indicator

If experimental measurements of the structure in a damaged state are available and used in Equation (16), the residual displacement field ($\boldsymbol{u}_z - \boldsymbol{v}_z$) accounts for the effect of not only the modeling error in the numerical model, but also the structural damage. Hence, damage detection indicators that simply use Equation (17) are prone to false negatives because the modeling error, if present, can lead to high elemental residual energy (a similar effect as structural damage). Since no model is perfect, it is necessary to take into account for any potential modeling errors in the mass and the stiffness distribution of the system, a correction step is performed before identifying damage. Accordingly, the ECRE equation considering stiffness and mass becomes:

$$ME_{z,i}^2 = \left(\boldsymbol{R}_h - \boldsymbol{R}_d\right)^T \boldsymbol{K}_i (\boldsymbol{R}_h - \boldsymbol{R}_d) + \lambda_z^e (\boldsymbol{R}_h - \boldsymbol{R}_d)^T \boldsymbol{M}_i (\boldsymbol{R}_h - \boldsymbol{R}_d) \quad (18)$$

where $\boldsymbol{R}_d$ is the vector ($\boldsymbol{u}_z - \boldsymbol{v}_z$) obtained from Equation (16) using the experimental measurements from the structure in a damaged state. $\boldsymbol{R}_h$ is the vector ($\boldsymbol{u}_z - \boldsymbol{v}_z$) obtained from Equation (16) using the experimental measurements from the structure in an undamaged state and accounts for the modeling error in both mass and stiffness distribution. $\boldsymbol{R}_h$ is then used to correct the relative displacement field $\boldsymbol{R}_d$, through the subtraction of $(\boldsymbol{R}_h - \boldsymbol{R}_d)$, to account for the imperfections of the reference FE model representing the undamaged structure. However, the elemental residual energy due to the

differences in both stiffness and mass distribution in Equation (18) only provides an absolute measure of modeling error in the i^{th} element. As different modes may have different levels of energy, elemental residual energy itself may be a misleading indicator. Hence, Equation (18) is normalized with respect to a quantity proportional to the total system energy:

$$I_{D,i}^{m} = \sum_{z=1}^{p} \frac{ME_{z,i}^{2}}{\boldsymbol{u}_{z}^{T}\boldsymbol{K}\boldsymbol{u}_{z} + \lambda_{z}^{e}\boldsymbol{u}_{z}^{T}\boldsymbol{M}\boldsymbol{u}_{z}} \tag{19}$$

where $\boldsymbol{I}_{D,i}^{m}$ is the damage indicator for i^{th} element that can be used to identify the damaged regions with reduced effect of modeling error; P is the total number of the experimentally identified modes. The normalization procedure in Equation (19) facilitates the equally weighting of all modes, and thus alleviates the effect of inherent differences in the energy for different modes.

3.3 Case study structure: steel frame

The case study structure is a laboratory-scale, two-story, single bay steel frame made of mild steel with a wooden floor as shown in Figure 2(a). The test frame is built using 2" × 1/8" angle for the four columns that are each 48" in length. The eight beams are each 25-3/8" in length and made of 2" × 1/8" flat stock. `Two 24" × 24" × 1" wooden plates are mounted on the first and second story to mimic diaphragm action with the edges of the plates bolted into the four beams. All beams and columns are connected at the center

using two vertically aligned Grade 5, common threaded bolts spaced 1” apart. The base of each column is connected to a 6” × 6” × 1/2” steel plate using a 2” × 2” × 1/8” steel angle and four ¼” bolts for each column. The steel plate itself is secured to a larger 8’ × 4’ × 1/2” steel plate that serves as a rigid base anchored to concrete floor. All bolts are given an initial torque of 140 in-lb.

The experimental campaign conducted on the steel frame involved an impact hammer vibration test with 64 uniaxial measurement points uniformly distributed along the four columns as shown in Figure 2(b), through which the first four modes of the steel frame are identified. These modal parameters, namely natural frequencies and mode shapes, are used for damage detection.

The FE model of the frame is developed in ANSYS v14.0 using BEAM188 elements for all beam and column elements and SHELL63 elements for the wooden diaphragms (see Figure 2(c)). BEAM188 is a 3D two-node linear element with six DOFs (three translational and three rotational) at each node and considers the relevant quantities of the user-defined cross-section (area, centroid, moments, etc.) as well as member orientation. The SHELL63 element also has six DOFs at each node (three translational and three rotational) with both bending and membrane capabilities. Base connections of the steel frame are modeled as fixed connections by restraining all the translational and rotational DOFs. All beam-column connections, as well as the connections of wood floors

to steel beams, are simplified as rigid connections. A linear elastic constitutive model is adopted as the response of the frame is anticipated to remain in the elastic range. Table 1 lists the material properties of the steel frame FE model.

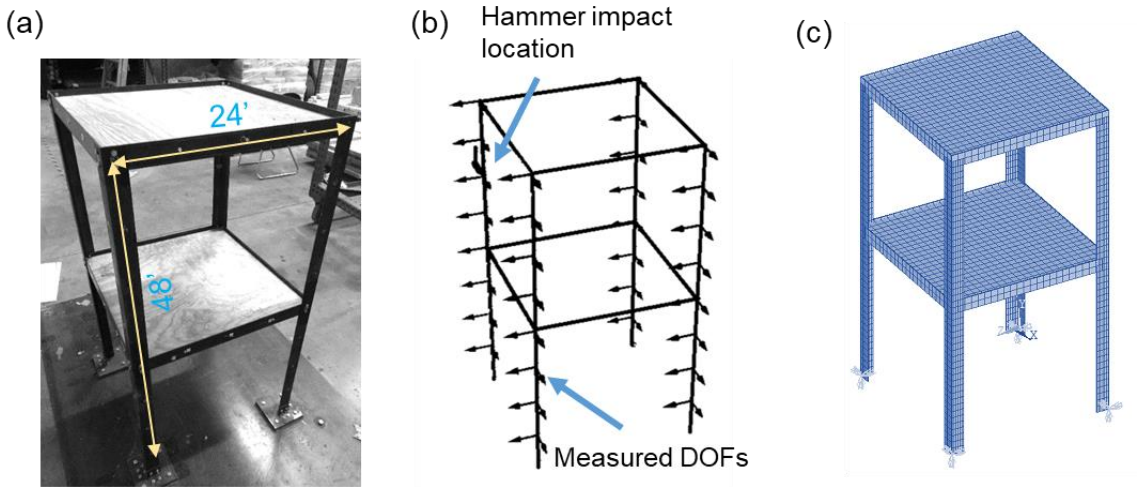

Figure 3.2. (a) Steel frame model with wooden floors; (b) Sensor and hammer impact locations; (c) Extruded view of FE model.

Table 2. Nominal parameter values for the steel frame model

Symbol	Parameter	Value
D_s	Density of steel	0.284 lb/in^3
D_w	Density of wood	0.022 lb/in^3
E_s	Young's modulus of steel	29000000 psi
E_w	Young's modulus of wood	1600000 psi
ν_s	Poisson's ratio of steel	0.33
ν_w	Poisson's ratio of wood	0.35
N_{node}	Number of nodes	1630
N_{dof}	Number of DOF	8604
N_e	Number of beam elements	452
N_m	Number of measured DOFs	64

3.4 Controlled numerical studies on the case study structure

The aim of this section is to evaluate the ECRE-based damage detection methodology without the contaminating effects of model and experimental uncertainty. Hence, we use noise-free *synthetic measurements* (i.e. simulated by the FE model) of first four mode shape vectors of the FE model are obtained at nodes identical to those of the sensor locations on the test structure as shown in Figure 2(b). This upfront pairing of nodes eliminates the need to interpolate the mode shape vectors to make possible compare the model predictions and experimental measurements. In Section 4.1, error localization is conducted on the steel frame in its undamaged state to evaluate the effect of considering inertial forces in ECRE approach. In Section 4.2, using FE model that is built to have the modeling error in mass distribution, three ECRE-based approaches are applied to evaluate the effect of considering inertial forces and the effect of correction process as introduced in Equation (18) on the success of damage detection.

3.4.1 A case study with modeling error in the distribution of mass

To compare the capabilities of ECRE-based error localizations both neglecting and considering the unbalanced inertial forces to identify the mass modeling error without consideration of structural damage. In the former treatment, ECRE error localization is implemented solely considering the unbalanced elastic forces, and neglects the residual energy term due to unbalanced inertial forces (Equation (10)). In the latter treatment, ECRE error localization is implemented considering both the unbalanced elastic and inertial forces (Equation (13)), and thus takes account of any difference in mass distribution. Through the comparison of these two approaches, the importance of considering the unbalanced inertial forces in the ECRE approach can be evaluated.

A modeling error in the mass distribution of the steel frame is intentionally introduced in one of the columns on the frame's first floor as shown in Figure 3(a) by reducing the column's density by 50% (reduction to 0.142 lb/in^3). Synthetic measurements are generated using the FE model with nominal parameter values (recall Table 2) representing the undamaged steel frame.

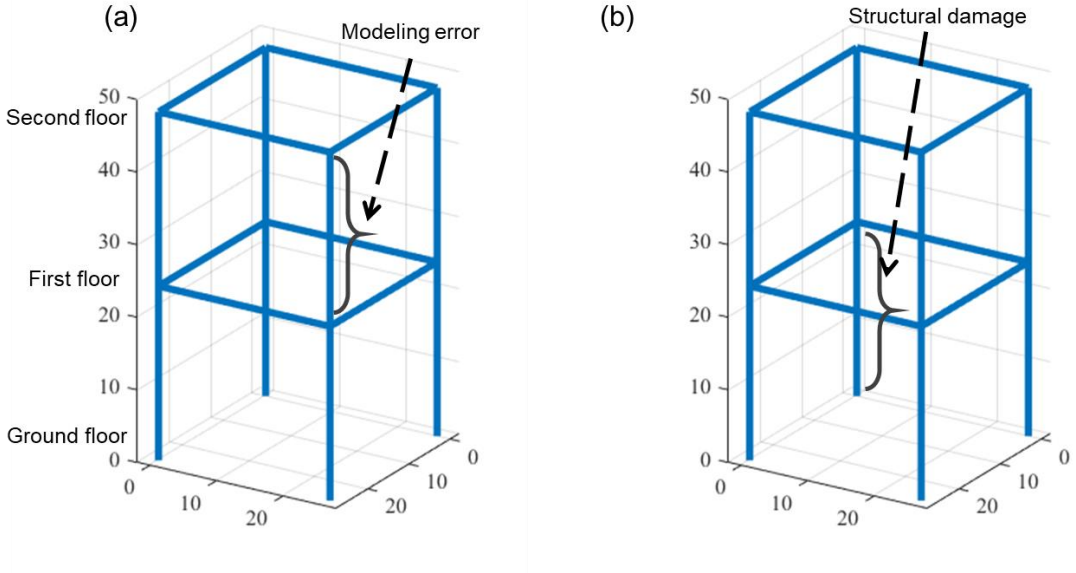

Figure 3.3. The FE model for (a) the undamaged steel frame with error in mass distribution; (b) the damaged steel frame.

In Figure 4(a), through the implementation of K-only ECRE error localization method, the residual energy of the erroneous region is 2.62×10^{-4}. This low value, combined with false negatives with high residual energy of 2.57×10^{-4} near the base connections make it difficult to correctly identify the location of the erroneous modeling parameters. On the other hand, in Figure 4(b), the introduced mass modeling error, calculated using M-K ECRE error localization method, is clearly identified with a residual energy of 3.03×10^{-4} that correctly indicates the erroneous region. Considering the effect of unbalanced inertial forces in the calculation of system's residual energy has improved performance in localizing the erroneous region in scenarios where variation in the mass distribution occurs. When the K-only approach is applied, the unbalanced inertial forces due to the introduced modeling error is taken into account by using unbalanced elastic

forces, which are formulated with the system's stiffness matrix $\boldsymbol{K}$ and residual displacement field ($\boldsymbol{u}_z - \boldsymbol{v}_z$) (Equation (10)). Therefore, it is expected that the calculated high elemental residual energy cannot be effectively pinpoint to those elements with modeling error. Conversely, the M-K approach considers residual energy due to unbalanced inertial forces in addition to unbalanced elastic forces. Because of the utilization of correct formulation (Equation (17)), the calculated high elemental residual energy can be used to localize the introduced modeling error. When ECRE method is applied for damage detection, since the FE model is erroneous, it is important to note that K-only ECRE approach without the consideration of unbalanced inertial forces could lead to false negative damage detection.

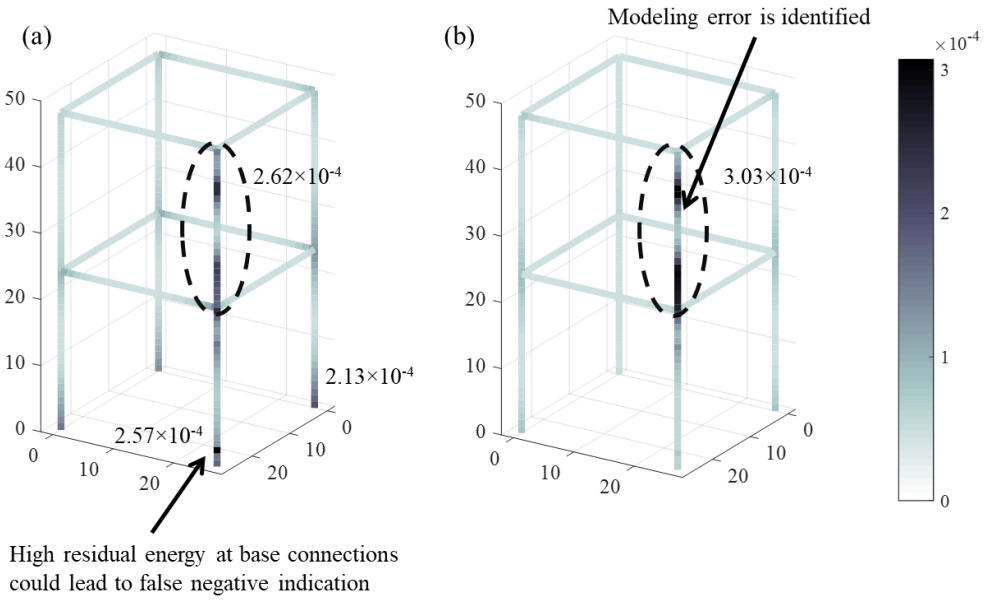

Figure 3.4. Residual energy distribution identified using: (a) K-only ECRE error localization approach; (b) M-K ECRE error localization approach; - - dashed line indicates the modeling error location.

3.4.2 Damage detection using an FE model with mass distribution error

This section aims to test and compare the ability of three different implementations of ECRE-based damage detection to localize damage. Herein, the damage type is considered to change both stiffness and mass properties of the system. The model is considered to be an imperfect representation of the mass distribution.

The first implementation is the M-K ECRE-based damage detection approach that involves considering the unbalanced elastic and inertial forces. The previously discussed model correction approach is adopted. The second implementation includes the M-K ECRE-based damage detection approach without the correction step. The comparison between the first two approaches enables us to evaluate the effect of the correction step on

the calculated indicators for damage detection. The third method applied is the K-only ECRE-based damage approach with the correction step introduced in Section 2. The effect of mass modeling error on the success of the K-only ECRE-based approach is evaluated.

The model for the undamaged structure with introduced modeling error in mass distribution (Figure 3(a)) is used for damage detection. The synthetic measurements for the undamaged structure are generated using the FE model with the nominal parameter values (recall Table 2). The synthetic measurements for the damaged structure, as shown in Figure 3(b), are generated using FE model with the reduction of Young's modulus and density of one column on the ground floor to 50% of their nominal value (Young's modulus is reduced to 2.45×10^7 psi; density is reduced to 0.142 lb/in^3).

Figure 5(a) shows the damage detection results using the K-only ECRE approach with the correction step. Although the correction step is applied to minimize the effect of the intrinsic stiffness modeling error in the reference model, the damaged region is localized with false negatives of 0.86×10^{-3} on other the columns. These false negatives stem from the formulation of residual energy minimization process that neglects mass-related residual energy due to the unbalanced inertial forces. Consequently, the unbalanced inertial forces could lead to high elemental residual energy in the numerical model, which does not necessarily pinpoint the damaged region.

In Figure 5(b), the damage is successfully localized without false negatives using the M-K ECRE-based damage detection approach with the correction step. The highest residual energy of 1.61×10^{-3} correctly pinpoints the simulated damage region. In contrast to K-only ECRE approach, the proposed M-K ECRE approach with the correction step properly includes the mass-related residual energy in Equation (13), allowing the calculation of a more reliable damage indicator I_D^m. Through the comparison of damage detection results in Figure 5(a) and (b), we note that including the effect of unbalanced inertial forces in the ECRE formulation was crucial to the success of ECRE-based damage detection in this case study example as the residual energy term due to unbalanced inertial forces can account for potential mass modeling error.

When M-K ECRE approach without the correction step is applied, Figure 5(c) shows that the damaged region is identified with highest residual energy of 1.60×10^{-3} using. However, false negatives of 1.30×10^{-3} are found on the column with the mass modeling error. Based on the comparison between Figure 5(b) and (c), we note that the correction step of using the corrected relative displacement field vector $(\boldsymbol{R}_h - \boldsymbol{R}_d)$ in Equation (18) can significantly reduce the effect of intrinsic modeling error on the calculated damage indicator and thus reducing the incidents of false negatives that creep in due to modeling errors.

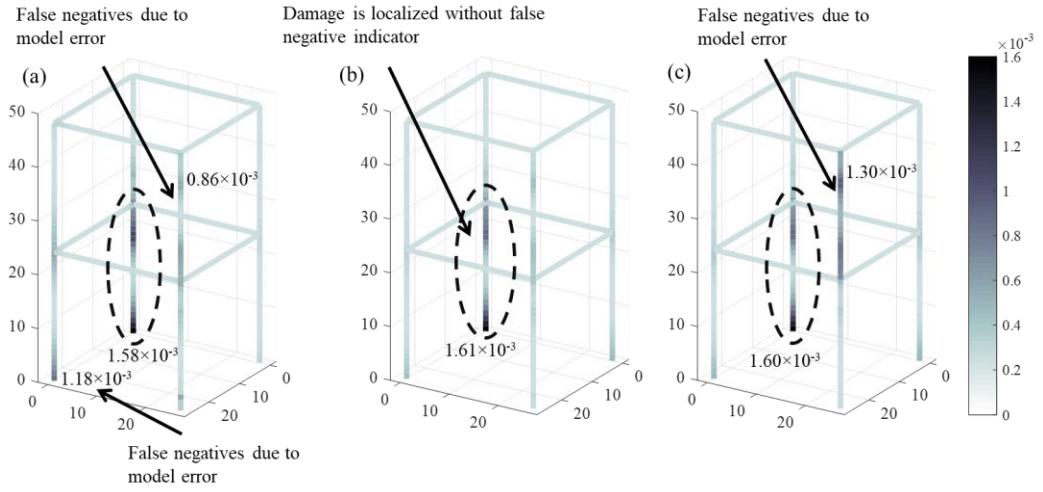

Figure 3.5. ECRE damage detection results when FE model with mass modeling error used as reference model: (a) K-only ECRE-based damage detection approach with the correction step; (b) M-K ECRE-based damage detection approach with the correction step; and (c) M-K ECRE-based damage detection approach without the correction step; - - dashed line indicates the damage location.

3.5 Damage detection on the scaled laboratory steel frame

The proposed approach is also applied to data obtained from laboratory vibration experiments on the steel frame structure in both undamaged and damaged states. The FE model of the steel frame with nominal parameter values (recall Table 2) is applied for damage detection. It is expected that the reference model contains a level of modeling errors in both stiffness and mass distribution due to inevitable simplifications of the geometry and connections, as well as approximate representation of material behavior. For example, the base connections are modeled by constraining all DOFs rather than a semi-rigid connection that may more faithfully represent the actual behavior (Kameshki and Saka 2001). Moreover, the details in mass modeling of the connections (i.e. mass of angles

and bolts) are neglected, which are also likely to lead to a difference between FE model and physical system mass distribution.

Three damage scenarios investigated in this study include the reduction of both the structural stiffness and the mass through the removal of bolts and angles. Damage case 1 is applied to one top connection by the removal of all bolts that connect the column and two beams (Figure 6(a)). Damage case 2 is applied to one base connection by the removal of all bolts with two angle plates attached to the base plate retained (Figure 6(b)). Damage case 3 involves the removal of all bolts and angles at the same damage location as damage case 2 (Figure 6(c)). For detecting damage in these scenarios, we implement ECRE-based damage detection approach, with and without consideration of the effect of unbalanced inertial forces.

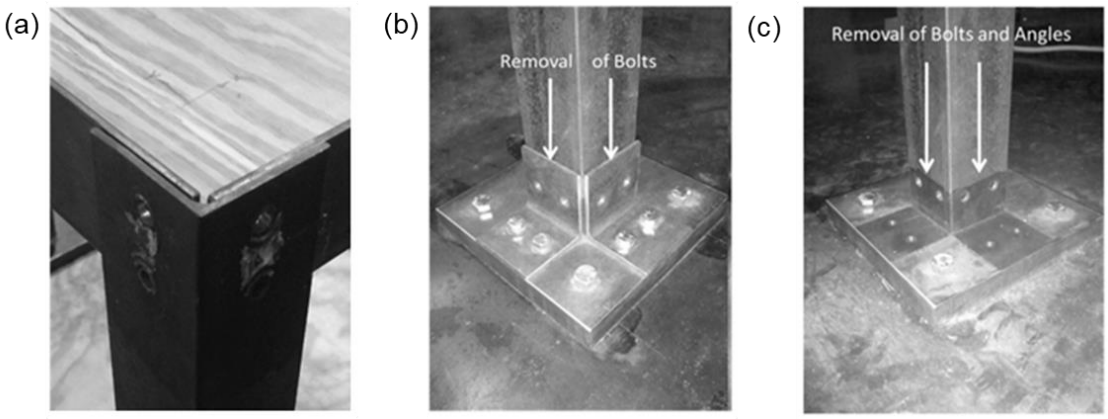

Figure 3.6. Three damage cases with controlled damage introduced: (a) the removal of all bolts at one top connection; (b) the removal of all bolts at one base connection; (c) the removal of all bolts and angles at one base connection.

3.5.1 Damage case 1: removal of bolts from the connection of top floor

The aim of this damage case is to test the performance of the ECRE-based damage detection method on identifying damage in the superstructure of the frame. Using the K-only ECRE-based damage detection approach as shown in Figure 7(a), the maximum indicator of 0.05 pinpoints damaged region. However, two obvious false negative indications (0.03) appear on the second floor; and false negative indications with damage indicators (approximately 0.02) are located at the connections of the ground and first floor. Conversely, using the M-K ECRE-based damage detection approach as shown in Figure 7(b), the damaged region is more effectively localized with the maximum damage indicator of 0.3. One false negative indication with a lower value of 0.25 is found at the diagonal neighbor of the true damaged connection, while another false negative indication with lower value of 0.15 is observed at the connection on the first floor. Consequently, although it is observed that there are still two false negatives using M-K ECRE-based approach, the M-K ECRE-based damage detection result has shown superiority to the K-only approach, while providing more reliable damage detection results with fewer false negatives.

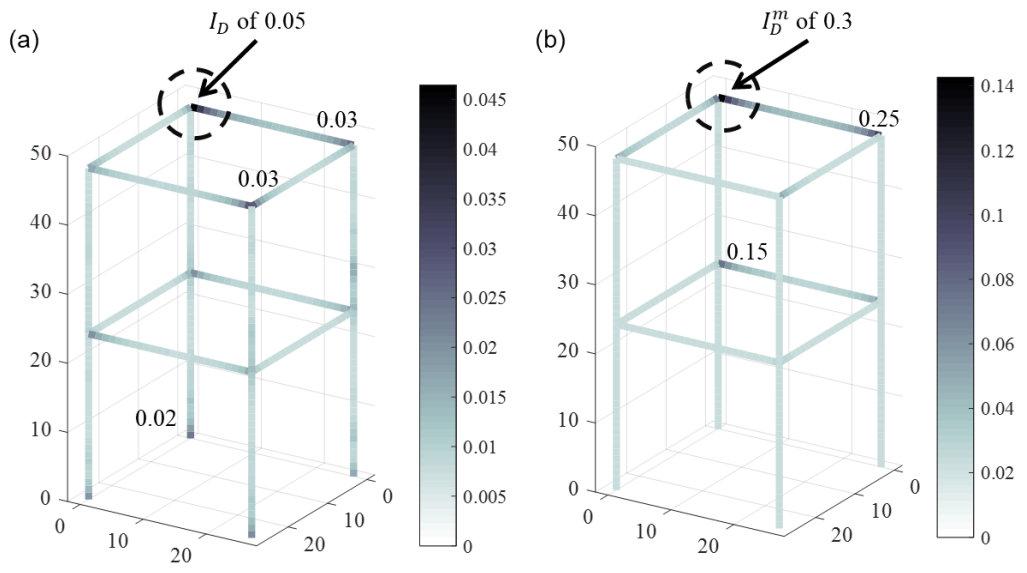

Figure 3.7. ECRE damage detection result of damage case 1 with the consideration of residual energy due to: (a) only unbalanced elastic forces, and (b) both unbalanced elastic and inertial forces; - - dashed line indicates the actual damage location.

3.5.2 Damage case 2: removal of bolts from the base of one column

For the K-only ECRE-based approach, Figure 8(a) shows that the maximum damage indicator of 0.07 is located at the damaged base connection. However, false negative indications with lower values (around 0.05) are also visible around the connections of the second floor. For the M-K ECRE-based approach, Figure 8(b) shows the damaged region is successfully identified with the maximum damage indicator of 0.35. Only one false negative indication with a lower value of 0.2 is observed in Figure 8(b). It is observed that the maximum damage indicator value calculated considering both the unbalanced elastic and inertial forces (approximately 0.35) is higher than that obtained only considering the unbalanced elastic forces (approximately 0.07). Moreover, the comparison

of these two damage detection results in Figure 8 shows that the false negative indication on the top of the frame is eliminated when both the unbalanced elastic and inertial forces are considered for damage detection. The importance of including residual energy term due to the unbalanced inertial forces in the ECRE formulation is once again emphasized so that the damage detection method can be more robust to potential mass modeling error.

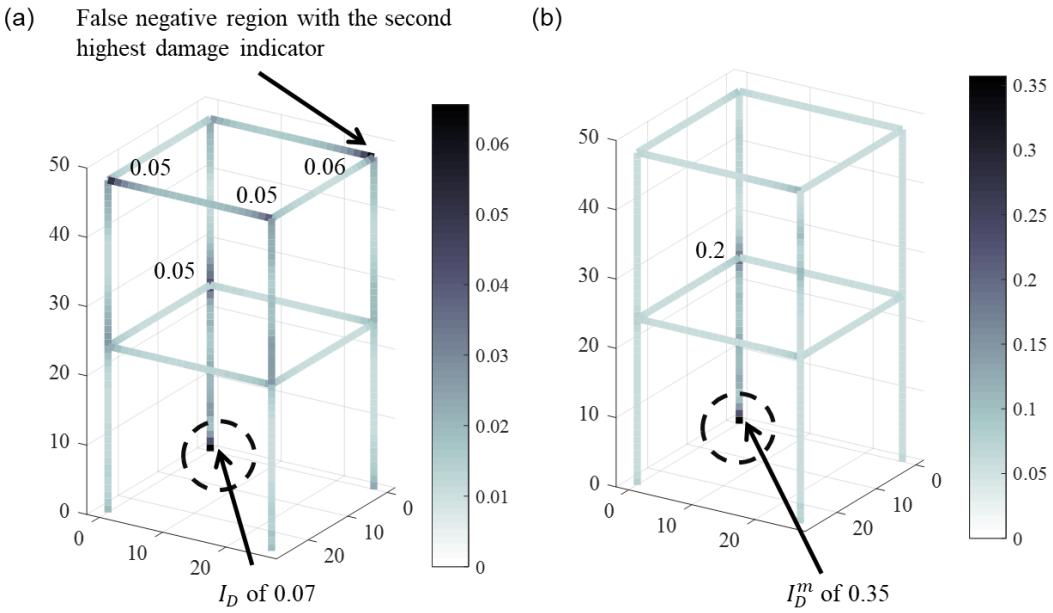

Figure 3.8. ECRE result of damage case 2 with the consideration of residual energy due to: (a) only unbalanced elastic forces, and (b) both unbalanced elastic and inertial forces; - - dashed line indicates the actual damage location.

3.5.3 Damage case 3: removal of bolts and angles from the base of one column

Compared to damage case 2, damage case 3 involves the removal of the angle plates in addition to the bolts. Therefore, damage case 3 is more severe because the associated column is no longer constrained by the friction between these angle plates and the column at the connection. In Figure 9 below, we observe that the damage indicators correctly

identify the location of damage in both M-K and K-only ECRE-based approaches, but with a different max damage indicator value (0.35 with M-K ECRE-based approach compared to 0.25 with K-only ECRE-based approach). The distribution of the damage indicators calculated using K-only ECRE-based approach in Figure 9(a) is similar to the M-K ECRE-based damage detection results in Figure 9(b). Both approaches are shown to successfully identify the location of damage and this result is attributed to the high severity of the damage case. Thus, if the damage introduced is severe enough, it will be detected even without consideration of the residual energy due to unbalanced inertial forces in the ECRE-based damage detection method.

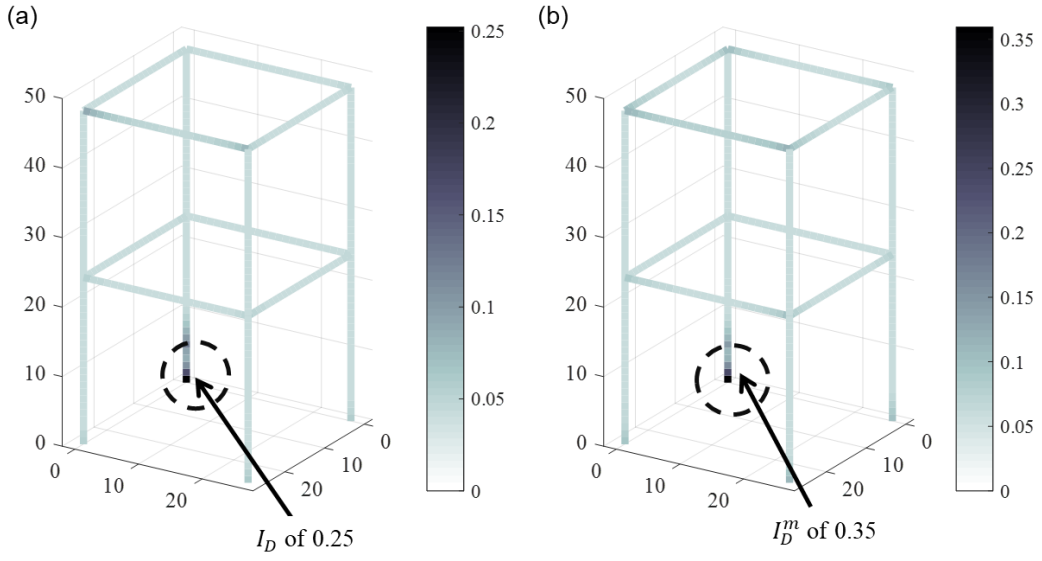

Figure 3.9. ECRE result of damage case 3 with the consideration of residual energy due to: (a) only unbalanced elastic forces, and (b) both unbalanced elastic and inertial forces; - - dashed line indicates the actual damage location.

3.6 Conclusion

Most of model based damage detection methods have been conducted focusing solely on the change within the stiffness matrix to detect damage and neglecting the influence of damage on structural mass as well as the potential modeling error in the FE model mass distribution. For example, in K-only ECRE-based approach, the damage indicator was formulated based on the minimization of residual energy considering only unbalanced elastic forces due to the variation in the stiffness distribution. The conclusions are as follows:

1. In this paper, the M-K ECRE-based methodology is proposed by additionally considering the effect of the unbalanced inertial forces between numerical

model and physical model. Therefore, the proposed approach allows for the consideration of variations in both system's mass and stiffness.

2. The ability of the proposed M-K ECRE approach for the error localization is verified through a numerical study of a steel frame in an undamaged state with introduced mass modeling error. Compared to the K-only ECRE approach, the M-K ECRE approach can achieve an improved performance in localizing the erroneous region.
3. The M-K ECRE-based damage detection method is advantageous as the proposed correction procedure can account for the effect of potential modeling errors, which is inevitable in numerical models. Another numerical study on the capability of ECRE-based approach for damage detection is conducted with an imperfect FE model with mass modeling error. Numerical results indicate that the proposed approach can effectively identify the structural damage with little influence of modeling error.
4. The M-K ECRE-based approach is a more robust damage detection scheme which is suitable for damage patterns that alter not only the stiffness, but also the mass of the system. The M-K ECRE-based damage detection approach is illustrated using a steel frame model that is tested in the laboratory considering three different damage scenarios. The comparison of results of K-only and M-

K ECRE-based damage detection reveal that the latter approach can provide a significant improvement to the damage detection accuracy with higher damage indicators and fewer false negatives.

Reference

Agbabian, M. S., Masri, S. F., Miller, R. K., & Caughey, T. K. (1991). System identification approach to detection of structural changes. *Journal of Engineering Mechanics*, *117*(2), 370-390.

Atamturktur, H. S., Gilligan, C. R., & Salyards, K. A. (2013). Detection of internal defects in concrete members using global vibration characteristics. *ACI Materials Journal*, *110*(5), 1-10.

Berman, A. (1979). Mass matrix correction using an incomplete set of measured modes. *AIAA journal*, *17*(10), 1147-1148.

Brownjohn, J. M., Xia, P. Q., Hao, H., & Xia, Y. (2001). Civil structure condition assessment by FE model updating: methodology and case studies. *Finite Elements in Analysis and Design*, *37*(10), 761-775.

Cawley, P., & Adams, R. D. (1979). The location of defects in structures from measurements of natural frequencies. *The Journal of Strain Analysis for Engineering Design*, *14*(2), 49-57.

Charbonnel, P. E., Ladevèze, P., Louf, F., & Le Noac'h, C. (2013). A robust CRE-based approach for model updating using in situ measurements. *Computers & Structures*, *129*, 63-73.

Deraemaeker, A., Ladevèze, P., & Leconte, P. (2002). Reduced bases for model updating in structural dynamics based on constitutive relation error. *Computer methods in applied mechanics and engineering*, *191*(21), 2427-2444.

Doebling, S. W., Farrar, C. R., & Prime, M. B. (1998). A summary review of vibration-based damage identification methods. *Shock and Vibration Digest*, *30*(2), 91-105.

El Maaddawy, T., Soudki, K., & Topper, T. (2005). Long-term performance of corrosion-damaged reinforced concrete beams. *ACI Structural Journal*, *102*(5), 649.

Faverjon, B., & Sinou, J. J. (2009). Identification of an open crack in a beam using an *a posteriori* error estimator of the frequency response functions with noisy measurements. *European journal of mechanics-A/Solids*, *28*(1), 75-85.

Friswell, M. I. (2007). Damage identification using inverse methods. *Philosophical Transactions of the Royal Society of London A: Mathematical, Physical and Engineering Sciences*, *365*(1851), 393-410.

Fritzen, C. P., Jennewein, D., & Kiefer, T. (1998). Damage detection based on model updating methods. *Mechanical systems and signal processing*, *12*(1), 163-186.

Fugate, M. L., Sohn, H., & Farrar, C. R. (2001). Vibration-based damage detection using statistical process control. *Mechanical Systems and Signal Processing*, *15*(4), 707-721.

Guyan, R. J. (1965). Reduction of stiffness and mass matrices. *AIAA journal*, *3*(2), 380.

Hassiotis, S., & Jeong, G. D. (1995). Identification of stiffness reductions using natural frequencies. *Journal of Engineering Mechanics*, *121*(10), 1106-1113.

He, W. Y., & Zhu, S. (2013). Progressive damage detection based on multi-scale wavelet finite element model: numerical study. *Computers & Structures*, *125*, 177-186.

Hearn, G., & Testa, R. B. (1991). Modal analysis for damage detection in structures. *Journal of Structural Engineering*, *117*(10), 3042-3063.

Hemez, F. M., & Farhat, C. (1995). Bypassing numerical difficulties associated with updating simultaneously mass and stiffness matrices. *AIAA journal*, *33*(3), 539-546.

Hu, X., Prabhu, S., Atamturktur, S., & Cogan, S. (2017). Mechanistically-informed damage detection using dynamic measurements: Extended constitutive relation error. *Mechanical Systems and Signal Processing*, *85*, 312-328.

Joukoski, A., Portella, K. F., Galvão, J. C. A., Alberti, E. L., Soares, M. A., & Tümmler, P. (2009). Mass loss evaluation of a roller-compacted concrete dam: Understanding the problem for planning repair intervention. *Concrete Solutions*, 283.

Kameshki, E. S., & Saka, M. P. (2001). Optimum design of nonlinear steel frames with semi-rigid connections using a genetic algorithm. *Computers & Structures*, *79*(17), 1593-1604.

Kim, H. M., & Bartkowicz, T. J. (1993). Damage detection and health monitoring of large space structures. *Sound and vibration*, *27*, 12-17.

Kopsaftopoulos, F. P., & Fassois, S. D. (2010). Vibration based health monitoring for a lightweight truss structure: experimental assessment of several statistical time series methods. *Mechanical Systems and Signal Processing*, *24*(7), 1977-1997.

Kosmatka, J. B., & Ricles, J. M. (1999). Damage detection in structures by modal vibration characterization. *Journal of Structural Engineering*, *125*(12), 1384-1392.

Ladeveze, P., & Chouaki, A. (1999). Application of a posteriori error estimation for structural model updating. *Inverse Problems*, *15*(1), 49.

Landolfo, R., Cascini, L., & Portioli, F. (2010). Modeling of metal structure corrosion damage: a state of the art report. *Sustainability*, *2*(7), 2163-2175.

Lee, J. J., Lee, J. W., Yi, J. H., Yun, C. B., & Jung, H. Y. (2005). Neural networks-based damage detection for bridges considering errors in baseline finite element models. *Journal of Sound and Vibration*, *280*(3), 555-578.

Ma, J., & Pines, D. J. (2003). Damage detection in a building structure model under seismic excitation using dereverberated wave mechanics. *Engineering Structures*, *25*(3), 385-396.

Martin, M. T., & Doyle, J. F. (1996). Impact force identification from wave propagation responses. *International Journal of Impact Engineering*, *18*(1), 65-77.

Mottershead, J. E., Link, M., & Friswell, M. I. (2011). The sensitivity method in finite element model updating: a tutorial. *Mechanical Systems and Signal Processing*, *25*(7), 2275-2296.

Oberkampf, W. L., DeLand, S. M., Rutherford, B. M., Diegert, K. V., & Alvin, K. F. (2002). Error and uncertainty in modeling and simulation. *Reliability Engineering & System Safety*, *75*(3), 333-357.

Prabhu, S., & Atamturktur, S. (2012). Feature assimilation for vibration based damage detection. *Journal of Testing and Evaluation*, *41*(1), 39-49.

Prabhu, S., & Atamturktur, S. (2015). A review on prognostic evaluation of historic masonry structures: Present Challenges and Future Direction. *The Masonry Society Journal*, *33*(1), 1-12.

Prabhu, S., Atamturktur, S., Brosnan, D., Messier, P., & Dorrance, R. (2014). Foundation settlement analysis of Fort Sumter National Monument: Model development and predictive assessment. *Engineering Structures*, *65*, 1-12.

Sheinman, I. (1996). Damage detection and updating of stiffness and mass matrices using mode data. *Computers & Structures*, *59*(1), 149-156.

Shi, Z., Law, S. S., & Zhang, L. (2000). Structural damage detection from modal strain energy change. *Journal of Engineering Mechanics*, *126*(12), 1216-1223.

Teughels, A., & De Roeck, G. (2004). Structural damage identification of the highway bridge Z24 by FE model updating. *Journal of Sound and Vibration*, *278*(3), 589-610.

Teughels, A., & De Roeck, G. (2004). Structural damage identification of the highway bridge Z24 by FE model updating. *Journal of Sound and Vibration*, *278*(3), 589-610.

Whalen, T. M., Archer, G. C., & Bhatia, K. M. (2004). Implications of vertical mass modeling errors on 2D dynamic structural analysis. *The Structural Design of Tall and Special Buildings*, *13*(4), 305-314.

Whittome, T. R., & Dodds, C. J. (1983). 9 Monitoring offshore structures by vibration techniques. In *Design in Offshore Structures*, 93-100. Thomas Telford Publishing.

Worden, K., Manson, G., & Denoeux, T. (2009). An evidence-based approach to damage location on an aircraft structure. *Mechanical Systems and Signal Processing*, *23*(6), 1792-1804.

Yuen, K. V., Au, S. K., & Beck, J. L. (2004). Two-stage structural health monitoring approach for phase I benchmark studies. *Journal of Engineering Mechanics*, *130*(1), 16-33.

Zimmerman, D. C., & Kaouk, M. (1994). Structural damage detection using a minimum rank update theory. *Transactions-American Society of Mechanical Engineers Journal of Vibration and Acoustics*, *116*, 222-222.

Zou, Y., Tong, L. P. S. G., & Steven, G. P. (2000). Vibration-based model-dependent damage (delamination) identification and health monitoring for composite structures—a review. *Journal of Sound and vibration*, *230*(2), 357-378.

Kammer, D. C. (1991). Sensor placement for on-orbit modal identification and correlation of large space structures. *Journal of Guidance, Control, and Dynamics*, *14*(2), 251-259.

Chang, P. C., Flatau, A., & Liu, S. C. (2003). Health monitoring of civil infrastructure. *Structural health monitoring*, *2*(3), 257-267.

CHAPTER FOUR

MODEL CALIBRATION OF LOCALLY NONLINEAR DYNAMICAL SYSTEMS: EXTENDED CONSTITUTIVE RELATION ERROR WITH MULTI-HARMONIC COEFFICIENTS

4.1 Introduction

Local nonlinearities are pervasive in engineering applications (Shi and Atluri 1992; Fey et al. 1996; Wojtkiewicz and Johnson. 2011). In some cases, local nonlinearities are deliberately designed into the system to avoid excessively high responses or stresses (Fey 1992) and in others, they arise from large deformations or material stress (Clough and Wilson 1979). Examples include nonlinear bearings (Nelson and Nataraj 1989), dry friction damping (Ferri and Dowell 1988), local nonlinear springs and dampers (Qu 2002), structural joints with an opening and closing ability (Niwa and Clough 1982), and concrete cracking (Atamturktur et al. 2013; Llau et al. 2015).

In these systems, as the nonlinear effects are localized within a component of a larger linear system, the dynamic response tends to remain predominantly linear for small magnitude forces (Clough and Wilson 1979). However, when sufficiently high magnitude forces are applied, the dynamic behavior becomes nonlinear and is governed by the interaction between the linear and nonlinear components. Hence, when developing numerical models to represent such systems, one must pay attention to accurate modeling

of both the global system that exhibits the underlying linear behavior and the spatially local component that introduces nonlinearity. It is important to note that modeling error in the underlying linear behavior could degrade the prediction accuracy of the overall nonlinear behavior, resulting in large deviations from the measured dynamic response (Lenaerts et al. 2001; Kerschen et al. 2003; Kerschen et al. 2005; Hot 2012). As such, the accuracy with which model error in local, nonlinear components can be identified is naturally dependent on errors which may be associated with linear components.

Common approaches for calibrating models of nonlinear dynamical systems can be grouped into two categories. The first category of approaches corrects errors in the representation of both the linear and nonlinear responses of the system simultaneously (Lenaerts et al. 2001; Meyer and Link 2003; Bellizzi and Defilippi 2003; Kerschen et al. 2005). These approaches may face the identifiability problem due to the large number of confounding parameters that need to be calibrated using an inevitably finite set of available measurements (Lenaerts et al. 2001; Kurt et al. 2005; Jaishi and Ren 2007; Van Buren and Atamturktur 2012). The second category of approaches, on the other hand, corrects the representation of only the nonlinear response, and therefore assumes the linear system to be modeled accurately. This assumption in turn mandates the availability of reliable *a priori* knowledge of the linear system (Kerschen et al. 2005; Isasa et al. 2011). Hence, this second approach risks that during calibration of the locally nonlinear component

parameters errors in the linear system may be compensated for since the linear model accuracy is seldom guaranteed. Separately identifying the modeling errors that govern the system's linear and nonlinear behavior offers a solution that can mitigate the issues related to identifiability faced by both of these categories of approaches (Lenaerts et al. 2001; Ewins et al. 2015).

In this paper, a two-step process is presented for calibrating numerical models of dynamical systems with local nonlinearities. The process involves separately measuring the system's predominantly linear and nonlinear dynamic response under periodic excitation at low and high force magnitudes, respectively. From these response measurements, multi-harmonic coefficients, a commonly used set of features for characterization of nonlinear dynamical systems (Cardona et al. 1994), are extracted. When coupled with the extended constitutive relation error (ECRE), the multi-harmonic coefficients allow the calculation of the residual energy, which reflects the discrepancy between the model predictions and the experimental measurements (Isasa et al. 2011; Hu et al. 2017). In the first step of this study, the residual energy in the predominantly linear behavior is calculated for each discretized finite element allowing us to identify the model input parameters that need calibration. These input parameters, when combined with the poorly known parameters associated with the local nonlinearity constitute the total set of calibration parameters.

Subsequently in the second step, the residual energy calculated under both the low magnitude excitation and the nonlinearity-inducing, higher magnitude excitation is minimized to update the calibration parameters. Thus, model parameter calibration becomes an optimization problem that is solved through an iterative approach combining the multi-harmonic balance method (MHB) and ECRE into a method henceforth referred to as Iterative Integrated MHB and ECRE (IIME). In this study, the performance and efficiency of IIME are compared against discrete, sampling-based optimal value searches that are commonly used for nonlinear model calibration.

This paper is organized as follows. In Section 2, we briefly review the MHB-ECRE identification approach as applied to nonlinear dynamical systems. Section 3 describes the procedure for the two-step model calibration approach. In Section 4, the calibration approach is demonstrated on the finite element model of an academic example: a nonlinear beam with model error in both the linear and nonlinear components, using synthetically generated measurements. In this section, the efficacy of the proposed two-step approach is evaluated by comparing the obtained results against those of a one-step MHB-ECRE nonlinear model calibration. In Section 5, the limitations of the proposed approach when implemented with reduced quantity (i.e. fewer measured degrees of freedom) and quality (i.e. higher noise levels) of measurements is discussed. Moreover, the effect of the location of the excitation force and model error on the performance of the proposed method is

evaluated. Finally, Section 6 draws the conclusions of this paper and summarizes the benefits and drawback of the proposed nonlinear model calibration method compared to the conventional, single-step MHB-ECRE method.

4.2 Background perspectives: nonlinear model calibration using the MHB-ECRE approach

When calibrating numerical models of dynamical systems, the discrepancy between model predictions and experimental measurements can be calculated using response features in modal, time, or frequency domains (Atamturktur et al. 2012). In modal domain, nonlinear effects are projected into modal space in terms of nonlinear normal modes. Nonlinear normal modes are amplitude-dependent, however, which prevents the direct separation of space and time in the governing equations of motion (Vakakis 1997; Kerschen et al. 2009). This energy dependence complicates the analytical calculation of the nonlinear normal modes, and the model calibration using nonlinear normal models often becomes computationally demanding (Kerschen et al. 2006). The use of time domain response features is less computationally demanding than modal domain features as measurement devices directly provide the desired inputs (Masri and Caughey 1979; Gondhalekar et al. 2009). Nonetheless, time domain response features are large-dimensional and highly sensitive to measurement noise (Atamturktur and Laman 2012;

Moaveni and Asgarieh 2012), which makes direct comparisons between the measurements and the model predictions in the time domain highly unreliable.

Frequency domain response features are calculated by applying a transformation process on the time domain signals to separate the response into a series of harmonics (Meyer and Link 2003; Böswald and Link 2004). In frequency domain methods, the time and space in the governing equations of motion can be easily separated through linearization using Fourier series expansion. Thus, response features in frequency domain can be expressed as a function of excitation frequency and amplitude (Ferreira and Serpa 2005). Furthermore, frequency domain features are less sensitive to noise and more compact compared to the time domain features (Kerschen et al. 2006; Atamturktur and Laman 2012). In this paper, we implement a class of frequency domain response features known as multi-harmonic coefficients calculated through the Multi-Harmonic Balance (MHB) method, chosen for their high accuracy (Ren et al. 1998) and computational efficiency (Huang et al. 2006).

4.2.1 Multi-harmonic balance method

The equation of motion of a nonlinear structure with local geometrical nonlinearity can be written as follows:

$$\boldsymbol{M}\ddot{\boldsymbol{x}}(t) + \boldsymbol{C}\dot{\boldsymbol{x}}(t) + \boldsymbol{K}\boldsymbol{x}(t) + K_{NL}\boldsymbol{x}^3(t) = \boldsymbol{p}(t) \quad (1)$$

where $\boldsymbol{M}, \boldsymbol{C}, \boldsymbol{K} \in \Re^{N,N}$ are the mass, damping and stiffness matrices, respectively, and N is the number of degrees of freedom (DOF) considered. The stiffness matrix is assumed to be positive definite. Here, $\boldsymbol{p}(t)$ is the external force vector and $\boldsymbol{x}(t)$ is the displacement response vector of the N DOFs at time t. In Equation (1), a spatially localized, geometrical nonlinearity is represented by the cubic stiffness, K_{NL} (Worden and Tomlinson 2000).

In linear structural dynamics, the system is conveniently characterized by the structural modes and their associated resonant frequencies. In nonlinear dynamical systems, however, distinctly nonlinear features can be generated from a set of periodic response vectors. When a periodic excitation is applied to a nonlinear dynamical system, the input energy is concentrated at the excitation frequency making it relatively simple to generate nonlinear features through the transformation from time domain response into frequency domain response. This approach also yields higher signal-to-noise ratio compared to the response measured under random or transient excitations (Worden and Tomlinson 2000). Because of these benefits, solving the equation of motion of a nonlinear system under periodic excitation has become common practice for evaluating the dynamic behavior of nonlinear systems (Kerschen et al. 2006).

Most early approaches for predicting the steady-state oscillation of a nonlinear system under periodic excitation were limited to approximate calculations of the

fundamental harmonic coefficients. These fundamental harmonic coefficients were assumed to have a significantly larger value compared to higher order harmonic coefficients (Stoker 1950; Tondl 1974). However, in the early 1980s, researchers began to recognize that the higher order harmonic coefficients are also essential to accurately predict the steady state response (Tamura et al. 1981; Leung and Fung 1989). To include the higher order harmonics for steady-state oscillations of a nonlinear system, Tamura et al. (1981) suggested the multi-harmonic balance (MHB) method. As an extension of the fundamental harmonic balance approach, MHB operates in the frequency domain to solve nonlinear equations of motion under periodic excitation using a Fourier series approximation. MHB has proven capability solving the periodic response of nonlinear systems more efficiently than time domain integration methods, such as Newmark's, central difference, and Runge-Kutta methods (Cardona et al. 1994).

In MHB, the periodic displacement response vector of a nonlinear system is expressed as a Fourier series:

$$\boldsymbol{x}(t) = \boldsymbol{Q}_0 + \sum_{j=1}^{n} (\boldsymbol{Q}_j^c \cos m_j \omega t + \boldsymbol{Q}_j^s \sin m_j \omega t) \tag{2}$$

where $\boldsymbol{Q}_0$ is a constant; $\boldsymbol{Q}_j^c$ and $\boldsymbol{Q}_j^s$ represent the j^{th} cosine and sine multi-harmonic coefficients, respectively; m_j is the harmonic of excitation frequency ω; and n is the number of harmonics included in the analysis. Usually, the multi-harmonic coefficients are obtained by directly applying a fast Fourier transform on the time history response of

measured DOFs. If excitation frequency is constant, Fourier series and harmonic curve fitting tools can also be applied for calculating the multi-harmonic coefficients (Isasa et al. 2011).

Introducing Equation (2) into the equation of motion for the nonlinear system given in Equation (1) results in the following expression:

$$\begin{aligned}&\boldsymbol{M}\left(\sum_{j=1}^{n}\left(-(m_j\omega)^2\boldsymbol{Q}_j^c\cos m_j\omega t-(m_j\omega)^2\boldsymbol{Q}_j^s\sin m_j\omega t\right)\right)\\&+\boldsymbol{C}\left(\sum_{j=1}^{n}\left(-m_j\omega\boldsymbol{Q}_j^c\sin m_j\omega t+m_j\omega\boldsymbol{Q}_j^s\cos m_j\omega t\right)\right)\\&+\boldsymbol{K}\left(\boldsymbol{Q}_0+\sum_{j=1}^{n}\left(\boldsymbol{Q}_j^c\cos m_j\omega t+\boldsymbol{Q}_j^s\sin m_j\omega t\right)\right)+K_{NL}\boldsymbol{x}^3(t)=\boldsymbol{p}(t)\end{aligned} \tag{3}$$

Sequentially pre-multiplying all terms in Equation (3) by the harmonic functions $(1,\cos m_1\omega t,\sin m_1\omega t\ldots\cos m_n\omega t,\sin m_n\omega t)$ and integrating from zero to the fundamental period of the system, $T=2\pi/\omega$, the following frequency domain expression can be obtained:

$$\boldsymbol{\mathcal{Z}}(\omega)\boldsymbol{Q}_\omega+\boldsymbol{F}(\boldsymbol{Q}_\omega,\omega)-\boldsymbol{P}=0 \tag{4}$$

where $\boldsymbol{Q}_\omega=\{Q_0,Q_1,\ldots,Q_{2n}\}$ is the vector of harmonic coefficients with $Q_i\in\Re^{N,1}$. The matrix $\boldsymbol{\mathcal{Z}}(\omega)\in\Re^{(2n+1)N,(2n+1)N}$ is a matrix of structural system properties in the frequency domain and is expressed as:

$$\boldsymbol{\mathcal{Z}}(\omega)=\begin{bmatrix}\boldsymbol{K}&0&0&\ldots&0&0\\0&\boldsymbol{K}-(m_1\omega)^2\boldsymbol{M}&m_1\omega\boldsymbol{C}&\ldots&0&0\\0&-m_1\omega\boldsymbol{C}&\boldsymbol{K}-(m_1\omega)^2\boldsymbol{M}&\ldots&0&0\\\ldots&\ldots&\ldots&\ldots&\ldots&\ldots\\0&0&0&\ldots&\boldsymbol{K}-(m_n\omega)^2\boldsymbol{M}&m_n\omega\boldsymbol{C}\\0&0&0&\ldots&-m_n\omega\boldsymbol{C}&\boldsymbol{K}-(m_n\omega)^2\boldsymbol{M}\end{bmatrix} \tag{5}$$

The nonlinear force vector $K_{NL}\boldsymbol{x}^3(t)$ and periodic excitation force vector $\boldsymbol{p}(t)$ in Equation (3) are also transformed from nonlinear, time domain response into linearized, frequency domain response (see Equations (6) and (7)). It is seen that each harmonic of the periodic excitation yields corresponding sine and cosine functions not only for the excitation, $\boldsymbol{P}$, but also for the force due to the localized nonlinearity, $\boldsymbol{F}(\boldsymbol{Q}_\omega, \omega)$.

Nonlinear force vectors in frequency domain $\boldsymbol{F}(\boldsymbol{Q}_\omega, \omega) \in \Re^{(2n+1)N,1}$ are then expressed as:

$$\boldsymbol{F}(\boldsymbol{Q}_\omega, \omega) = \begin{Bmatrix} \int_0^T f_{NL}(\boldsymbol{x}(t))dt \\ \frac{\omega}{\pi}\int_0^T f_{NL}(\boldsymbol{x}(t))m_1 \cos\omega t dt \\ \frac{\omega}{\pi}\int_0^T f_{NL}(\boldsymbol{x}(t))m_1 \sin\omega t dt \\ \vdots \\ \frac{\omega}{\pi}\int_0^T f_{NL}(\boldsymbol{x}(t))\cos m_n\omega t dt \\ \frac{\omega}{\pi}\int_0^T f_{NL}(\boldsymbol{x}(t))\sin m_n\omega t dt \end{Bmatrix} \quad \text{where } f_{NL}(\boldsymbol{x}(t)) = K_{NL}\boldsymbol{x}^3(t) \tag{6}$$

Periodic excitation force vectors in frequency domain $\boldsymbol{P} \in \Re^{(2n+1)N,1}$ are expressed as:

$$\boldsymbol{P} = \begin{Bmatrix} \int_0^T \boldsymbol{p}(t)dt \\ \frac{\omega}{\pi}\int_0^T \boldsymbol{p}(t)m_1 \cos\omega t dt \\ \frac{\omega}{\pi}\int_0^T \boldsymbol{p}(t)m_1 \sin\omega t dt \\ \vdots \\ \frac{\omega}{\pi}\int_0^T \boldsymbol{p}(t)\cos m_n\omega t dt \\ \frac{\omega}{\pi}\int_0^T \boldsymbol{p}(t)\sin m_n\omega t dt \end{Bmatrix} \tag{7}$$

Equation (4) can be solved using the Newton–Raphson method (Ferri 1986). The number of harmonics included must be considered as it increases the size of Equation (4), and thus, increases the computation time. Models with prohibitively large linear system matrices can make use of reduction techniques (e.g. Guyan reduction) to reduce computational cost.

4.2.2 The integrated MHB-ECRE approach

By integrating MHB and ECRE, we seek to minimize the constitutive error of the system. This constitutive error, E_ω^2, accounts for the uncertainties in both the model predictions and the experimental measurements and is expressed as:

$$E_\omega^2 = \boldsymbol{r}_\omega^T \mathcal{K} \boldsymbol{r}_\omega + \alpha (\boldsymbol{H}\boldsymbol{Q}_\omega - \boldsymbol{Q}_\omega^e)^T \mathcal{K}_R (\boldsymbol{H}\boldsymbol{Q}_\omega - \boldsymbol{Q}_\omega^e) \tag{8}$$

where $\mathcal{K} \in \Re^{(2n+1)N,(2n+1)N}$ is the multi-harmonic stiffness matrix (Isasa et al, 2011) and is expressed as:

$$\mathcal{K} = \begin{pmatrix} \boldsymbol{K} & 0 & \cdots & 0 & 0 \\ 0 & \boldsymbol{K} & \cdots & 0 & 0 \\ \vdots & \vdots & \ddots & \vdots & \vdots \\ 0 & 0 & \cdots & \boldsymbol{K} & 0 \\ 0 & 0 & \cdots & 0 & \boldsymbol{K} \end{pmatrix} \tag{9}$$

In Equation (8), Q_ω is the multi-harmonic coefficient vector that is expanded from experimentally identified, multi-harmonic coefficients to the total number of DOFs in the numerical model; and $\boldsymbol{Q}_\omega^e$ is the experimentally identified, multi-harmonic coefficient

vector that is generated based on the experimentally measured time history response. In this study, only excitation with a constant frequency is considered; hence, $\boldsymbol{Q}_{\omega}^{e}$ is obtained using a Fourier series expansion and harmonic curve fitting. In Equation (8), $\boldsymbol{r}_{\omega} = \boldsymbol{Q}_{\omega} - \boldsymbol{V}_{\omega}$ is the relative multi-harmonic coefficient vector that accounts for the discrepancy between model predictions and experimental measurements. $\boldsymbol{V}_{\omega}$ expresses the multi-harmonic coefficients obtained from model predictions. $\boldsymbol{H}$ is a transformation matrix that reduces the multi-harmonic coefficient matrix for all DOFs to the size of the measured DOFs. α is a weighting factor that accounts for the confidence level of experimental measurements (Deraemaeker et al. 2002). Finally, $\mathcal{K}_{R}$ is the $(2n+1)N_e \times (2n+1)N_e$ reduced multi-harmonic stiffness matrix of the numerical model obtained by model reduction, where N_e is the number of measured DOFs.

To evaluate $\boldsymbol{r}_{\omega}$ and $\boldsymbol{Q}_{\omega}$, we solve the following minimization problem:

Minimize cost function: $E_{\omega}^{2} = \boldsymbol{r}_{\omega}^{T} \mathcal{K} \boldsymbol{r}_{\omega} + \alpha (\boldsymbol{H}\boldsymbol{Q}_{\omega} - \boldsymbol{Q}_{\omega}^{e})^{T} \mathcal{K}_{R} (\boldsymbol{H}\boldsymbol{Q}_{\omega} - \boldsymbol{Q}_{\omega}^{e})$ (10a)

Subjected to constraint relationship: $\mathcal{Z}(\omega)\boldsymbol{Q}_{\omega} + \boldsymbol{F}(\boldsymbol{Q}_{\omega}, \omega) - \boldsymbol{P} = \mathcal{K}\boldsymbol{r}_{\omega}$ (10b)

The constraint in Equation (10b) can be dualized using a Lagrange multiplier to form an unconstrained minimization problem.

4.3 Calibrating the models of nonlinear dynamical systems: Iterative Integrated MHB and ECRE (IIME)

The two-step process presented herein is conceived to identify the residual errors in the underlying linear system and those in the nonlinear component. The strategy implemented involves measuring the dynamical system vibration response under low magnitude periodic excitation such that the system vibration response is predominantly linear. Using this low magnitude excitation ($\boldsymbol{P}_1$) data, the experimental multi-harmonic coefficients ($\boldsymbol{Q}^e_{\omega 1}$) are first obtained. Next, model-predicted multi-harmonic coefficients ($\boldsymbol{V}_{\omega 1}$) are calculated and experimental multi-harmonic coefficients ($\boldsymbol{Q}_{\omega 1}$) are expanded to match the degrees of freedom of the numerical model. Through the error minimization step of ECRE, the difference between experimental multi-harmonic coefficient and model predicted multi-harmonic coefficient vectors ($\boldsymbol{Q}_{\omega 1} - \boldsymbol{V}_{\omega 1}$) is calculated. The knowledge of this disagreement, combined with the stiffness matrix, allows us to calculate the elemental residual energy. The elements with high residual energy indicate the existence of higher model error (Hu et al. 2017), and thus, the model parameters associated with these elements are selected for calibration. This model error localization step is useful for parameter selection (Larsson and Abrahamsson 1999; Kim and Park 2004; Hu et al. 2017), because the number of parameters that need to be calibrated can often be significantly reduced in

this step, which in turn helps mitigate the risk of rank deficiency and ill-conditioning during calibration (Yu et al. 2007).

In the second step, a higher magnitude periodic excitation is applied to obtain the nonlinear dynamic displacement response and the corresponding multi-harmonic coefficient is calculated ($\boldsymbol{Q}_{\omega 2}^{e}$). Using both multi-harmonic coefficients, $\boldsymbol{Q}_{\omega 1}$ and $\boldsymbol{Q}_{\omega 2}$, linear and nonlinear model parameters are calibrated by minimizing the sum of the residual energy calculated for both excitation magnitudes ($\boldsymbol{P}_1$ and $\boldsymbol{P}_2$). This way the model error in the locally nonlinear component is accurately identified all while errors in the modeling of the underlying linear system are corrected. Figure 1 schematically shows the proposed method as divided into two steps: localization and parameter calibration. The details of these two steps are given below:

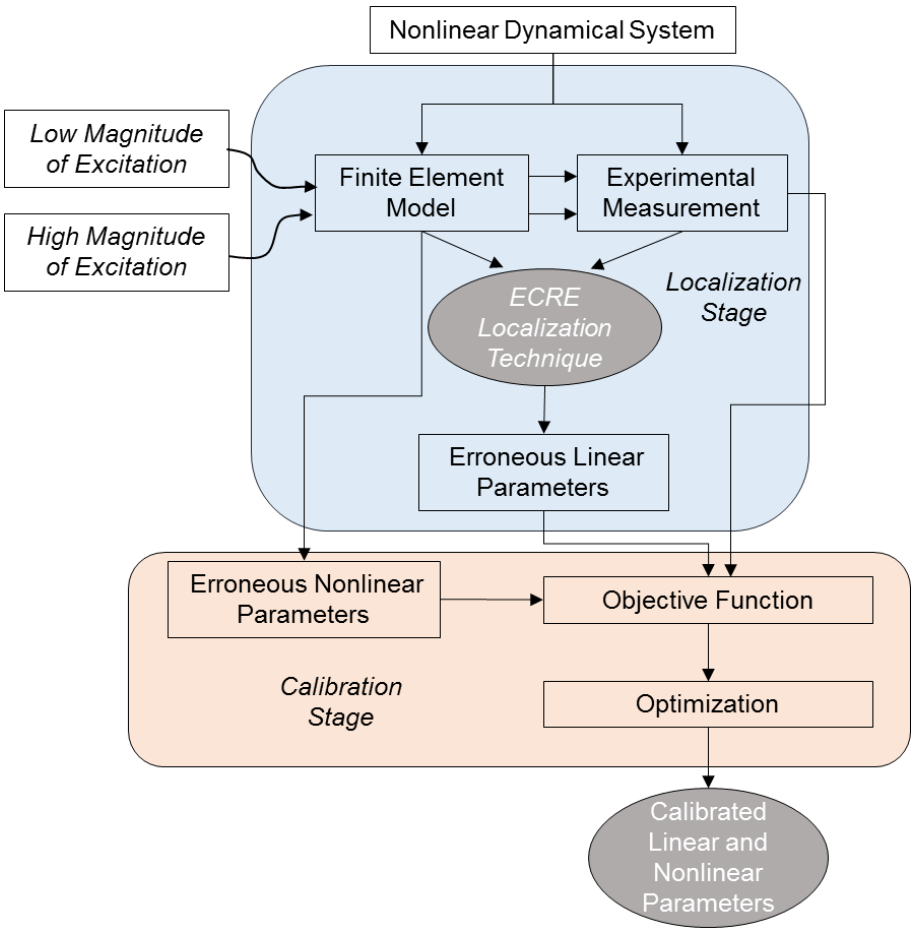

Figure 4.1. The calibration procedure for the proposed method

Step 1. Model error localization using low magnitude excitation, $\boldsymbol{P}_1$

Based on the system response to low magnitude excitation, the optimization problem is formulated in Equation (11) that minimizes the residual energy between the numerical model and the measurements. To minimize the objective function, we formulate a saddle-point problem with the introduction of Lagrange multipliers. Equation (11) yields the system of the nonlinear equations shown in Equation (12), based on which the two unknown multi-harmonic coefficient vectors, $\boldsymbol{r}_{\omega 1}$ and $\boldsymbol{Q}_{\omega 1}$, that represent the predominantly linear dynamic response features can be solved. The relative multi-harmonic coefficient vector $\boldsymbol{r}_{\omega 1}$, combined with elemental stiffness matrix, is then used for localizing the model error in the linear component. Therefore, the linear parameters that are associated with identified model error, E_L, are selected from a large candidate set of parameters for the calibration in the next step.

Minimize the cost function for force level $\boldsymbol{P}_1$:

$$E_{\omega 1}^2 = \boldsymbol{r}_{\omega 1}^T \mathcal{K} \boldsymbol{r}_{\omega 1} + \alpha (\boldsymbol{H}\boldsymbol{Q}_{\omega 1} - \boldsymbol{Q}_{\omega 1}^e)^T \mathcal{K}_R (\boldsymbol{H}\boldsymbol{Q}_{\omega 1} - \boldsymbol{Q}_{\omega 1}^e) \tag{11a}$$

Subjected to constraint relationship: $\mathcal{Z}(\omega)\boldsymbol{Q}_{\omega 1} + F(\boldsymbol{Q}_{\omega 1}, \omega, K_{NL}) - \boldsymbol{P}_1 = \mathcal{K}\boldsymbol{r}_{\omega 1}$ (11b)

Nonlinear matrix equation:

$$\begin{pmatrix} \mathcal{Z}(\omega) + \dfrac{\partial \boldsymbol{F}(\boldsymbol{Q}_{\omega 1}, \omega, K_{NL})}{\partial \boldsymbol{Q}_{\omega 1}} & \alpha \boldsymbol{H}^T \mathcal{K}_R \boldsymbol{H} \\ \mathcal{K} & -\mathcal{Z}(\omega) \end{pmatrix} \begin{Bmatrix} \boldsymbol{r}_{\omega 1} \\ \boldsymbol{Q}_{\omega 1} \end{Bmatrix} + \begin{Bmatrix} 0 \\ -\boldsymbol{F}(\boldsymbol{Q}_{\omega 1}, \omega, K_{NL}) \end{Bmatrix} = \begin{Bmatrix} \alpha \boldsymbol{H}^T \mathcal{K}_R \boldsymbol{Q}_{\omega 1}^e \\ -\boldsymbol{P}_1 \end{Bmatrix} \tag{12}$$

Step 2. Nonlinear model calibration using both low and high magnitude excitations, $\boldsymbol{P}_1$ and $\boldsymbol{P}_2$

In the second step, we combine the measurements of multi-harmonic coefficients for both low and high magnitude excitations. The sum of the residual energy for both excitation magnitudes is then minimized.

Minimize the cost function for $\boldsymbol{P}_1$ and $\boldsymbol{P}_2$:

$$\begin{aligned} E^2_{\omega\_combined} &= \boldsymbol{r}_{\omega 1}^T \mathcal{K} \boldsymbol{r}_{\omega 1} + \alpha (\boldsymbol{H}\boldsymbol{Q}_{\omega 1} - \boldsymbol{Q}^e_{\omega 1})^T \mathcal{K}_R (\boldsymbol{H}\boldsymbol{Q}_{\omega 1} - \boldsymbol{Q}^e_{\omega 1}) \\ &+ \boldsymbol{r}_{\omega 2}^T \mathcal{K} \boldsymbol{r}_{\omega 2} + \alpha (\boldsymbol{H}\boldsymbol{Q}_{\omega 2} - \boldsymbol{Q}^e_{\omega 2})^T \mathcal{K}_R (\boldsymbol{H}\boldsymbol{Q}_{\omega 2} - \boldsymbol{Q}^e_{\omega 2}) \end{aligned} \tag{13a}$$

Subjected to the following constraints:

$$\mathcal{Z}(\omega)\boldsymbol{Q}_{\omega 1} + \boldsymbol{F}(\boldsymbol{Q}_{\omega 1}, \omega, K_{NL}) - \boldsymbol{P}_1 = \mathcal{K}\boldsymbol{r}_{\omega 1} \tag{13b}$$

$$\mathcal{Z}(\omega)\boldsymbol{Q}_{\omega 2} + \boldsymbol{F}(\boldsymbol{Q}_{\omega 2}, \omega, K_{NL}) - \boldsymbol{P}_2 = \mathcal{K}\boldsymbol{r}_{\omega 2} \tag{13c}$$

A new cost function g_c is obtained after applying the Lagrange multipliers and is expressed as follows:

$$\begin{aligned} g_c &= \boldsymbol{r}_{\omega 1}^T \mathcal{K} \boldsymbol{r}_{\omega 1} + \alpha (\boldsymbol{H}\boldsymbol{Q}_{\omega 1} - \boldsymbol{Q}^e_{\omega 1})^T \mathcal{K}_R (\boldsymbol{H}\boldsymbol{Q}_{\omega 1} - \boldsymbol{Q}^e_{\omega 1}) \\ &+ \psi_1^T (\mathcal{K}\boldsymbol{r}_{\omega 1} - \mathcal{Z}(\omega)\boldsymbol{Q}_{\omega 1} - \boldsymbol{F}(\boldsymbol{Q}_{\omega 1}, \omega, K_{NL}) + \boldsymbol{P}_1) \\ &+ \boldsymbol{r}_{\omega 2}^T \mathcal{K} \boldsymbol{r}_{\omega 2} + \alpha (\boldsymbol{H}\boldsymbol{Q}_{\omega 2} - \boldsymbol{Q}^e_{\omega 2})^T \mathcal{K}_R (\boldsymbol{H}\boldsymbol{Q}_{\omega 2} - \boldsymbol{Q}^e_{\omega 2}) \\ &+ \psi_2^T (\mathcal{K}\boldsymbol{r}_{\omega 2} - \mathcal{Z}(\omega)\boldsymbol{Q}_{\omega 2} - \boldsymbol{F}(\boldsymbol{Q}_{\omega 2}, \omega, K_{NL}) + \boldsymbol{P}_2) \end{aligned} \tag{14}$$

where ψ_1 and ψ_2 are the Lagrange multipliers for the constraint relationships for $\boldsymbol{P}_1$ and $\boldsymbol{P}_2$, respectively. Through the calculation of the stationary conditions of g_c with respect to the unknowns $\boldsymbol{r}_{\omega 1}$, $\boldsymbol{Q}_{\omega 1}$, $\boldsymbol{r}_{\omega 2}$, $\boldsymbol{Q}_{\omega 2}$, E_L, K_{NL}, ψ_1, and ψ_2, the solution of Equation (14) is calculated using the following matrix relationship:

$$\begin{bmatrix} \mathcal{Z}(\omega)+\frac{\partial \boldsymbol{F}(\boldsymbol{Q}_{\omega 1},\omega,K_{NL})}{\partial \boldsymbol{Q}_{\omega 1}} & \alpha \boldsymbol{H}^T \mathcal{K}_R \boldsymbol{H} & 0 & 0 & 0 & 0 \\ \mathcal{K} & -\mathcal{Z}(\omega) & 0 & 0 & 0 & 0 \\ 0 & 0 & \mathcal{Z}(\omega)+\frac{\partial \boldsymbol{F}(\boldsymbol{Q}_{\omega 2},\omega,K_{NL})}{\partial \boldsymbol{Q}_{\omega 2}} & \alpha \boldsymbol{H}^T \mathcal{K}_R \boldsymbol{H} & 0 & 0 \\ 0 & 0 & \mathcal{K} & -\mathcal{Z}(\omega) & 0 & 0 \\ 0 & 0 & 0 & 0 & 0 & 0 \\ 0 & 0 & 0 & 0 & 0 & 0 \end{bmatrix} \begin{Bmatrix} \boldsymbol{r}_{\omega 1} \\ \boldsymbol{Q}_{\omega 1} \\ \boldsymbol{r}_{\omega 2} \\ \boldsymbol{Q}_{\omega 2} \\ E_L \\ K_{NL} \end{Bmatrix}$$

$$+\begin{Bmatrix} 0 \\ -\boldsymbol{F}(\boldsymbol{Q}_{\omega 1},\omega,K_{NL}) \\ 0 \\ -\boldsymbol{F}(\boldsymbol{Q}_{\omega 2},\omega,K_{NL}) \\ \frac{\partial g}{\partial E_L} \\ \frac{\partial g}{\partial K_{NL}} \end{Bmatrix} = \begin{Bmatrix} \alpha \boldsymbol{H}^T \mathcal{K}_R \boldsymbol{Q}^e_{\omega 1} \\ -\boldsymbol{P}_1 \\ \alpha \boldsymbol{H}^T \mathcal{K}_R \boldsymbol{Q}^e_{\omega 2} \\ -\boldsymbol{P}_2 \\ 0 \\ 0 \end{Bmatrix}$$

(15)

where E_L are the linear structural parameters corresponding to the identified model error in the linear component.

All the above objective functions are convex, thus facilitating the use of efficient local optimization algorithms in the calibration process. A modified Newton-Raphson algorithm is chosen to solve this nonlinear problem due to its desirable convergence characteristics (Nocedal and Wright 2006; Stevens et al. 2017) and because the parameter gradients are calculated numerically. In each of the Newton-Raphson iterations, the parameters are calibrated and the residual error term is recalculated. A new iteration consisting of a localization step and a correction step is performed until the prescribed convergence criterion is satisfied.

Instead of iteratively calibrating the parameters corresponding to linear and nonlinear behavior (i.e. using IIME), calibration can also be conducted based on a discrete set of inputs−henceforth referred to as Discrete Integrated MHB-ECRE (DIME). In the DIME approach, a sample set of values are generated for the poorly-known model input parameters and then used for calculation of the residual energy using Equation (13) and (14). As such, the minimum residual energy is expected to be achieved when the calibration parameters associated with the linear and nonlinear components are closest to the true parameter values. In DIME, a large number of instances must be calculated, which means the discrete approach is more computationally demanding than IIME. In the following section, the results obtained with the DIME approach are used as a reference to compare against those obtained with the proposed two-step IIME approach.

4.4 Benchmark beam model application

4.4.1 The description of the numerical model

The proposed approach is demonstrated on a simulated academic example based on the COST action F3 project benchmark structure developed at Ecole Centrale de Lyon (Thouverez 2003; Worden 2003). The model consists of a main beam clamped to a thin, secondary beam with both ends of the structure clamped to fixed supports (see Figure 2). The main beam has a length of 0.7 m and a thickness of 0.014 m, whereas the secondary beam has a length of 0.04 m with a thickness of $5x10^{-4}$ m. Both beams have a width of

0.014 m and are comprised of steel with a Young's modulus of 210 GPa and a Poisson's ratio of 0.33. Table 1 lists the reference configuration of the F3 project benchmark model. The main beam is modeled with seven elements and the secondary beam with four elements as shown in Figure 2. The connection of the beams is modeled by a semi-rigid, rotational spring and a grounded, translational spring element with cubic stiffness such that the nodes are constrained to have the same translation displacement, but allowed to have different rotations. The value of the cubic stiffness (K_{NL}) is set to be 6.1×10^9 N/m.

Table 1. Reference configuration of the benchmark beam model

Symbol	Parameter	Value
L_1	Length of Main Beam	0.7 m
L_2	Length of Thin Beam	0.04m
b	Width of Cross Section	0.14 m
h_1	Height of Main Beam	0.14 m
h_2	Height of Thin Beam	0.0005 m
ρ	Density	7830 kg/m^3
E	Young's modulus	210 GPa
ν	Poisson's ratio	0.33
N_{node}	Node Number	12
N_{dof}	DOF Number	21
N_e	Beam Element Number	11
N_m	Measured Dofs	21

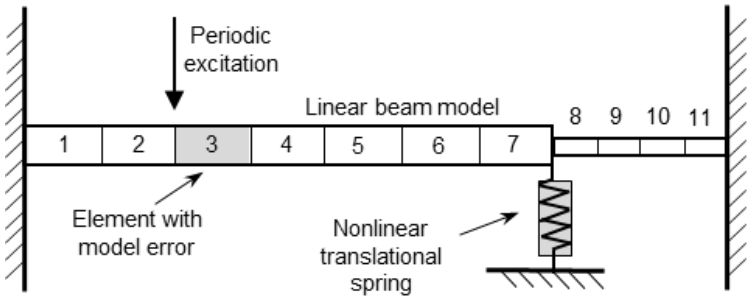

Figure 4.2. A linear beam model with local nonlinearity under periodic excitation.

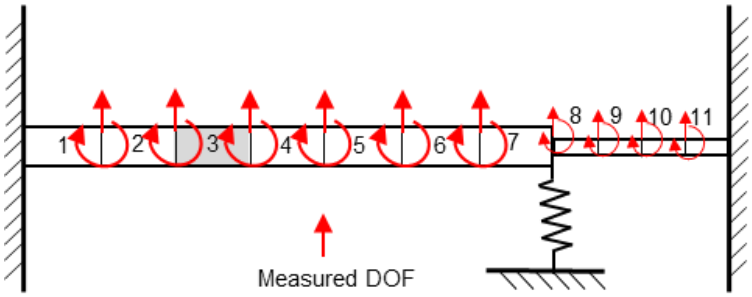

Figure 4.3. The experimentally measured translational and rotational DOFs.

Vibration response measurements are synthetically generated for 21 DOFs along the beam as shown in Figure 3. For the low magnitude excitation, a stepped sine force with a magnitude of 0.5 N and frequency of 32 Hz, selected based on the value of the fundamental frequency of the linear beam, is applied to the structure. For the high magnitude excitation, a stepped sine force with a magnitude of 5 N and frequency of 32 Hz is applied to ensure sufficiently large deflections to observe the nonlinear dynamic effects. In addition, simulated measurement noise is introduced as an additive zero mean Gaussian white noise at a level of 5% of the maximum displacement time history response. The noise is added to the time history measurements before the experimental multi-harmonic coefficients vectors are calculated.

The initial model is preset to have error in two distinct forms (recall Figure 2): (i) model error in the linear beam structure that is simulated by intentionally reducing the Young's modulus for element 3 by 50% (i.e. 105 GPa); (ii) model error in the nonlinear spring that is simulated by intentionally altering the stiffness coefficient with cubic nonlinearity by 50% (i.e. 3.05×10^9 N/m).

4.4.2 The conventional approach: MHB-ECRE using only high magnitude excitation

This section presents the results of the conventional, one-step MHB-ECRE approach in which the parameter of the nonlinear translational stiffness (K_{NL}) is calibrated with the presumption that the model of the underlying linear system is error-free. The effect of the model error in the linear beam on the results of this conventional approach is evaluated using both a model with and without the manually introduced reduction in the Young's modulus of element 3.

Owing to the need that the structure's dynamic response must exhibit nonlinear behavior for the one-step MHB-ECRE method, synthetic response measurements are generated by the model under the high amplitude excitation (5 N), using which the ECRE values are calculated by solving Equation (11).

Figure 4 depicts the ECRE values obtained for a range of nonlinear stiffness values where the correction coefficient that multiplies the nonlinear stiffness parameter (K_{NL})

varies from 0.5 to 1.5 with an interval of 0.1, essentially representing a correction of 50% below and above the nominal stiffness value. For this given range of nonlinear stiffness coefficients, the residual energy is calculated using both the 'exact' linear model (the solid curve in Figure 4) and the 'erroneous' linear model (i.e. one with a reduced Young's modulus in element 3; the dashed curve in Figure 4). The results shown in Figure 4 indicate that the linear model error leads to a 30% deviation from the true value for the identified nonlinear stiffness parameter. This difference is due to the fact that the ECRE values are biased by the model error present in the linear component and thus, the minima no longer corresponds to the *true* value of the nonlinear stiffness.

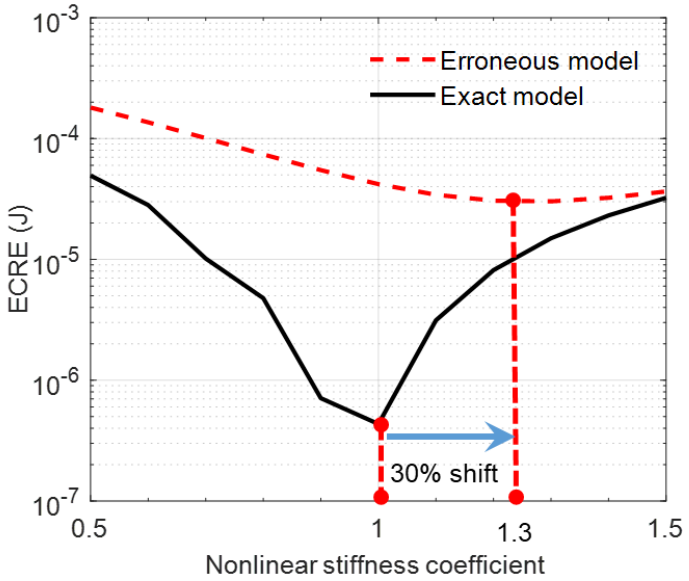

Figure 4.4. Nonlinear parameter identification result when the linear stiffness coefficient is 0.5 and 1.

4.3 The two-step approach: MHB-ECRE using two excitation magnitudes

In this section, the proposed, iterative, two-step approach is used to calibrate the model input parameters of both the Young's modulus of element 3 and the nonlinear stiffness (K_{NL}) and verify its ability to accurately calibrate the parameters without suffering the confounding effects of error in both the linear and nonlinear components of the structure. The efficiency of this iterative approach in its search algorithm to find the optimal input parameters is compared to the discrete (DIME) approach which tests over a grid sampling of possible parameters.

The structure is excited at node 3 using the lower amplitude periodic force (0.5N) to obtain the synthetic structural vibration response with negligible nonlinear effects. As shown in Figure 5 (a), the nonlinear effects lead to only a 1.5% shift in the fundamental frequency of the structural system, while no significant distortion can be observed in the Frequency Response Function (FRF) of the nonlinear beam model with respect to the linear model. Hence, the obtained dynamic response is predominantly linear. The ECRE calculated for all beam elements is shown in Figure 6. From the figure, element 3 (E_L) is identified with the highest ECRE value, which is consistent with the fact that an incorrect Young's modulus value is assigned for this element.

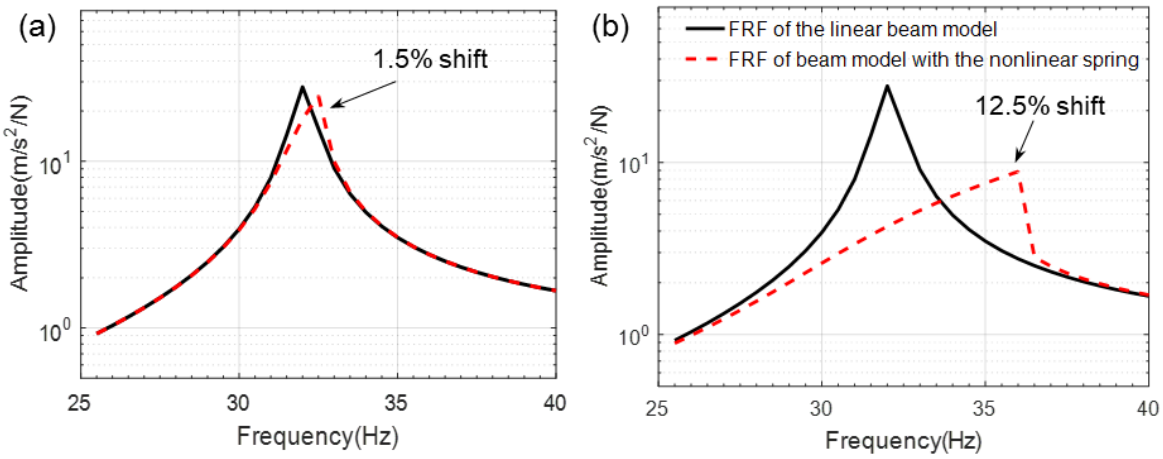

Figure 4.5. Comparison of FRFs at node 8 for the linear beam model with and without the nonlinear spring: (a) a low magnitude excitation of 0.5 N is applied; (b) a high magnitude excitation of 5 N is applied.

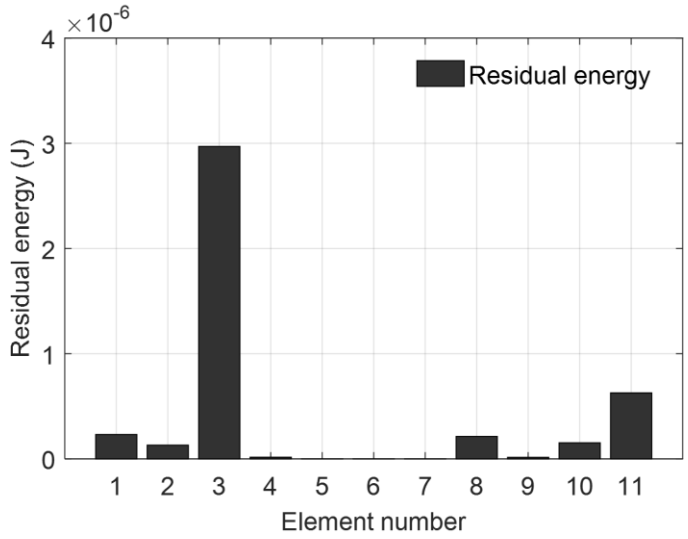

Figure 4.6. The ECRE localization of model error in linear component.

The structure is then excited at the same location using the higher amplitude periodic excitation (5N) to observe the synthetic nonlinear vibration. The FRF of the translational DOF associated with the nonlinear spring is presented in Figure 5 (b). A

significant distortion of 12.5% in the FRF plots is observed where the peaks shift from 32 to 36 Hz under high magnitude excitation, confirming that a sufficiently high force is applied to observe the nonlinear response.

Both IIME and DIME approaches are used to calibrate the selected model parameters as presented in the Figure 7. The IIME approach is applied by solving Equation (15) using the Newton-Raphson algorithm. The convergence threshold for the IIME approach is set to 10^{-10} for the norm of the relative solution vector between iterations. In Figure 7, it is noticed that the IIME approach is completed within 5 iterations. The calibrated linear and nonlinear model parameters are 210.21 GPa and 6.08×10^{9} N/m, respectively, which represent a 0.1% and 0.4% deviation from the true values, respectively. The detailed calibration results for each iteration are also provided in Table 2. For the DIME approach, a range of coefficients that multiply the nonlinear stiffness (K_{NL}) and Young's modulus in the linear component (E_L) is created from 50% to 150% of the true value with an interval of 10%. These pre-defined sets of model parameters are substituted into Equation (15) and a surface plot of the residual energy is shown in Figure 7. The detailed calibration results for each iteration are also provided in Table 2.

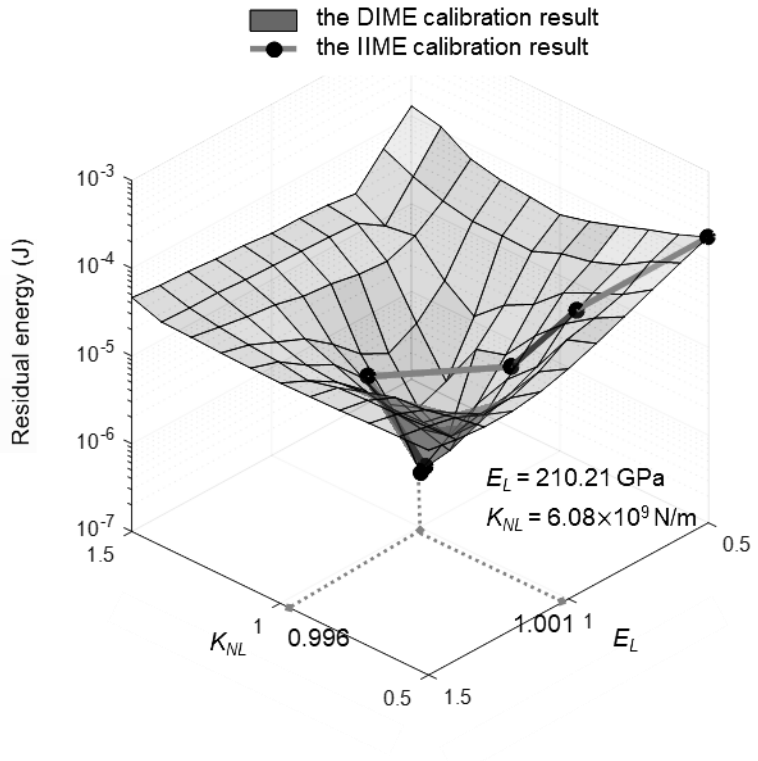

Figure 4.7. The calibration result for the linear and nonlinear parameters

Table 2. Model calibration results using IIME approach.

Iteration number	Calibrated linear parameter (GPa)	Percentage error	Calibrated nonlinear parameter (N/m)	Percentage error	ECRE
0	105	-50.00%	3.05×10^{9}	-50.00%	1.81×10^{-5}
1	159.18	-24.20%	4.28×10^{9}	-29.80%	3.50×10^{-5}
2	182.28	-13.20%	4.98×10^{9}	-18.30%	7.91×10^{-6}
3	223.86	6.60%	6.80×10^{9}	11.50%	4.40×10^{-6}
4	210.21	0.10%	5.99×10^{9}	-1.80%	5.18×10^{-7}
5	210.21	0.10%	6.08×10^{9}	-0.40%	4.34×10^{-7}

4.5 Discussions on the performance of proposed method

In this section, the impact of measurement noise, number of response measurement locations, and model error location on the accuracy of the proposed method is examined.

The purpose of conducting these studies is to evaluate the proposed approach's robustness and to understand how the method performs under a variety of realistic scenarios. All the calibration results presented in this section are obtained using an identical procedure as detailed in Section 4.

4.5.1 Model calibration considering varying noise levels

All practical experimental data is inevitably contaminated by noise to some degree (Modak et al. 2002). To assess the impact of measurement noise, in this section, the performance of the proposed model calibration method is evaluated in the presence of varying levels of noise. Accordingly, the two-step model calibration process is applied in the presence of zero mean Gaussian white noise with varying standard deviations of 5%, 10%, 15%, and 20%. For each noise level, 10 random realizations of noise are generated to contaminate the time history data and the calibrated model parameters are obtained using these contaminated measurements.

The mean and standard deviation for the calibrated stiffness coefficients for these ten realizations are shown in Figure 8. The solid line in Figure 8 shows that the linear stiffness parameter is estimated with less than 1% deviation from the true value when the noise level is less than 15%. With 20% noise, the calibrated linear stiffness parameter deviates by 5.6%. The calibrated nonlinear stiffness parameter is observed to be more sensitive to the measurement noise. The dashed line in Figure 8 shows that the nonlinear

stiffness parameter is accurately estimated with less than 1% deviation when the noise level is less than 10%. As the noise level increases to 15% and 20%, the calibrated nonlinear stiffness parameter deviates by 6.1% and 11.2%, respectively.

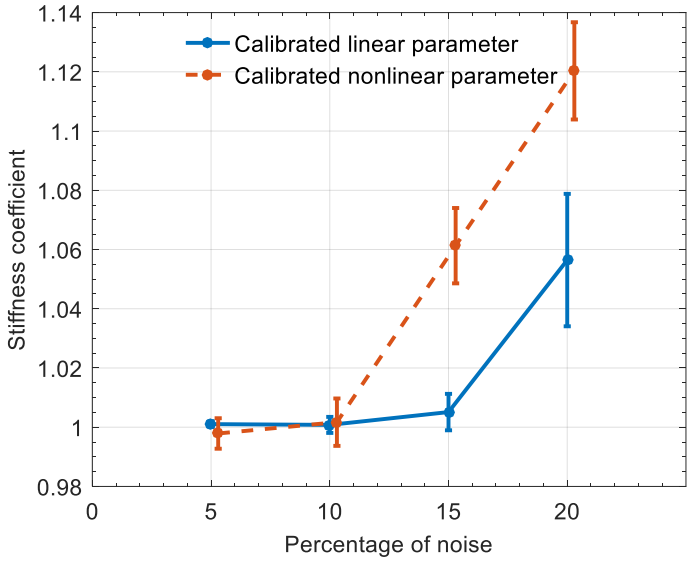

Figure 4.8. The effect of multiple noise levels on parameter calibration results

4.5.2 Model calibration with reduced set of measurements.

In practical application, the number of measured response locations is limited by the feasible number of sensors, measurement channels available, and the inaccessibility of some measurement locations (Majumder and Manohar 2003). To assess the effect of such limitations, this section evaluates he performance of the proposed two-step model calibration approach by hypothetically reducing the set of measured DOFs. Three reduced sets of measurements are used to obtain the multi-harmonic coefficient vectors as shown in Figure 9. The first two measurements are with 10 (Figure 9 (a)) and 5 (Figure 9 (b))

translational DOFs including the DOF at the nonlinear spring, while the last set of measurements is with 5 (Figure 9 (c)) translational DOFs excluding the DOF at the nonlinear component. Using the reduced set of measurements, the residual energy plot for model error localization is shown in Figure 10.

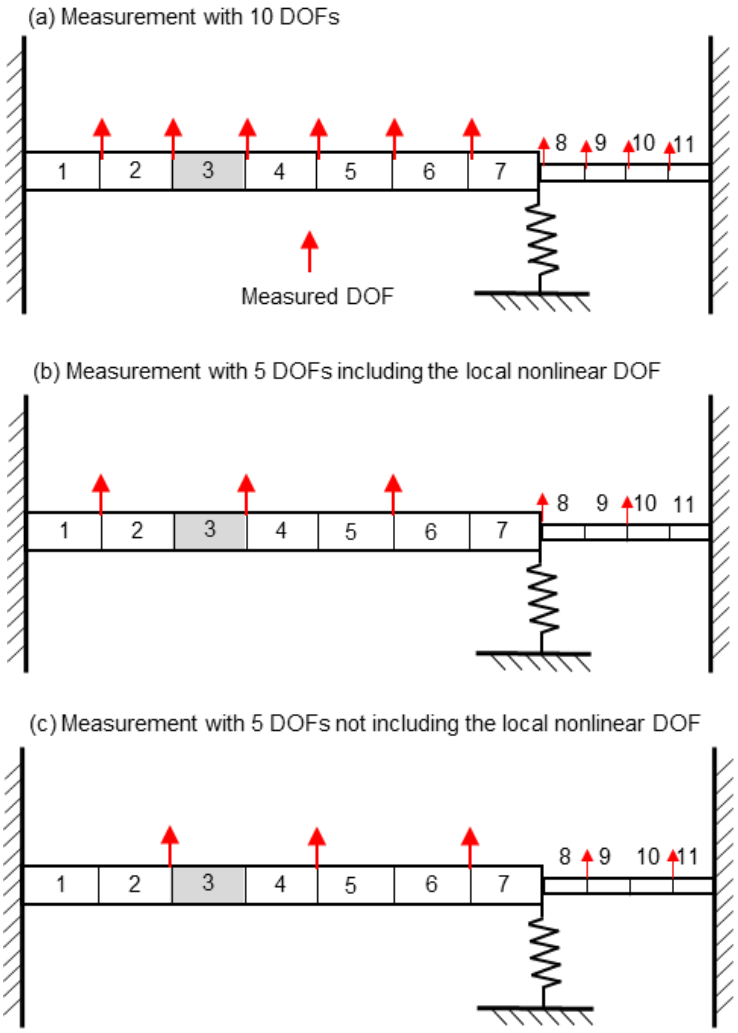

Figure 4.9. Three sets of reduced DOF measurements.

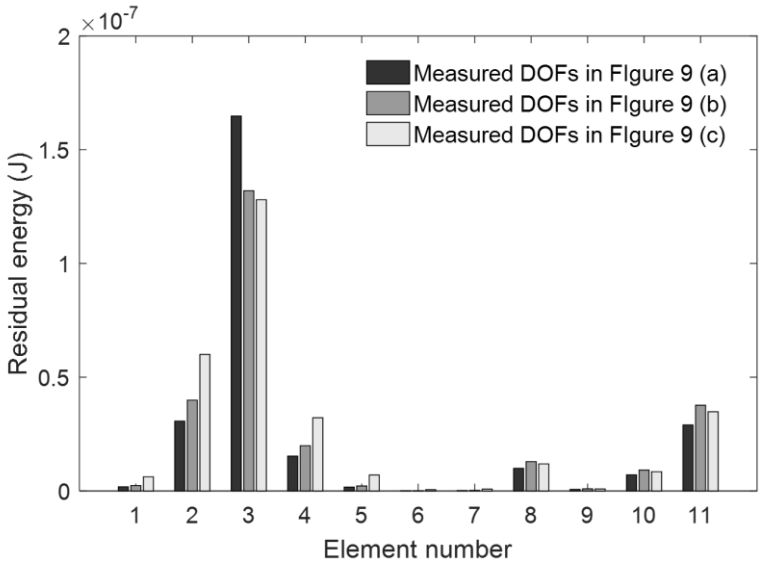

Figure 4.10. The ECRE localization of linear model error using reduced sets of measurements.

As seen in Figure 11, the calibrated values for the nonlinear stiffness coefficient match the true parameter values even when the number of measurements is as low as 5 DOFs. The value of the parameter associated with the linear element with error is correctly calibrated with 10 measured DOFs, while an 8% deviation from the true values is present when only 5 DOFs are measured. When the DOF at the nonlinear spring is not included in the measurement, Figure 12 shows that the linear calibrated stiffness coefficient has a 12.3% deviation from the true value, and the nonlinear calibrated stiffness coefficient has a 26.1% deviation from the true value. The calibration of the nonlinear stiffness coefficient parameter is less affected by a reduced set of measurements as long as the response associated with the nonlinear spring is measured. It is concluded that it is important to

measure the response as close to where local nonlinearity is present as possible to ensure the accuracy of the results of the proposed model calibration method.

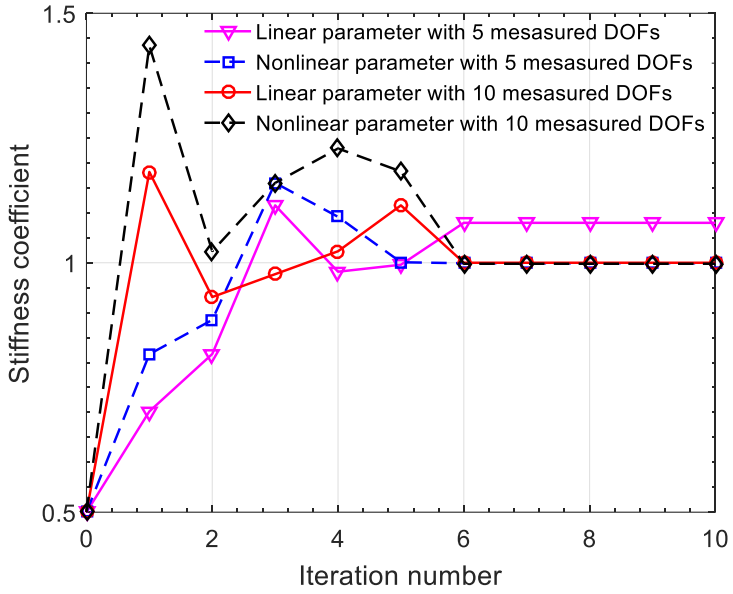

Figure 4.11. Calibration results with fewer measured DOFs (the nonlinear DOF is included).

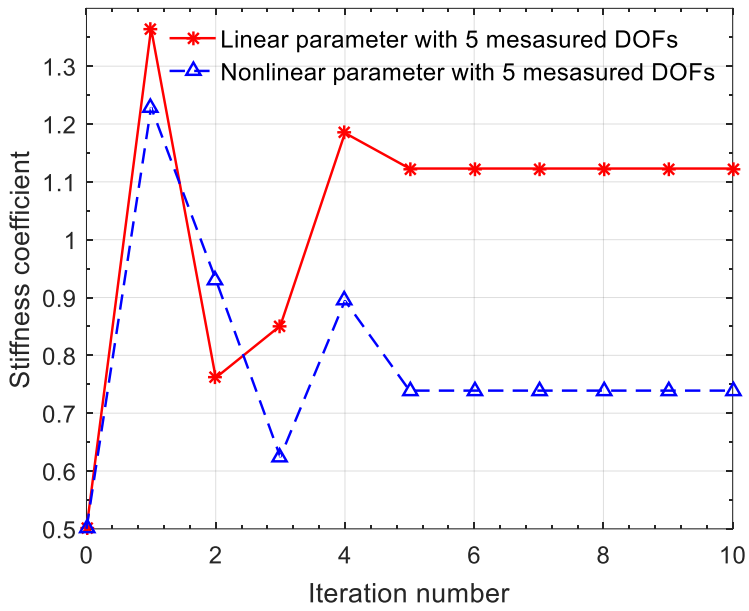

Figure 4.12. Calibration results with 5 measured DOFs (not including the nonlinear DOF).

4.5.3 The effect of model error location

The objective of this section is to investigate the effect the spatial distribution of modeling error on the linear system on the obtained results for the calibrated model. Specifically, we introduced model error to 7 different elements (elements 1 to 7) of the main beam, simulated by reducing the Young's modulus by 50%. The model error in the nonlinear component is kept the same as defined in Section 4 for the seven sets of calibration cases. The proposed approach is applied to calibrate the linear and nonlinear structural component parameters, and the calibration results are plotted in Figure 13 (a) and (b), respectively. As shown in the Figure 13 (a) and (b), the convergence rate to the true value for the linear and nonlinear stiffness parameters is similar (five iterations) for all

seven cases regardless of the model error location.

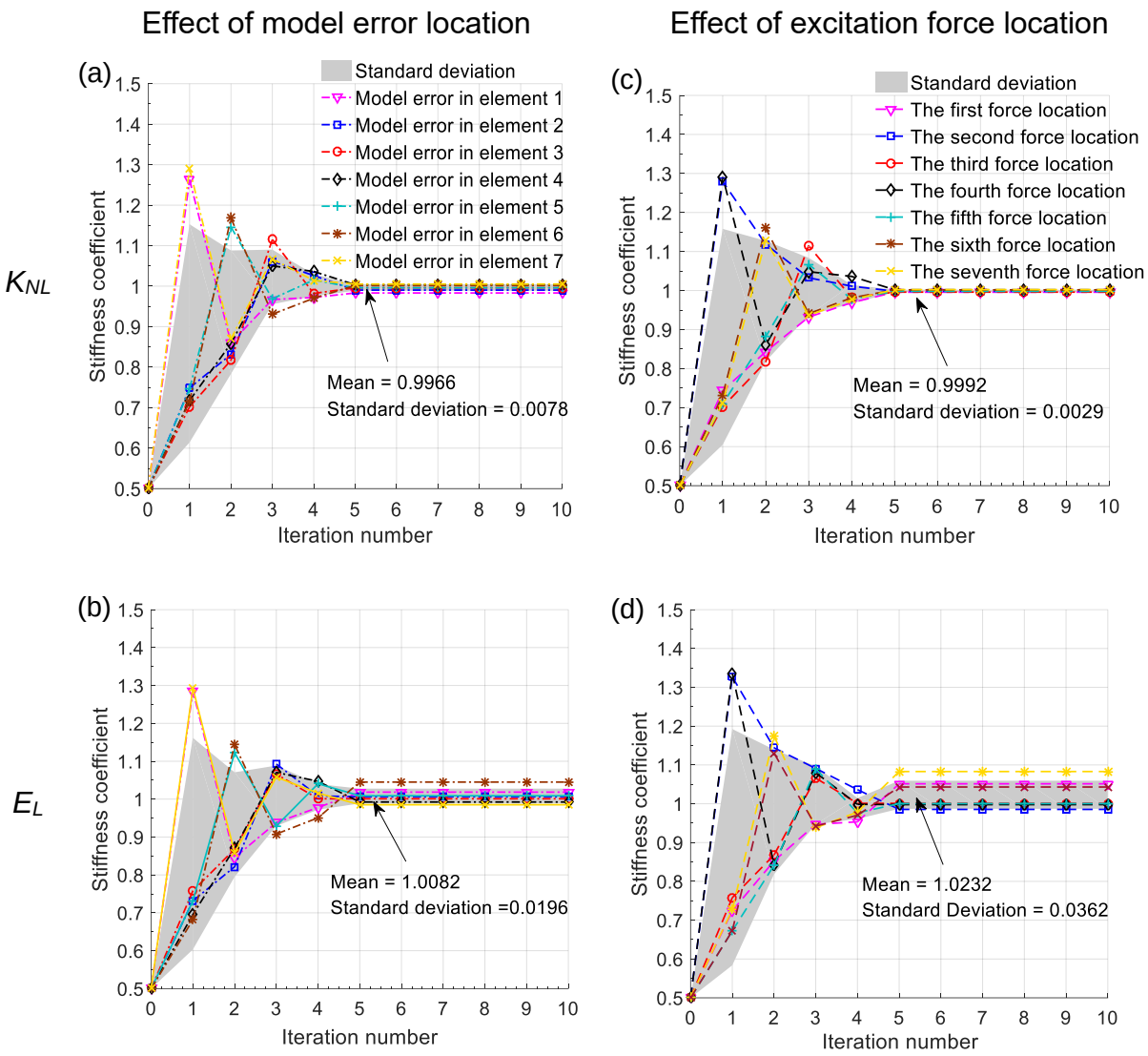

Figure 4.13. Calibration results considering the effect of model error location and excitation force location.

4.5.4 The effect of excitation force location

In this section, the effect of the location of the excitation force, and thus the distance between the applied force location and nonlinear spring component on the performance of model calibration results is evaluated (see Figure 14). Similar to the calibration results

presented in Section 5.3, the unknown structural parameters mostly converge to the true value with the proposed calibration approach. The calibration results for all seven force locations are presented in Figure 13 (c) and (d). Figure 13 (c) shows that the averaged calibrated nonlinear stiffness coefficient relative to the true value for different locations is 0.9992 with a standard deviation of 0.0029.

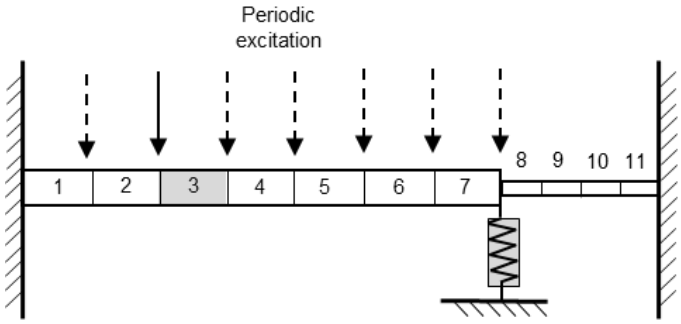

Figure 4.14. Seven locations for applied excitation force.

Compared to the calibration of the nonlinear structural parameter, the average calibrated linear stiffness coefficient is 1.0232, which deviates slightly from the true parameter value (see Figure 13 (d)). Also, a larger standard deviation of 0.0362 is observed relative to the nonlinear stiffness calibration. Moreover, it can be concluded from Figure 13 (b) and (d) that the calibration of linear model parameters is affected by the location of the excitation force relative to the location of the model error. As the excitation force moves from the left end of the beam to the right end, the calibrated linear parameters deviate more from the true parameter value. This effect may be because as the magnitude of response becomes larger as the distance between force location and nonlinear spring element

decreases, the total response is more likely to be dominated by the nonlinear effect. Thus, the accuracy of the linear parameter calibration results is influenced.

4.6 Conclusion

This paper presents a two-step, nonlinear model calibration framework referred to as IIME that simultaneously corrects modeling error in both linear and nonlinear components based on the combined MHB-ECRE algorithm. An appealing feature of this approach is that modeling errors in the underlying linear model can be isolated and corrected, reducing their degrading effects in the model calibration of the nonlinear component. For this, the modeling errors in the linear system are localized by applying low magnitude excitation that ensures the dynamic response of the system remains predominantly linear. Accordingly, subsequent optimization step for parameter calibration is formulated to determine both the parameters associated with poorly modeled linear components and those associated with the nonlinear components without making any assumptions regarding initial linear model accuracy.

The proposed method has been demonstrated on a numerical example (the F3 project benchmark structure) using synthetic measurements. The results show that the Integrated MHB-ECRE method is capable of calibrating nonlinear models with model error in both linear and nonlinear components. When model error is present in both linear and nonlinear components, this two-step integrated MHB-ECRE calibration approach has

shown superiority to the conventional one-step MHB-ECRE approach, while providing more reliable calibration of the nonlinear component parameter with less dependency on *a priori* knowledge of the accuracy of the associated linear system. An iterative optimization process is developed for solving the calibration problem so that the model parameters can be calibrated with less computational cost and more accurate results compared to a discretized approach.

Work has also been conducted to quantify the influence of measurement noise, a reduced set of measurements, and model error location on the proposed method. These studies show that the method is quite robust against introduced measurement noise, especially in the calibration of the linear component parameter to the true value. In addition, as long as the structural response is measured close to the location of the nonlinearity, the method has shown calibration capability with a relatively scarce set of measured data points. The proposed method has been evaluated for a case that entails a spatially localized nonlinearity, there is room for further work in testing the approach in calibrating other types of nonlinearity, such as nonlinear material properties.

References

Atamturktur, S., Gilligan, C., & Salyards, K. (2013). Detection of Internal Defects in Concrete Members Using Global Vibration Characteristics. *Materials Journal (ACI)*, *110*(5), 529-538.

Atamturktur, S., Hemez, F., & Laman, J. (2012). Uncertainty Quantification in Model Verification and Validation as Applied to Large Scale Historic Masonry Monuments. *Engineering Structures (Elsevier), 43*, 221-234.

Atamturktur, S. & Laman, J. (2012). Finite Element Model Correlation and Calibration of Historic Monuments: Review. *Journal of Structural Design of Tall and Special Buildings (Wiley), 21*(2), 96-113.

Bellizzi, S., & Defilippi, M. (2003). Non-linear mechanical systems identification using linear systems with random parameters. *Mechanical Systems and Signal Processing*, *17*(1), 203-210.

Böswald, M., & Link, M. (2004). Identification of non-linear joint parameters by using frequency response residuals. *In Proceedings of the 2004 International Conference on Noise and Vibration Engineering (ISMA2004), Leuven, Belgium, September*, 20-22.

Cardona, A., Coune, T., Lerusse, A., & Geradin, M. (1994). A multiharmonic method for non-linear vibration analysis. *International Journal for Numerical Methods in Engineering*, *37*(9), 1593-1608.

Clough, R. W., & Wilson, E. L. (1979). Dynamic analysis of large structural systems with local nonlinearities. *Computer Methods in Applied Mechanics and Engineering*, *17*, 107-129.

Deraemaeker, A., Ladevèze, P., & Leconte, P. (2002). Reduced bases for model updating in structural dynamics based on constitutive relation error. *Computer Methods in Applied Mechanics and Engineering*, *191*(21), 2427-2444.

Ewins, D. J., Weekes, B., & Delli Carri, A. (2015). Modal testing for model validation of structures with discrete nonlinearities. *Philosophical Transactions of the Royal Society A*, *373*(2051), 20140410.

Ferreira, J. V., & Serpa, A. L. (2005). Application of the arc-length method in nonlinear frequency response. *Journal of Sound and Vibration*, *284*(1), 133-149.

Ferri, A. A. (1986). On the equivalence of the incremental harmonic balance method and the harmonic balance-Newton Raphson method. *Journal of Applied Mechanics*, *53*(2), 455-457.

Ferri, A. A., & Dowell, E. H. (1988). Frequency domain solutions to multi-degree-of-freedom, dry friction damped systems. *Journal of Sound and Vibration*, *124*(2), 207-224.

Fey, R. H. B, Van Campen, D. H., & De Kraker, A. (1996). Long term structural dynamics of mechanical systems with local nonlinearities. *Journal of Vibration and Acoustics*, *118*, 147-153.

Fey, R. H. B. (1992). Steady-state behaviour of reduced dynamic systems with local nonlinearities. *Technische Universiteit Eindhoven*.

Gondhalekar, A. C., Petrov, E. P., & Imregun, M. (2009). Parameters identification for nonlinear dynamic systems via genetic algorithm optimization. *Journal of Computational and Nonlinear Dynamics*, *4*(4), 041002.

Hot, A. (2012). *Validation expérimentale de structures localement non-linéaires dans un contexte spatial* (Doctoral dissertation, Besançon).

Hu, X., Prabhu, S., Atamturktur, S., & Cogan, S. (2017). Mechanistically-informed damage detection using dynamic measurements: Extended constitutive relation error. *Mechanical Systems and Signal Processing*, *85*, 312-328.

Huang, S., Petrov, E. P., & Ewins, D. J. (2006). Comprehensive analysis of periodic regimes of forced vibration for structures with nonlinear snap-through springs. *Applied Mechanics and Materials*, *5*(6) 3-13.

Isasa, I., Hot, A., Cogan, S., & Sadoulet-Reboul, E. (2011). Model updating of locally non-linear systems based on multi-harmonic extended constitutive relation error. *Mechanical Systems and Signal Processing*, *25*(7), 2413-2425.

Jaishi, B., & Ren, W. X. (2007). Finite element model updating based on eigenvalue and strain energy residuals using multiobjective optimisation technique. *Mechanical Systems and Signal Processing*, *21*(5), 2295-2317.

Kerschen, G., Golinval, J. C., Vakakis, A. F., & Bergman, L. A. (2005). The method of proper orthogonal decomposition for dynamical characterization and order reduction of mechanical systems: an overview. *Nonlinear Dynamics*, *41*(1-3), 147-169.

Kerschen, G., Lenaerts, V., & Golinval, J. C. (2003). Identification of a continuous structure with a geometrical non-linearity. Part I: Conditioned reverse path method. *Journal of Sound and Vibration*, *262*(4), 889-906.

Kerschen, G., Worden, K., Vakakis, A. F., & Golinval, J. C. (2006). Past, present and future of nonlinear system identification in structural dynamics. *Mechanical Systems and Signal Processing*, *20*(3), 505-592.

Kerschen, G., Peeters, M., Golinval, J. C., & Vakakis, A. F. (2009). Nonlinear normal modes, Part I: A useful framework for the structural dynamicist. *Mechanical Systems and Signal Processing*, *23*(1), 170-194.

Kim, G. H., & Park, Y. S. (2004). An improved updating parameter selection method and finite element model update using multiobjective optimisation technique. *Mechanical Systems and Signal Processing*, *18*(1), 59-78.

Kurt, M., Eriten, M., McFarland, D. M., Bergman, L. A., & Vakakis, A. F. (2015). Methodology for model updating of mechanical components with local nonlinearities. *Journal of Sound and Vibration*, *357*, 331-348.

Larsson, A., & Abrahamsson, T. (1999). A comparison of finite element model error localization methods. In *IMAC XVII-17th International Modal Analysis Conference-Modal Analysis: Reducing the Time to Market*, 929-935.

Lenaerts, V., Kerschen, G., & Golinval, J. C. (2001). Proper orthogonal decomposition for model updating of non-linear mechanical systems. *Mechanical Systems and Signal Processing*, *15*(1), 31-43.

Leung, A. Y. T., & Fung, T. C. (1989). Phase increment analysis of damped Duffing oscillators. *International Journal for Numerical Methods in Engineering*, *28*(1), 193-209.

Llau, A., Jason, L., Dufour, F., & Baroth, J. (2015). Adaptive zooming method for the analysis of large structures with localized nonlinearities. *Finite Elements in Analysis and Design*, *106*, 73-84.

Masri, S. F., & Caughey, T. (1979). A nonparametric identification technique for nonlinear dynamic problems. *Journal of Applied Mechanics*, *46*(2), 433-447.

Meyer, S., & Link, M. (2003). Modelling and updating of local non-linearities using frequency response residuals. *Mechanical Systems and Signal Processing*, *17*(1), 219-226.

Moaveni, B., & Asgarieh, E. (2012). Deterministic-stochastic subspace identification method for identification of nonlinear structures as time-varying linear systems. *Mechanical Systems and Signal Processing*, *31*, 40-55.

Nelson, H. D., & Nataraj, C. (1989). Periodic solutions in rotor dynamic systems with nonlinear supports: a general approach. *Journal of Vibration, Acoustics, Stress and Reliability in Design*, *111*, 187-193.

Niwa, A., & Clough, R. W. (1982). Non-linear seismic response of arch dams. *Earthquake Engineering & Structural Dynamics*, *10*(2), 267-281.

Nocedal, J., & Wright, S. (2006). *Numerical optimization*. Springer Science & Business Media.

Qu, Z. Q. (2002). Model reduction for dynamical systems with local nonlinearities. *AIAA Journal*, *40*(2), 327-333.

Ren, Y., Lim, T. M., & Lim, M. K. (1998). Identification of properties of nonlinear joints using dynamic test data. *Transactions-ASME, Journal of Vibration and Acoustics*, *120*, 324-330.

Schultze, J. F., Hemez, F. M., Doebling, S. W., & Sohn, H. (2001). Application of non-linear system model updating using feature extraction and parameter effects analysis. *Shock and Vibration*, *8*(6), 325-337.

Shi, G., & Atluri, S. N. (1992). Nonlinear dynamic response of frame-type structures with hysteretic damping at the joints. *AIAA Journal*, *30*(1), 234-240.

Garrison, S., Atamturktur, S., Lebensohn, R., & Kaschner, G. (2016). Experiment-based validation and uncertainty quantification of coupled multi-scale plasticity models. *Multidiscipline Modeling in Materials and Structures*, *12*(1), 151-176.

Stoker, J. J. (1950). *Nonlinear vibrations in mechanical and electrical systems*. New York: Interscience Publishers.

Tamura, H., Tsuda, Y., & Sueoka, A. (1981). Higher approximation of steady oscillations in nonlinear systems with single degree of freedom: Suggested multi-harmonic balance method. *Bulletin of JSME, 24*(195), 1616-1625.

Thouverez, F. (2003). Presentation of the ECL benchmark. *Mechanical Systems and Signal Processing*, *17*(1), 195-202.

Tondl, A. (1974). Notes on the solution of forced oscillations of a third-order non-linear system. *Journal of Sound and Vibration, 37*(2), 273-279.

Vakakis, A. F. (1997). Non-linear normal modes (NNMs) and their applications in vibration theory: an overview. *Mechanical Systems and Signal Processing*, *11*(1), 3-22.

Van Buren, K. & Atamturktur, S. (2012). A Comparative Study: Predictive Modeling of Wind Turbine Blades. *Journal of Wind Engineering*, 36(3), 235- 250.

Wojtkiewicz, S. F., & Johnson, E. A. (2011). Efficient uncertainty quantification of dynamical systems with local nonlinearities and uncertainties. *Probabilistic Engineering Mechanics*, *26*(4), 561-569.

Worden, K. (2003). Cost action F3 on structural dynamics: benchmarks for working group 2—structural health monitoring. *Mechanical systems and signal processing*, *17*(1), 73-75.

Worden, K., & Tomlinson, G. R. (2000). *Nonlinearity in structural dynamics: detection, identification and modelling*. CRC Press.

Yu, E., Taciroglu, E., & Wallace, J. W. (2007). Parameter identification of framed structures using an improved finite element model-updating method—Part I: formulation and verification. *Earthquake Engineering & Structural Dynamics*, *36*(5), 619-639.

CHAPTER FIVE

CONCLUSION

5.1 Major Contributions

Based on a combination of the Extended Constitutive Relation Error (ECRE), a method developed for error localization in finite element models, and experimental modal testing, this dissertation has focused on developing a novel damage detection method for damage identification, localization, quantification and model calibration. The studies proposed in this dissertation can significantly improve damage detection methods that are based on model calibration techniques. Different than the traditional black-box model calibration that merely relies on the outputs of numerical models, the proposed ECRE-based damage detection methods belong to the white-box approaches that integrate the knowledge regarding the underlying mechanistic behavior of the structural system. The major contributions achieved in this dissertation are summarized as following:

Chapter 2 proposes a novel a two-step ECRE-based damage detection approach through integrating the mechanistic concept of ECRE into the model-based damage detection process by explicitly considering the underlying dynamic behavior of linear elastodynamic systems. I demonstrated and verified its feasibility in identifying the presence, location and relative severity of damage on a scaled, two-story steel frame for damage scenarios of varying type and severity.

Traditional model-based damage detection relies on a well-calibrated numerical model. The proposed approach, however, calculates the constitutive error in a numerical model of the undamaged system and employs these residual errors to account for the model's imperfection and, finally, calculates a damage indicator using a numerical model of undamaged system and the experimental data of the damaged system. This results in significant reduction in computational costs that arise during calibration of the reference numerical model. Moreover, the ECRE-based damage detection method can identify the damage location—unlike many model calibration-based approaches which require an additional step after damage is detected. Additionally, given the availability of enough measurement points with low enough experimental uncertainty, the proposed method can determine the relative severity of the damage based on a proportional relationship between the damage indicator values and the severity of the damage.

Chapter 3 extends the two-step, ECRE-based damage detection method by simultaneously considering the effect of stiffness and mass variation in the calculation of residual energy. There are two specific reasons for the additional consideration of mass change: (1) the damage results in a variation in the mass in addition to the stiffness reduction; (2) the numerical model has an imperfect representation of the mass distribution. The accuracy and efficiency of the approach is demonstrated using the experimental measurements from the same steel frame with damage scenarios of varying type and

severity. Compared to the original ECRE-based damage detection approach, a noticeable improvement is achieved in the damage detection accuracy, with a higher damage indicator and less false negatives.

The modified ECRE-based damage detection approach has all the above-mentioned advantages as the original two-step, ECRE-based damage detection method in Chapter 2. Additionally, the proposed modified ECRE approach accounts for the mass-related residual energy in the constitutive relation error, allowing for the calculation of a more reliable damage indicator. Consequently, the modified ECRE-based damage detection approach achieves more effective and robust performance in localizing the damage when mass modeling error or mass-related damage is presented.

Chapter 4 presents an iterative model calibration approach for dynamical systems with spatially localized nonlinear components. The approach implements the ECRE-based model calibration method using the multi-harmonic balance (MHB) method, and is conceived to separate the errors in the representation of the predominantly linear and nonlinear components through a two-step process. The first step is based on the low magnitude excitation test, which ensures the dynamic response of the system remains predominately linear and the location of model error associated with the linear component can be separately identified through the utilization of ECRE-MHB method. In the second step, a higher magnitude excitation is applied to ensure the nonlinear dynamic response.

The measurements from both low and high magnitude excitation tests are used to calibrate the parameters associated with linear components and those associated with the nonlinear components without making any assumptions regarding linear model accuracy.

The proposed method has been demonstrated on an academic example using synthetic measurements. The Iterative Integrated MHB-ECRE calibration approach has shown superiority to the conventional MHB-ECRE method, while providing more reliable calibration of the nonlinear component parameter with less dependency on *a priori* knowledge of the accuracy of the associated linear system. An iterative calibration process is also developed for solving the optimization problem so that the model parameters can be calibrated with less computational cost and more accurate results compared to a discretized approach. Moreover, the influence of measurement noise, applied force location, a reduced set of measurements, and error location on the proposed method has been investigated. These studies show that the method is quite robust against introduced measurement noise, especially in the calibration of the linear component parameter to the true value.

5.2 Limitations and recommendations for future research

This dissertation has been focused on identification and quantification techniques for damage detection, and closely related model calibration topics. However, I have not assumed that structural health monitoring problems can be fully solved using the

techniques developed in this dissertation. The limitations and future work for this dissertation are summarized as following:

ECRE-based damage detection scheme

Although the two-step ECRE-based damage detection method is promising, it is also strongly dependent on the number and distribution of sensors, as well as the level of experimental uncertainty. Thus, sensor placement strategy should be carefully developed for the success of the damage detection approach. Future applications of ECRE-based damage detection method are also suggested to utilize full-field surface vibration measurement techniques, such as instance laser Doppler vibrometers or high-frequency cameras, to provide the needed quality and quantity of experimental measurements.

The proposed approach considers the change of stiffness and mass in the identification of damage. Since significant changes may occur in damping due to structural system damage, damping has the potential to be incorporated into the proposed damage detection methodology.

Model calibration approach using integrated MHB-ECRE algorithm

Based on the proposed integrated MHB-ECRE model calibration approach, a reliable locally nonlinear model can be obtained. However, the verification of the proposed approach is only conducted using the synthetic measurements from numerical model. Therefore, a practical application is needed based on experimental measurements.

A well-calibrated, locally nonlinear model has a potential to be used for damage prognosis that can estimate structural system's remaining useful life. Future research for integrated MHB-ECRE model calibration method may focus on developing a decision-making tool for maintenance and service requests. While ECRE-based model calibration method has been applied for damage detection as described in Chapter 3 and Chapter 4, this nonlinear model calibration strategy can also be extended to identify the damage in a nonlinear structural system. However, the difficulty of this implementation is that three sources may lead to nonlinear dynamical behavior in the nonlinear system: 1) potential structural damage in linear component; 2) potential structural damage in nonlinear component; 3) undamaged nonlinear component. Thus, if the undamaged system is nonlinear, the healthy nonlinear dynamical behaviors must be distinguished from nonlinear behaviors due to damage. This complication must be investigated further in future research of damage detection for locally nonlinear systems.